Feasibility Study of III-Nitride-Based Transistors Grown by Ammonia-Based Metal-Organic Molecular Beam Epitaxy

A Dissertation
Presented to
The Academic Faculty

By

Daniel D. Billingsley

In partial fulfillment
Of the requirements for the Degree
Doctor of Philosophy in Electrical Engineering

Georgia Institute of Technology

August 2010

Feasibility Study of III-Nitride-Based Transistors Grown by Ammonia-Based Metal-Organic Molecular Beam Epitaxy

Dr. W. Alan Doolittle
School of Electrical and Computer Engineering
Georgia Institute of Technology

Dr. A. Bruno Frazier
School of Electrical and Computer Engineering
Georgia Institute of Technology

Dr. Oliver Brand
School of Electrical and Computer Engineering
Georgia Institute of Technology

Dr. John Papapolymerou
School of Electrical and Computer Engineering
Georgia Institute of Technology

Dr. W. Brent Carter
School of Materials Science and Engineering
Georgia Institute of Technology

Date Approved: June 4, 2010

To Amanda, for her patience
To my parents, for their guidance
To my siblings, for their inspiration
I love you all

ACKNOWLEDGEMENTS

I would like to thank foremost my family for their continual, unconditional support. My parents, Art and Kathy Billingsley, have been the most important figures in my life and have supported my every life decision. My siblings, Sarah, Emily and Bradly, have been both my best friends and my biggest supporters. My fiancée, Amanda Hoffpauir, has endured the goods and bads associated with graduate school and has provided unwavering support in our journey together. Without my family, I am unsure if I would have succeeded in my graduate studies.

My advisor, Dr. William Alan Doolittle, has provided the guidance necessary to reach my personal goals, and the patience to continually aid in my research. He has been not only a mentor in my research, but also a mentor in my life. Additionally, the members of Dr. Doolittle's research group, who I consider not only colleagues but friends include Walter Henderson, Dr. Elaissa Trybus, Dr. Shawn Burnham, Dr. David Pritchett, Dr. Kyoung-Keun Lee, Dr. Alex Carver, Dr. Gon Namkoong, Michael Moseley, William Laws Calley, Jonathon Lowder and Jordan Greenlee.

I would like to thank my thesis research committee; Dr. Bruno Frazier, Dr. Oliver Brand, Dr. John Papapolymerou, and Dr. Brent Carter, for their support and guidance throughout my thesis defense. Additionally, the staff of the MiRC has been extremely helpful and accommodating throughout my research, specifically Charlie Suh, Ben Hollerbach, Dean Sutter, Jason Herrington, and Gary Spinner.

Finally, I would like to thank the Air Force Office of Scientific Research, specifically Drs. Donald Silversmith, Gerald Witt and Todd Steiner for their financial contributions that has made this research possible under the “Non-Equilibrium, Wide-Application Epitaxial Patterning by Intelligent Control” multidisciplinary university research initiative.

TABLE OF CONTENTS

LIST OF TABLES

LIST OF FIGURES

LIST OF NOMECLATURE

λ	wavelength
κ	thermal conductivity
ε	dielectric constant, emissivity
ε_o	electric permittivity of free space
Å	angstrom (10^{-10} meter)
$\Delta\omega$	spacing in omega position between fringes
Φ	angle difference between beam and surface
φ	work function
η_{ext}	external quantum efficiency
μ_{2DEG}	2DEG mobility
μ_n	electron mobility
μ_p	hole mobility
μm	micron / micrometer

2DEG	2-dimensional electron gas
[C]	carbon concentration
a^0_{GaN}	theoretical a-axis lattice spacing for GaN
a^0_{AlN}	theoretical a-axis lattice spacing for AlN
(ads)	adsorption site
A	area
AFM	atomic force microscopy
AlGaN	aluminum gallium nitride
Al_2O_3	sapphire, aluminum oxide
AsH_3	arsine
Al	aluminum
AlN	aluminum nitride
Be	beryllium
C	conductance, capacitance
C-V	capacitance-voltage
C_{gs}	gate-source capacitance
C_I	carbon substitution at interstitial position
C_{Ga}	carbon substitution at gallium site
C_N	carbon substitution at nitrogen site
C_o	capacitance with no deep-level impurities
c_{xy}	elastic constant
C_2H_5	ethane
C_2H_4	ethylene
CBE	chemical beam epitaxy
CB	conduction band
CBr_4	carbon tetrabromide

Cs+	positive cesium ion
D	orifice diameter
DEGa	diethylgallium
DI	de-ionized
e_{xy}	piezoelectric constant
E_c	electric breakdown field
E_g	bandgap energy
eV	electron volt
f_T	unity gain frequency
f_{max}	maximum oscillation frequency
FWHM	full-width at half-maximum
ΔG	Gibbs free energy
g_m	transconductance
Ga	gallium
Ga(ads)	adsorbed gallium
GaAs	gallium arsenide
GaN	gallium nitride
GHz	gigahertz
GSMBE	gas-source molecular beam epitaxy
H_2SO_4	sulfuric acid
H_2O_2	hydrogen peroxide
HEMT	high electron mobility transistor
HF	hydrofluoric acid
HR	high-resistivity
$I_{3.4eV}$	PL transition intensity at 3.4 eV
$I_{3.0eV}$	PL transition intensity at 3.0 eV
$I_{2.85eV}$	PL transition intensity at 2.85 eV
I_d	drain current
InGaN	indium gallium nitride
InN	indium nitride
K_S	relative permittivity
kJ	kiloJoules
LED	light-emitting diode
LD	laser diode
L_G	gate length
MBE	molecular beam epitaxy
MEGa	monoethylgallium
MESFET	metal-semiconductor field effect transistor
Mg	magnesium
MOMBE	metal-organic molecular beam epitaxy
MOCVD	metal-organic chemical vapor deposition
MOVPE	metal-organic vapor phase epitaxy
mTorr	milliTorr
n	electron concentration
$n_T(t)$	deep level impurity density
N	nitrogen

N_D	charge density
Nb	niobium
N_S	sheet charge density
NH_x	ammonia radical
NH_3	ammonia
nm	nanometer
OI	optical interferometry
P	power
P_{down}	downstream pressure
P_{pz}	piezoelectric polarization
P_{sp}	spontaneous polarization
P_{up}	upstream pressure
PL	photoluminescence
PMT	photomultiplier tube
q	electronic charge
Q	throughput
Q_g	charge per unit width under gate
$Q_{x,y}$	X-ray scattering vectors
RF	radio frequency
RHEED	reflective high-energy electron diffraction
RGA	residual gas analysis
rms	root-mean-square
rpm	revolutions per minute
RSM	reciprocal space map
sccm	standard cubic centimeters per minute
SEM	scanning electron microscopy
SI	semi-insulating
SiC	silicon carbide
SIMS	secondary ion mass spectroscopy
t	film thickness
T	temperature
T_{growth}	growth temperature
TEAl	triethylaluminum
TEGa	triethylgallium
TIPG	tri-isopropyl gallium
TIBG	tri-isobutyl gallium
TMGa	trimethylgallium
UHV	ultra-high vacuum
UV	ultra-violet
$v(x)$	electron velocity
v_{eff}	effective electron velocity
v_{sat}	saturated electron velocity
V_{bi}	built-in voltage
V_{DS}	drain-source voltage
V_{GS}	gate-source voltage
V/III ratio	ratio of group V to group III elements

VB	valence band
W	tungsten, watts
W/mm	Watts/millimeter
$W_D(x)$	depletion region thickness
X^S_{Al}	aluminum solid phase composition
X^G_{Al}	aluminum gas phase composition
XRD	X-ray diffraction

SUMMARY

Although commercially available high-electron mobility transistors (HEMTs) based on the III-Nitride material system are available, there still remains areas for further optimization. These transistor devices are currently limited because of current leakage when the devices are operated at increased operating voltages. To reach the full potential of these devices, these leakage mechanisms need to be addressed. The objective of this work is to utilize the highly resistive properties of carbon-doped gallium nitride (GaN) as a low-leakage buffer layer for HEMTs. By increasing the resistivity of the underlying GaN layer, the source-drain current flow will be limited to electrons in the two-dimensional electron gas (2DEG) confined to the interface, reducing leakage paths through the GaN buffer layer, ultimately increasing the power density of the device.

These films are deposited via a novel ammonia-based metal-organic molecular beam epitaxy (NH_3-MOMBE) system capable of producing unintentionally carbon-doped GaN films with carbon concentrations ([C]) in excess of 10^{21} atoms/cm^3. These high levels of carbon incorporation lead to highly-resistive GaN buffer layers with a resistivity estimated at $\sim 10^{12}$ Ω-cm. In addition, the deposition of aluminum gallium nitride (AlGaN) has been accomplished for the first time in an NH_3-MOMBE environment. The AlGaN alloy is necessary for the production of a 2DEG, which is the source of electrons for the operation of the transistor. While providing the ability to produce highly-resistive buffer layers, the carbon which is unintentionally incorporated during the deposition of

the films may also become a source of channel depletion if the incorporation levels cannot be controlled. The results of this work demonstrate that carbon-doped NH_3-MOMBE thin films are extremely resistive, yet further optimization is necessary for the realization of transistor devices because of the trap states that are produced from the excessive carbon incorporation levels.

CHAPTER 1: INTRODUCTION

III-nitrides are a promising material system with unique material properties, which allows them to be utilized in a variety of semiconductor devices. III-nitrides grown by NH_3-MOMBE are typically grown with high carbon levels ($> 10^{21}$ cm^{-3}) as a result of the incomplete surface pyrolysis of the metal-organic sources. Recent research has involved the compensating nature of carbon in III-nitrides to produce semi-insulating films, which can provide low-leakage buffer layers in transistor devices. The aim of this work is to investigate the possibility of forming a 2DEG, which utilizes the highly carbon-doped GaN layers grown by NH_3-MOMBE to produce low-leakage buffer layers in the fabrication of HEMTs. These low leakage GaN buffers would provide increased HEMT performance, with better pinch-off, higher breakdown voltages and increased power densities. Additionally, methods of controlling and/or reducing the incorporation of carbon will be undertaken in an attempt to broaden the range of possible device applications for NH_3-MOMBE. To realize these transistor devices, optimization and improved understanding of the growth conditions for both GaN and AlGaN will be explored with the ultimate goal of determining the feasibility of III-nitride transistors grown by NH_3-MOMBE.

1.1 MOMBE

Metal-organic molecular beam epitaxy (MOMBE), also known as chemical beam epitaxy (CBE) or gas-source molecular beam epitaxy (GSMBE), is a hybrid growth technique that combines the benefits of metal-organic chemical vapor deposition (MOCVD) and solid-source molecular beam epitaxy (MBE). MOCVD, which is also known as metal-organic vapor phase epitaxy (MOVPE), was founded in the late 1960s by Manasevit *et al.* [1]. MOCVD (Fig 1.1) is a chemical vapor deposition technique that utilizes gaseous sources as the precursors with growth pressures typically operated above 1 millitorr (mTorr). For the supply of nitrogen (N), the most common source is ammonia (NH_3), although alternatives such as phenyl hydrazine [2], dimethylhydrazine [3], and N_2 plasmas [4] have been attempted. Typically, low vapor pressure metal-organic sources are employed as the group III species. To obtain the high group III fluxes necessary, carrier gases such as H_2 or N_2 are used to transport the metal species. For MOCVD, pyrolysis of the gaseous reactants occurs as they pass over a heated substrate, where they react chemically to form the epitaxial film (Figure 1.1). To facilitate this pyrolysis, growth temperatures are typically much hotter than MBE (~1,100 °C, as compared to ~700 °C). This combined gas phase and surface pyrolysis and subsequent film formation is a more complicated growth process than its MBE counterpart, yet it benefits from higher growth rates, generally higher throughput, and extremely high quality films. These benefits have lead MOCVD to become the most common commercial compound semiconductor epitaxy technique for light emitting diodes and laser diodes yet at present,

MOCVD has little market in electronic devices due to the non-uniform deposition and limited interface abruptness needed for transistor structures.

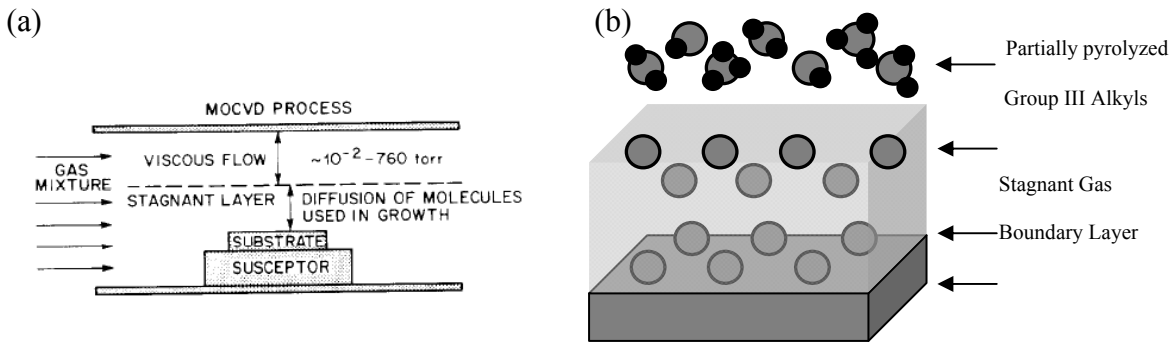

Figure 1.1: Schematic of typical MOCVD (a) growth reactor and corresponding (b) growth kinetics [5, 6].

Alternatively, MBE (Figure 1.2) is an epitaxial technique that occurs via reactions between atomic or molecular beams on a heated substrate in an ultra-high vacuum (UHV) environment. MBE was first performed in 1970 by Cho *et al.* [7] for the deposition of gallium arsenide (GaAs). The molecular beam of group III sources is provided through thermal evaporation of elemental sources in effusion cells. N radicals are typically generated either through dissociation by a RF-plasma source [8, 9] or by surface pyrolysis of an ammonia source [10, 11]. The UHV environment ($< 10^{-10}$ Torr) increases the mean-free path of the reactants, reducing collisions and providing a molecular beam flow regime. Although this decreased growth pressure results in a reduction in the growth rate, precise layer control and abrupt interfaces can be achieved, which is ideal for the deposition of device heterostructures. Another benefit of the UHV environment is the

ability to monitor the growth process *in situ* through characterization techniques such as reflection high-energy electron diffraction (RHEED) and residual gas analyzers (RGA). The precise control and *in situ* characterization of the growing surface has lead MBE to become the dominant technique for the research of electronic device structures. However, drawbacks such as maintenance requirements of the UHV components and solid sources, as well as high initial cost and limited throughput of the system, have prevented MBE growth from receiving increased commercial attention.

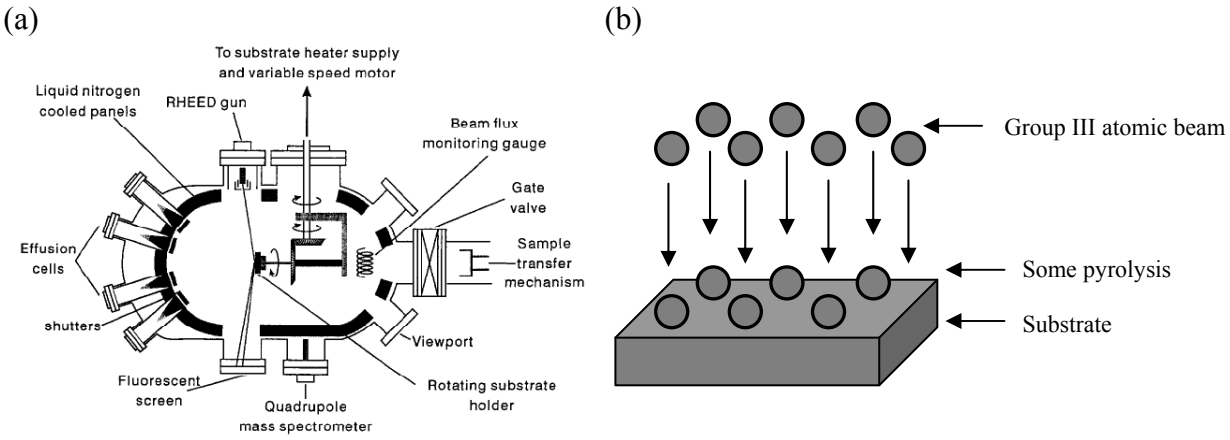

Figure 1.2: Schematic of traditional MBE (a) growth system and corresponding (b) growth kinetics [5, 12].

MOMBE (Figure 1.3) is a hybrid growth technique that exploits the benefits of both traditional solid-source MBE and MOCVD. Vodjdani *et al.* [13], who are commonly credited with the invention of MOMBE, first deposited GaAs in 1982 through the decomposition of arsine (AsH_3) and trimethylgallium (TMGa). The low growth pressure typically associated with MBE allows for *in-situ* growth monitoring equipment,

such as RHEED and RGA, which cannot be utilized in MOCVD because of the higher growth pressures. MOMBE also utilizes externally-plumbed gaseous precursors, which are common in MOCVD, which increases the throughput of the system by eliminating the need to replace solid sources, which requires extensive downtime and system baking. To effectively utilize the benefits of MOMBE, the temperature dependent surface reactions between NH_3 and the metal-organic precursors must be properly understood.

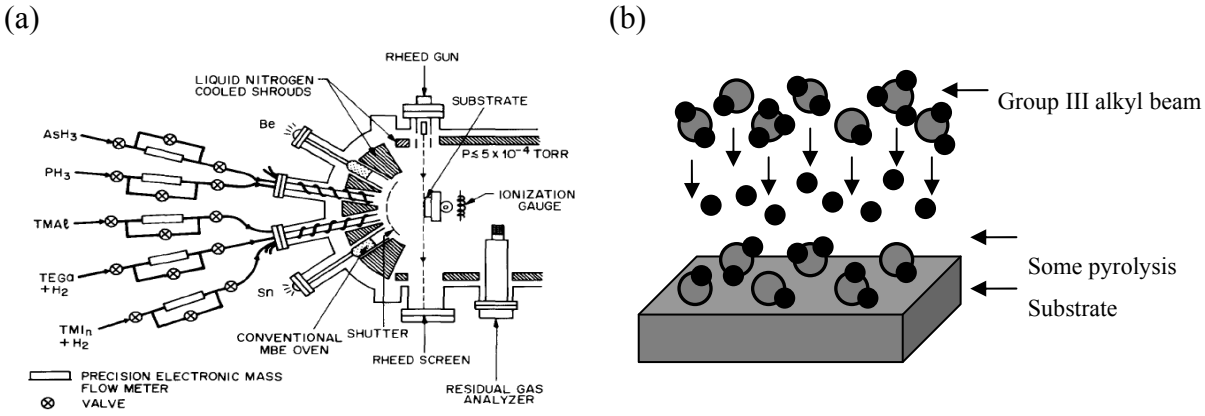

Figure 1.3: Schematic of traditional MOMBE (a) growth system and corresponding (b) growth kinetics [5, 6].

1.2 III-Nitride Material System

GaN and its alloys have attracted enormous attention because of their utility in a wide range of applications, including photonic [14], photovoltaic [15], and transistor devices [16]. In 1923 Johnson *et al.* [17] discovered GaN through the conversion of metallic Ga in an NH_3 gas stream. Aluminum nitride (AlN) and indium nitride (InN)

were discovered in 1924 [18] and 1938 [19], respectively. III-nitrides have received increased attention as a result of their improved material properties compared to competing material systems, such as arsenide and silicon semiconductors. Some of the most notable properties of the III-nitride material system are listed in Table 1.1.

Table 1.1: Properties of III-nitride binaries and selected competing semiconductors [20-24].

Property	**Si**	**GaAs**	**GaN**	**AlN**	**InN**
Bandgap energy, E_g (eV)	1.12	1.43	3.39	6.2	0.7
Lattice constants, a/c (Å)	5.431	5.654	3.189 5.185	3.112 4.982	3.537 5.704
Dielectric constant, ε	11.9	12.5	9.5	8.5	15.3
Electric breakdown field, E_c (MV/cm)	0.3	0.4	3.3	8.4	1.2
Electron mobility, μ_n (cm^2/V s)	1500	8500	990	1100	3000
Hole mobility, μ_p (cm^2/V s)	500	400	10	14	39
Thermal conductivity, λ (W/cm K)	1.5	0.54	1.3	2.85	0.45
Saturated electron drift velocity, v_{sat} (x10^7 cm/s)	1	1	2.5	1.7	2.5

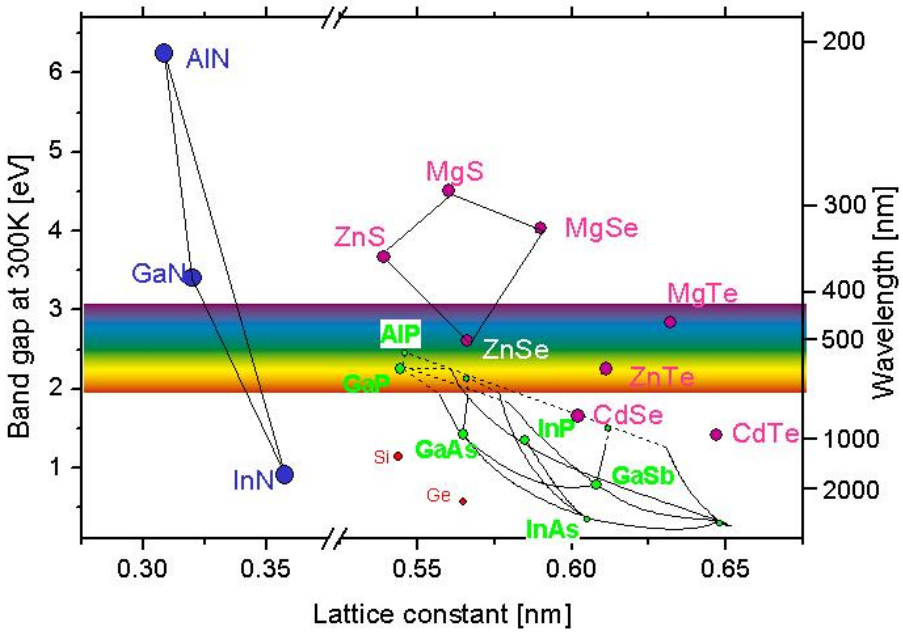

Figure 1.4: Room temperature energy bandgap and corresponding wavelength versus the lattice constant of common semiconductor material systems [25].

III-nitrides are direct bandgap semiconductors with bandgap energies ranging from 0.7 eV for pure InN to 6.2 eV for pure AlN. This large range of bandgap energies corresponds to a wavelength spectrum that spans from near-infrared to ultraviolet, as shown in Figure 1.4. The bandgap energy (E_g) for any of the III-nitride alloys can be calculated through the quadratic equation

$$E_g(A_{1-x}B_x) = (1-x)E_g(A) + xE_g(B) - x(1-x)C \tag{1.1}$$

where $E_g(A)$ and $E_g(B)$ are the bandgaps of binaries *A* and *B*, *C* is a nonzero bowing parameter, and *x* is the composition of the alloy [26]. The bowing parameter, C, is dependent on the alloy and has been measured as 1.38 for AlGaN [27] and 1.4 for InGaN

[28]. This large bandgap range, combined with their direct transition, makes this material system ideal for optical devices.

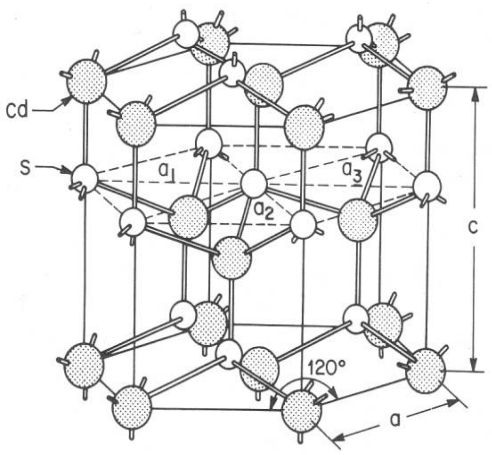

Figure 1.5: Illustration of the wurtzite crystal structure with base length, a, and height, c [29].

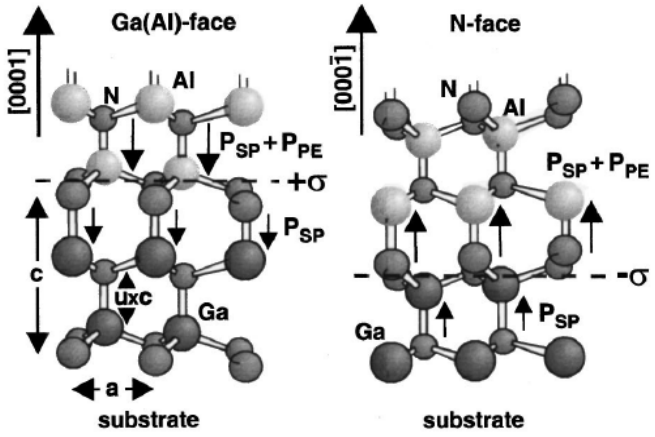

Figure 1.6: Schematic of the polar nature of III-nitrides, showing both N-face and Ga(Al)-face orientations [30].

III-nitrides exhibit a variety of crystal structures, including zincblende, wurtzite and rock salt structures [31, 32], yet the wurtzite crystal structure is the thermodynamically stable state [33]. The wurtzite structure shown in Figure 1.5 is a member of the hexagonal crystal system with lattice constants, a and c. Table 1.1 lists the lattice constants for the III-nitride binaries: GaN, AlN, and InN. These crystal structures lack inversion symmetry, which leads to a strong ionicity and a residual electrical polarity of the semiconductor. In these materials, a pyroelectric axis is parallel to the [0001] direction and the polarity of the crystal is determined by the bond direction. Ga-polar materials have a (0001) crystal face that is entirely Ga atoms with bonds from Ga to N along the [0001] direction. Alternatively, N-polar materials consist of a completely N covered $(000\bar{1})$ face with N to Ga bonds along the [0001] direction, as seen in Figure 1.6. The polarity of the material plays an important role in the bulk properties of the film [34, 35].

Table 1.2: Spontaneous polarization parameters of III-nitride semiconductors [31].

	GaN	**AlN**	**InN**
Spontaneous polarization, P_{SP} ($C\ m^{-2}$)	- 0.034	- 0.090	- 0.042

As mentioned previously, the polar nature of wurtzite materials results in a residual electrical polarity, which is known as spontaneous polarization. The magnitude of the spontaneous polarization is dependent on the crystalline symmetry and the value for each binary is listed in Table 1.2. This polarization leads to the formation of a built-in electric polarization oriented along the [0001] direction. In addition to spontaneous polarization, a piezoelectric polarization can arise in III-nitride crystals because of the strain in the film and can be solved through equation 1.2 [30].

$$P_{PZ} = 2 \cdot \left(\frac{a - a_o}{a_o}\right)\left(e_{31} - e_{33} \cdot \frac{C_{13}}{C_{33}}\right) \tag{1.2}$$

In (1.2) a and a_o are lattice constants, C_{xy} denotes elastic constants, and e_{xy} denotes piezoelectric constants. Therefore, the total polarization in the crystal is a summation of both spontaneous and piezoelectric components, which can result in the formation of very high electric fields of ~2 MV/cm [36].

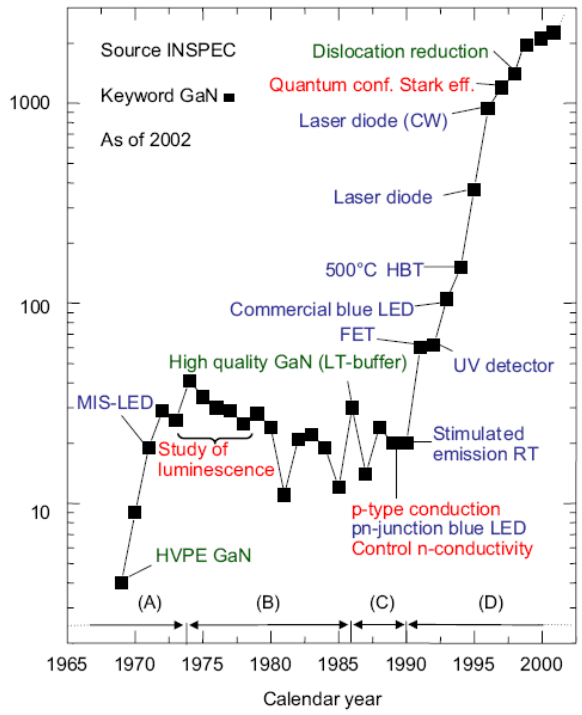

Figure 1.7: Number of publications relating to nitride research per year, as calculated by INSPEC [37].

The aforementioned characteristics of the III-nitride materials have lead to their utilization in a variety of devices. The first major breakthrough for nitride devices came in 1989 with the fabrication of GaN-based blue light emitting diodes (LEDs) via a p-n junction [38]. This p-n junction became possible because of an improvement in GaN crystalline quality, through the use of a low-temperature buffer layer introduced by Amano *et al.* [39]. This buffer allowed p-type conductivity and improved n-type doping, which was necessary for the realization of these devices. At the time, typical LEDs exhibited external quantum efficiencies (η_{ext}) of ~0.1 %. Since the aforementioned improvement in III-nitride crystal quality in 1989, the interest in nitrides has increased dramatically, as seen in Fig 1.7. Today, blue LEDs have achieved η_{ext} over 35 % and

nitride-based optical device research has spread to other areas, including laser diodes (LDs), ultra-violet (UV) detectors, and photovoltaics [14, 15, 32].

The spontaneous and piezoelectric polarization effects combined with the high electron drift velocities of III-nitrides have resulted in the utilization of the nitride materials in the fabrication of high-power transistors based on the GaN/AlGaN heterostructure. The abrupt polarization change at the GaN/AlGaN interface leads to the formation of a high density electron sheet, known as a 2DEG [30], which results in electron mobilities exceeding 2,100 cm^2/Vs at low electron carrier densities [40]. In 1994, this 2DEG was utilized for the development of a high-speed transistor device known as a HEMT [41]. Since then, HEMTs have become highly researched nitride devices because of their lack of doping requirements as well as a relatively simple device structure. Current HEMTs have achieved continuous wave current densities of 41.4 Watts/millimeter (W/mm) at 4 gigahertz (GHz) [42] with maximum oscillation frequencies (f_{max}) of 300 GHz [43].

1.3 Role of Carbon in III-Nitrides Grown by MOMBE

The utilization of metal-organic sources for the growth of III-nitrides leads to the unintentional incorporation of carbon (C) into the epitaxial films. The thermal decomposition of triethylgallium (TEGa, $Ga(C_2H_5)_3$) has been exhaustively studied on the surface of GaAs [44-47]. This thermal process involves a step-wise decomposition through the loss of an ethyl (C_2H_5) species at each step, as seen in Figure 1.8. If the

molecule is effectively adsorbed and desorption does not occur, the molecule undergoes thermal decomposition into diethylgallium (DEGa, $Ga(C_2H_5)_2$) and eventually monoethylgallium (MEGa, $Ga(C_2H_5)$), as seen in reactions (1.3) and (1.4), respectively.

$$TEGa_{(ads)} \rightarrow DEGa_{(ads)} + C_2H_{5\,(g)} \tag{1.3}$$

$$DEGa_{(ads)} \rightarrow MEGa_{(ads)} + C_2H_{5\,(g)} \tag{1.4}$$

At each decomposition step, further decomposition of an ethyl species can occur through the β-elimination reaction (1.5), resulting in the formation of ethylene (C_2H_4) [44, 47, 48].

$$C_2H_{5\,(ads)} \rightarrow C_2H_{4\,(g)} + H_{(ads)} \tag{1.5}$$

Incomplete pyrolysis of the alkyl species and adsorbed ethyl groups lead to the unintentional incorporation of C into the films [47, 49]. Various metal-organic sources with lower Ga-C bond strengths have been studied in an attempt to reduce the unintentional incorporation of carbon. Sources such as trimethylamine gallane (TMAG) [50], tri-isopropyl gallium (TIPG) [51], and tri-isobutyl gallium (TIBG) [52] have been successful in reducing C incorporation, yet TEGa and trimethylgallium (TMGa) are still the most predominant Ga sources used today, largely due to widespread availability in ultra-high purity form due to the MOCVD market. The unintentional incorporation of C becomes a greater issue when forming ternary alloys, such as AlGaN, since the higher

bond strength of Al-C over Ga-C leads to higher incorporation of C [53]. The use of metal-organic sources in GaAs growth has led to maximum background C concentrations in excess of 10^{20} cm^{-2} [54].

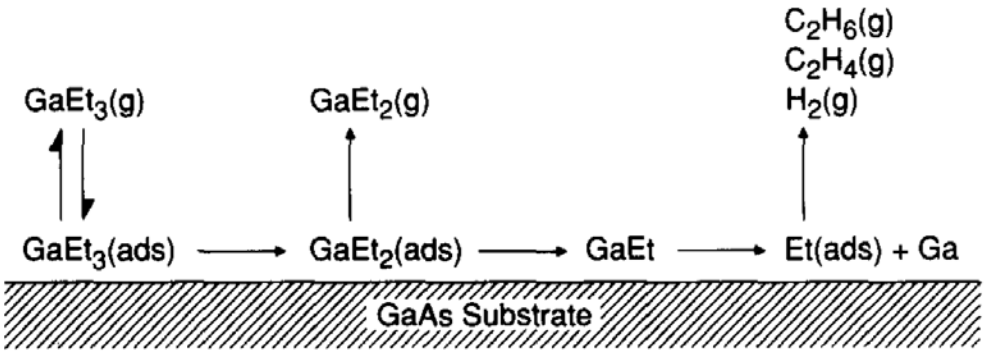

Figure 1.8: Decomposition schematic for the pyrolysis of triethylgallium on the surface of GaAs [45].

Carbon is an amphoteric material in III-nitrides, meaning that it can assume the role of either a donor or an acceptor. This dual-nature, combined with C's incorporation site dependency on growth conditions and Fermi level [55], makes doping with C difficult to consistently reproduce. C can substitute at a variety of lattice sites in GaN, depending on the Fermi level. In GaN, carbon can substitute at either Ga (C_{Ga}) or N (C_N) lattice sites and at various interstitial sites (C_I) [55, 56]. C_N acts as a shallow acceptor with an energy transition ~0.3 eV above the valence band (VB), while C_{Ga} behaves as a shallow donor with an energy transition ~0.2 eV below the conduction band (CB). For C_I, there are two stable configurations: a channel configuration and a split-interstitial configuration, depending on whether the C is at the center of the c-axis or if the C and N

share a lattice space, respectively. Depending on the growth conditions, the preferred C incorporation site is affected as the Fermi level varies, as seen in Figure 1.9. Ga-rich growth conditions lead to preferential incorporation on the N site, while N-rich growth conditions lead to self-compensating effects because carbon will incorporate equally at the Ga and N sites, pinning the Fermi level near midgap.

a) b)

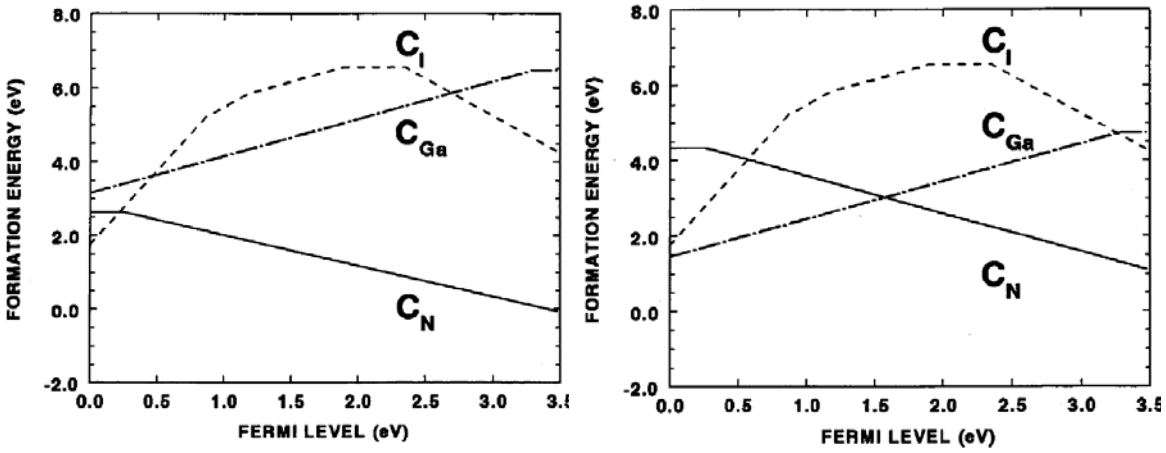

Figure 1.9: Formation energies of C_I, C_{Ga}, and C_N for both (a) Ga-rich growth and (b) N-rich growth as a function of Fermi-level position in the GaN bandgap [55].

Although carbon incorporation has always been a growth concern for MOCVD and MOMBE, recent work in MBE has intentionally doped III-nitride films with carbon [57]. The high thermal ionization energy [58] and tendency to form defect structures [59] that accompanies magnesium (Mg) doping has lead to the study of carbon as an alternative p-type dopant. MBE GaN films utilizing carbon tetrabromide (CBr_4) as the C source have reached [C] > 10^{19} cm^{-3} [57]. Successful C-doping in MBE has been

attributed to the Ga-rich growth conditions commonly used for the growth of GaN in MBE [9], leading to preferential incorporation of carbon on the nitrogen site. C-doping is also being investigated as a method of producing semi-insulating (SI) GaN films through the compensation of shallow donors [60]. These SI films have been utilized in the fabrication of HEMTs and related devices [61, 62] to provide low leakage buffer layers.

Utilizing the compensating property of carbon to produce low leakage buffer layers for AlGaN/GaN HEMTs have led to substantial device improvements. Eliminating conduction in the GaN buffer eliminates parasitic capacitances which lower power gains of the device at higher frequencies [63]. Carbon in the GaN buffer has been introduced unintentionally through adsorbed ethyls, as described earlier, and also through intentional doping using either methane [60, 64, 65] or CBr_4 [57] as the carbon sources. The high [C] obtained through intentional carbon doping have resulted in a GaN buffer resistivity increase from 500 Ω-cm in un-doped GaN to ~10^6 Ω-cm for C-doped GaN [66]. These GaN resistivities result in reduced leakage currents as low as 0.1 pA, up to 10 V, in HEMT devices [65]. These leakage currents for C-doped GaN buffers are three orders of magnitude less than those for alternative compensation methods such as heavily Beryllium (Be)-doped GaN layers [67]. Although devices have not been developed utilizing the thin films deposited from this work, the high carbon concentrations (in excess of 10^{21} cm^{-3}) have produced highly resistive GaN films with a resistivity estimated to be in excess of 10^{12} Ω-cm [68], which is an order or magnitude greater than other presently obtainable values. In addition to reducing the leakage current in the HEMTs, increased buffer resistivity results in improved device pinch-off [65] and breakdown voltages in excess of 1300 V [69].

1.4 High Electron Mobility Transistors

The HEMT is a heterojunction device which improves upon the traditional compound semiconductor transistor, the metal-semiconductor field effect transistor (MESFET). To better understand the operation of the HEMT, the operation of the silicon MESFET will first be introduced. Figure 1.10 illustrates the basic device structure of the homojunction MESFET. Typical device operation involves biasing with a drain-source voltage (V_{DS}) > 0 and gate-source voltage (V_{GS}) < 0. The channel region of the MESFET is typically doped n-type, while the contact regions are typically doped n+. When biased, electrons travel from the source to the drain. The gate bias modulates the depletion region in the channel, effectively modulating the thickness of the current-carrying channel. When the gate bias is greater than the threshold voltage (V_T), the channel becomes entirely depleted of carriers, preventing current from passing from drain to source. By modulating the thickness of the depletion region, the magnitude of the drain current can be varied as seen in equation 1.1

$$I_d = q\, n\, [1 - W_D(x)]\, v(x) \tag{1.6}$$

where q is the charge of an electron, n is the electron concentration in the channel, $W_D(x)$ is the thickness of the depletion region, and $v(x)$ is the electron velocity.

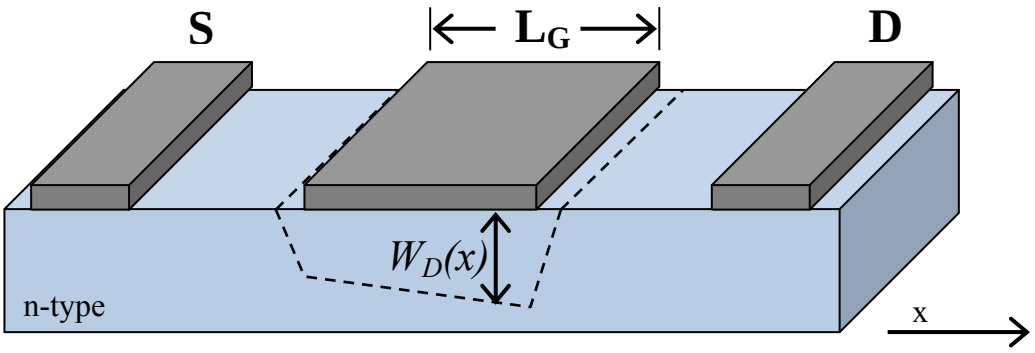

Figure 1.10: Schematic illustration of a MESFET with Vds > 0 and Vgs < 0. In the illustration, L_G represents the gate length and $W_D(x)$ is the thickness of the depletion regions with respect to the lateral position.

A HEMT follows the same basic principles as the MESFET. The main difference is that a HEMT utilizes the 2DEG formed at the AlGaN/GaN interface to carry current rather than relying on a thick n-type channel like the MESFET. Figure 1.11 shows a typical $Al_xGa_{1-x}N$/GaN HEMT. Similarly to the MESFET, electrons travel from the source to the drain and the current is modulated by the gate bias. The HEMT differs from the MESFET in that the current in a HEMT is modulated by reducing the concentration of electrons in the 2DEG rather than modulating the channel cross-section. It is the 2DEG of the HEMT that provides the benefit over the homojunction MESFET. The electrostatics responsible for populating the 2DEG in a HEMT can provide much higher electron concentrations and higher transconductance, a measure of how much applied voltage is required to modulate current flow, than possible for a MESFET. In the case of the III-Nitride material system, an AlGaN/GaN interface can result in electron sheet charge densities (N_s) of ~5 x 10^{13} /cm^2 [70], which is an order of magnitude greater than GaAs and Si technologies. The improved properties of the III-Nitride material system,

compared to traditional silicon, also provide additional benefits in current density and maximum operational frequency. Equation 1.7 expresses I_d for a HEMT in terms of charge per unit width under the gate Q_g,

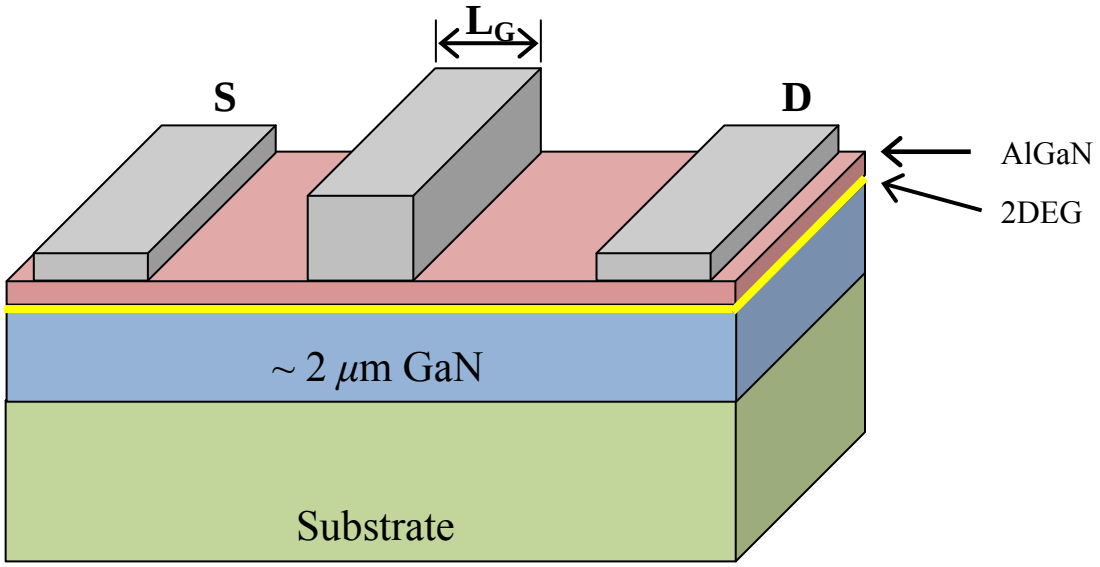

Figure 1.11: Schematic illustration of typical AlGaN/GaN HEMT device structure. The GaN buffer layer is typically unintentionally doped n-type.

$$I_d = \frac{Q_g v_{eff}}{L_G}, \tag{1.7}$$

where v_{eff} is the effective electron velocity under the gate. From equation 1.7, the transconductance of the device can be solved as,

$$g_m = \frac{\partial I_{ds}}{\partial V_{gs}} = \frac{C_{gs} v_{eff}}{L_G}, \tag{1.8}$$

where C_{gs} is the gate-source capacitance. The cut-off frequency of the device can be approximated with the transconductance by the following equation,

$$f_T = \frac{g_m}{2\pi C_{gs}} = \frac{v_{eff}}{2\pi L_G} \tag{1.9}$$

Equation 1.9 shows the dependency of device cut-off frequency (f_T) on v_{eff}, which is related to v_{sat}, illustrating the benefit of the III-Nitride material system over silicon for transistor devices. As shown previously in Table 1.1, the III-Nitride materials have v_{sat} 2.5 times greater than silicon, allowing for much higher operational frequencies. In addition, higher power transistors are possible because of the increased breakdown voltage of the III-Nitrides as compared to silicon. This higher power density compared to alternative materials allows for the III-Nitride devices to be fabricated much smaller than their silicon counterparts.

The first III-Nitride HEMT was developed in 1994 and consisted of a simple AlGaN/GaN stack [41] which utilized the polarization fields inherent in the material to form a 2DEG. The first power performance from an AlGaN/GaN HEMT was reported as 1.1 W/mm in 1996 [71]. Today, power densities have exceeded 40 W/mm through post-deposition processing improvements [42]. Epitaxially, the traditional HEMT continues to evolve as well. In 1991, Shen *et al.* inserted a thin AlN interlayer between the GaN and AlGaN layers, which exhibited increased 2DEG mobility and sheet charge density [72]. This increased in 2DEG mobility results from the elimination of alloy scattering that occurs in AlGaN alloys. Additionally, the larger band edge discontinuity that results from the insertion of an AlN interlayer provides the increase in sheet charge density.

Furthermore, additional device structures such as AlGaN/AlGaN HEMTs which utilize varying Al compositions to maintain the piezoelectric strain have been investigated [73]. Current HEMTs based on III-Nitride materials have obtained continuous wave current densities in excess of 40 W/mm at 4 GHz [42] and maximum oscillation frequency (f_{max}) of 300 GHz [43].

Although the theoretical possibilities of HEMTS are promising, there still exist issues with the structures which need to be improved to reach the full potential of the device. There are two central issues in AlGaN/GaN HEMTs performance: current slump and leakage current. Current collapse is a severe reduction in drain current, which occurs when the device is operated at high voltages. An example of current collapse is shown in Figure 1.12, illustrated by the decrease in I_d as the sampling frequency is increased. This current collapse has been attributed to surface states that exist on the surface of the AlGaN layer [74, 75]. These surface states can trap electrons and modulate the current in the channel. In this case, the surface states act as a "virtual gate" and alter the drain current through variation in the density of the trapped states. Once these surface states were identified, passivation techniques were adapted in post-processing to reduce the trapping effects of the AlGaN surface states. Since 2000, silicon nitride (SiN_x) passivation layers have become standard on almost all HEMTs [76-78], although other oxide and nitride passivation layers, such as magnesium oxide (MgO) [79, 80] and silicon dioxide (SiO_2) [81], have also been investigated. By incorporating a SiN passivation layer, the output powers at the time were increased from 9 to 11 W/mm [82]. In addition, increases in sheet charge densities [83], breakdown voltages [84] and power-added efficiencies (PAE) have been reported [84].

Additionally, device leakage can occur through leakage paths resulting from material defects. These leakage paths include interface leakage, leakage in the AlGaN capping layer, and leakage through the buffer layer. Because the 2DEG is located within approximately 70 Å of the AlGaN/GaN interface, it is paramount to maintain an abrupt and planar interface. Current loss at the interface is primarily a result of interface roughness [85, 86]. Interface roughness is the dominant source of scattering in the channel and the magnitude of the scattering increases as the Al content in the AlGaN layer increases. Figure 1.13 shows theoretical simulations plotting the effect of interface roughness on the mobility of the 2DEG, where L represents the distance between undulations along the AlGaN/GaN interface. As seen, as the roughness of the interface increases, the resulting mobility of the 2DEG is reduced because of increased scattering. Additionally, increasing the sheet charge density of the 2DEG results in a decreased mobility as the probability of scattering increases.

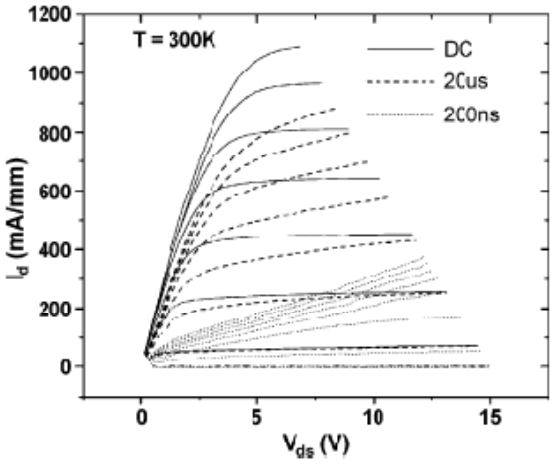

Figure 1.12: DC and pulse I-V characteristics of an AlGaN/GaN HEMT on a SiC substrate. Current collapse is seen as a decrease in I_d as the sampling frequency is increased [87].

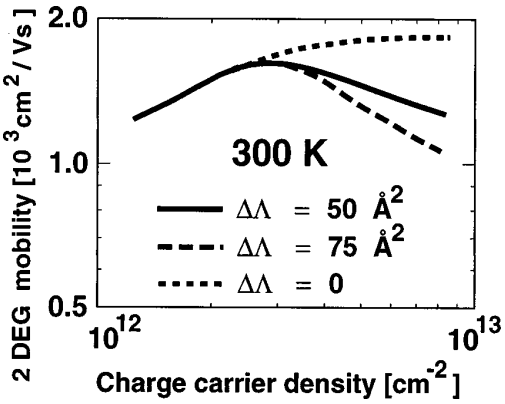

Figure 1.13: Electron mobility of the 2DEG at an AlGaN/GaN interface with increasing sheet charge density and varying interface roughness [88].

Finally, current leakage paths affecting device operation may also occur in the AlGaN capping layer or GaN buffer layer. When the device is operated at higher voltages, current paths through the buffer can manifest as a result of poor epitaxial quality. Buffer layers with poor crystalline quality can increase the magnitude of leakage current through the formation of trap states at dislocation sites [89, 90]; therefore optimization of the GaN layer is paramount. The quality of the buffer layer can be influenced by several factors including nucleation, bulk growth conditions, and thickness. III-Nitrides lack a native substrate; therefore heteroepitaxial substrates such as sapphire (Al_2O_3) [91, 92] or silicon carbide (SiC) [93, 94] are typically used. These alternative substrates have mismatches in lattice spacing with the III-Nitride films. These lattice mismatches lead to strain in the III-nitride film, thereby increasing the density of defects. A nucleation layer is typically employed to reduce the formation of defects at the substrate/film interface [95-97]. This nucleation layer has been shown to increase GaN

crystallinity when measured through X-ray diffraction (XRD), with a GaN (002) rocking curve full-width at half-maximum (FWHM) decrease from 8.2 min to 1.9 min, a 431.5% improvement [98]. Since trap states, which induce device leakage, can form at crystalline defects, this improvement in crystalline quality (reduction of defect density) will reduce device leakage. Additionally, the growth conditions used for the deposition of the GaN buffer layer can greatly affect the amount of leakage in the buffer layer. The optimization of several growth conditions, including growth temperature [99-101] and the ratio of Group V elements to Group III elements (V/III ratio) [101-103] have been shown to affect the quality of the film, and therefore the density of defects. The effect of growth temperature and V/III ratio on the resulting GaN crystalline quality is shown in Figures 1.14 and 1.15. Finally, the thickness of the GaN buffer used in the device can affect the leakage because thicker films have been found to have lower dislocation densities because of an increased probability of dislocation termination [104, 105]. Figure 1.16 illustrates the decrease in dislocation density as the thickness of the GaN buffer layer is increased. By incorporating each of the aforementioned optimizations into the epitaxial layers, the lowest leakage buffer layer possible can be achieved, greatly improving the device performance.

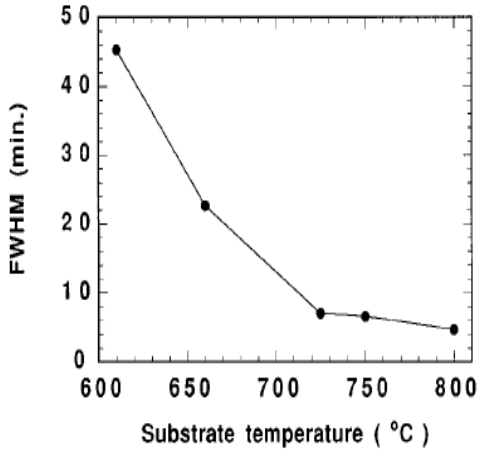

Figure 1.14: Correlation between film quality (FWHM) and growth temperature. Lower FWHM values represent an increase in crystalline quality [99].

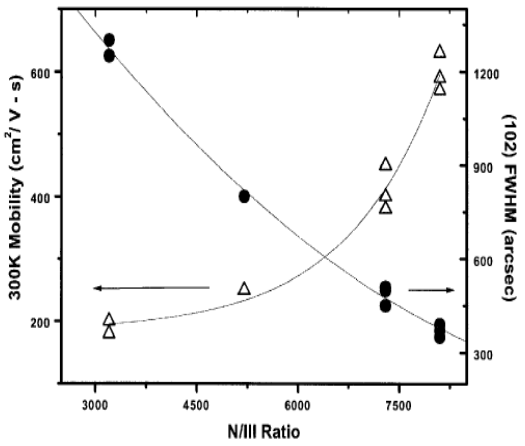

Figure 1.15: Influence of supplied V/III ratio on the crystalline quality (FWHM) and bulk mobility of GaN [103].

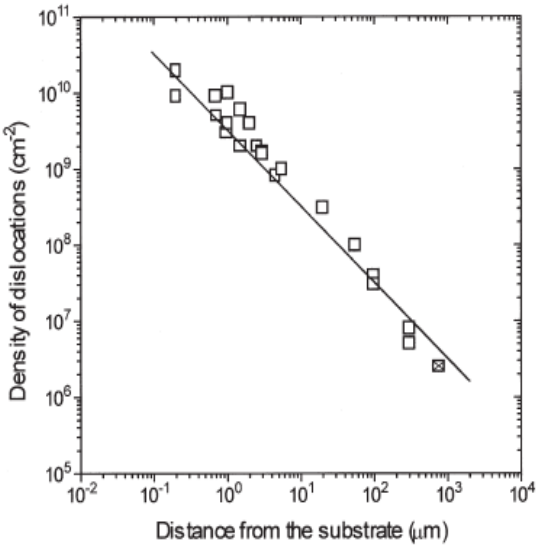

Figure 1.16: Defect density in GaN film as a function of film thickness. Graph is shown in logarithmic scale [105].

1.5 Problem Statement

NH_3-MOMBE has proven that it is capable of repeatedly producing highly resistive GaN thin films. Integration of these highly resistive films into a HEMT would result in vast improvements, specifically in reducing the leakage current of the device. Although there is a large potential impact, there are challenges associated with utilizing these carbon-doped films in transistor structures because of carbon-related trap state formation. The research in this thesis identifies and addresses challenges in the deposition of III-Nitrides by NH_3-MOMBE and addresses their possible utilization in transistor structures.

This thesis is arranged as follows:

- Chapter 2 describes the utilization of molecular hydrogen during the growth of GaN by NH_3-MOMBE, and reports its effect on the growth rate and carbon incorporation in the films.

- Chapter 3 describes the growth of $Al_xGa_{1-x}N$ by NH_3-MOMBE and identifies the effect of growth conditions on a variety of films properties including composition, surface cracking, film strain, growth rate, surface morphology, and crystalline quality.

- Chapter 4 describes the NH_3-MOMBE growth kinetics for the deposition of $Al_xGa_{1-x}N$, specifically the effect of Al on the catalyzation of NH_3, as well as the effect of the AlGaN growth regimes on film properties.

- Chapter 5 describes the high-temperature deposition of both $Al_xGa_{1-x}N$ and GaN and the effect of these increased growth temperatures on the growth rate and surface morphology of the films.

- Chapter 6 investigates the influence of GaN growth conditions on the incorporation of carbon. Specifically, the effect of both growth temperature and V/III ratio was investigated.

- Chapter 7 demonstrates the use of atomic hydrogen as a means of liberating adsorbed ethyls during the growth of GaN, and its influence on the carbon incorporation.

- Chapter 8 describes the deposition of several different III-Nitride transistor structures and their influence on the formation of a 2DEG.

- Chapter 9 describes the optical characterization of carbon-doped GaN through photoluminescence and photo-capacitance measurements and determines the influence of carbon on the formation of trap states.

- Chapter 10 details the conclusions resulting from this work and outlines future research directions to further extend the range of this thesis.

CHAPTER 2: INVESTIGATION INTO THE USE OF MOLECULAR HYDROGEN ON CARBON INCORPORATION

2.1 Introduction

III-nitrides grown by ammonia-based MBE presented significant promise in the last decade as a result of their high growth rates and excellent device properties. Interest has been renewed in ammonia-based MBE because of the perceived benefits in scalability over commercial plasma-based MBE. NH_3-MOMBE may provide a method to overcome the current limitations in commercial epitaxy while maintaining the benefits of traditional MBE. However, efficiency problems associated with ammonia nitridation and unintentional carbon contamination from metal-organic precursors must be overcome. While the majority of this thesis deals with applications (HEMTs) where carbon is used beneficially, the channels of HEMTS and other devices (LEDs, LASERS, etc…) cannot tolerate excessive carbon. For this reason, a method of controllably reducing or even eliminating carbon contamination is sought. Although theoretical and experimental studies of atomic hydrogen usage during GaN growth exist, there are still few experimental results demonstrating the effect of molecular hydrogen on the growth of GaN.

In this chapter, the effects of H_2 introduction during several growth steps of GaN grown via NH_3-MOMBE are reported. The results presented demonstrate the effect of a H_2 surface pre-treatment with varying durations and temperatures on film quality and

growth rate. Also, secondary ion mass spectroscopy (SIMS) data shows an increased carbon concentration when H_2 is introduced during the bulk film growth.

2.2 Experimental Procedure

The details regarding substrate preparation are discussed in Appendix A.1. For the growth of GaN, NH_3 and TEGa were used as the precursors, without the use of carrier gases. H_2 and NH_3 were regulated with a mass flow controller, while TEGa was controlled by maintaining a pressure behind a 660 μm orifice [54]. The precursor delivery system and conversion of source pressures are outlined in Appendix A.2. All pressure references for TEGa presented herein refer to its pressure behind the orifice.

Initial samples grown for these experiments were deposited on c-plane (0001) sapphire substrates. Following a 200 ºC anneal, the substrate was heated to pre-treatment temperature while exposed to 10 standard cubic centimetres per minute (sccm) of H_2. The H_2 pre-treatment step was conducted with varying durations (10 and 30 min) and temperatures (500, 800, 1000 ºC). The substrate temperature was reduced to 800 ºC at 1.5 ºC/s while exposed to 100 sccm of NH_3 for a subsequent 10 min sapphire nitridation. Following the nitridation, the temperature was decreased to 540 ºC at 1.5 ºC/s for the GaN buffer layer, grown for 16 min using 100 sccm NH_3 and 0.10 Torr (~0.119 sccm) TEGa. The buffer is followed by a ramp anneal to 870 ºC at 0.5 ºC/s with 25 sccm of NH_3. After the ramp, a 30 min GaN layer is deposited using 25 sccm NH_3 and 0.32 Torr (~0.38 sccm) TEGa.

Samples grown for the carbon incorporation experiments were deposited on ~3 μm GaN templates. Following a 200 ºC anneal, the substrate temperature was raised to 870 °C at 1.5 °C/s under 25 sccm of NH_3. The temperature ramp is followed by an initial GaN deposition for 60 min using 26 sccm NH_3 and 0.16 Torr TEGa. Following the hydrogen-free GaN deposition, a second GaN layer was deposited with the same conditions, yet with the introduction of 10 sccm of H_2.

2.3 Effect of Hydrogen Pre-Treatment on Crystalline Quality and Growth Rate

RHEED images were taken of samples that were pre-treated in H_2 and subsequently nitrided at varying temperatures (1000, 800, 550 °C). The RHEED images were obtained by transferring the samples to a RIBER II MBE system, equipped with a Staib RHEED system. The RHEED images are displayed in Figures 2.1 and 2.2. Both the H_2 un-treated and treated samples showed regions where nitridation was incomplete indicating a severe weakness of vacuum use of ammonia (low flow ammonia as compared to enormous flows used in MOCVD) . This incomplete nitridation weakness manifests itself in the subsequent GaN films as poor crystal quality.

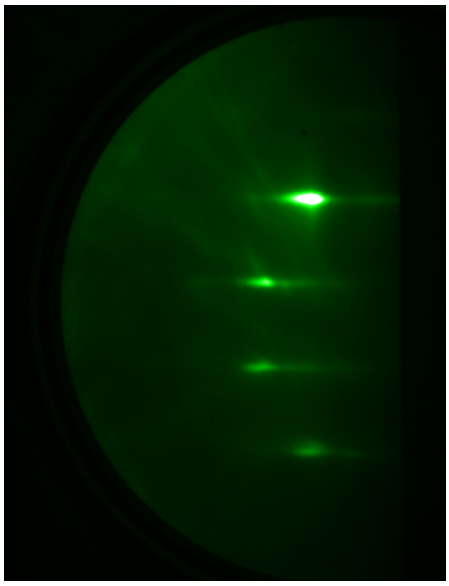

Figure 2.1: RHEED image of hydrogen-pretreated sapphire substrate following a 10-min. nitridation at 550 °C with an NH_3 flow rate of 100 sccm. The RHEED image indicates regions of the sapphire substrate have been converted to AlN.

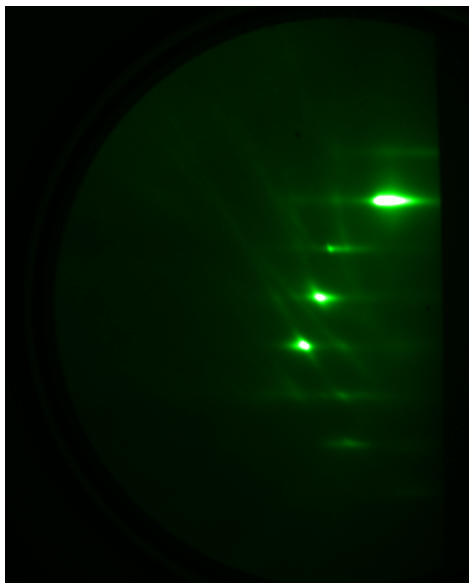

Figure 2.2: RHEED image of hydrogen-pretreated sapphire substrate following a 10-min. nitridation at 550 °C with an NH_3 flow rate of 100 sccm. The RHEED image indicates that regions of the sapphire substrate have not been converted to AlN.

Table 2.1: XRD rocking curve FWHM of GaN (002) films with H_2 pre-treatment.

H_2 Pre-Treatment Temperature	
1000 °C	550 °C
28.6 arcmin	41.25 arcmin

XRD rocking curve FWHM of GaN (002) with H_2 pre-treatments is shown in Table 2.1. As the temperature of the H_2 pre-treatment is increased from 550 to 1000 °C, the subsequent GaN (002) FWHM is decreased by ~30 %. This increased film quality is suspected to be the result of a more complete nitridation process, which was unable to be quantified by RHEED analysis. One possible explanation of this improvement in the nitridation process is the chemical reduction of the oxidized sapphire surface in the presence of H_2, which results in an improved, yet incomplete conversion to AlN. The more complete nitridation of the sapphire reduces the strain in the subsequent GaN film, thereby increasing the quality of the film. However, as confirmed by RHEED, neither H_2 treatment was sufficient to produce complete nitridation and thus resulted in poor quality films.

Table 2.2: Growth rate for GaN films with H_2 pre-treatment.

H_2 Pre-Treatment Temperature			
500 °C		1000 °C	
10 min	30 min	10 min	30 min
0.29	0.41	0.21	0.18

*Growth rates are in μm/hr

In addition to an increase in the quality of the subsequent GaN film, an increase in the growth rate of the GaN is observed with H_2 pre-treatment. Film thickness was measured *ex situ* on a KLA Tencor Alpha-step profilometer. The change in growth rate differs depending on the duration and temperature of the H_2 pre-treatment. As seen in Table 2.2, the growth rate of the GaN film decreases when the H_2 pre-treatment temperature is increased from 500 to 1000 °C. A decrease in growth rate of ~56 % is measured for the films treated for 30 min at 1000 °C, while the growth rate of the films treated for only 10 min decreased ~28.6 %. The change in growth rate is suspected to be a result of the polarity inversion caused by the H_2 pre-treatment temperature. Due to the inefficient use or ammonia for nitridation of sapphire and the attendant crystal quality concerns, unless otherwise noted, all subsequent growths were performed on GaN templates to provide a homoepitaxial substrate.

2.4 Effect of Hydrogen on Carbon Incorporation

With recent success in the control of carbon contamination and growth rate through the use of atomic hydrogen during GaN growth, a study was undertaken to determine the effect of H_2 on the growth of GaN in MOMBE. It should be noted that XRD indicated that GaN grown on GaN templates mimicked the quality of the template, therefore proving that MOMBE is capable of high quality growth but incomplete

ammonia nitridation, as discussed in the previous section represents a material quality limiting step at present. To determine the effect of H_2 on GaN carbon incorporation, a two layer structure was grown with one layer exposed to 10 sccm of H_2 during growth. SIMS analysis was conducted by Evans East Analytical Group, using a Cs^+ primary ion beam to determine carbon concentrations in the individual layers, as seen in Figure 2.3. A 57 % increase ($1.5 \times 10^{19} \rightarrow 3.5 \times 10^{19}$ cm^{-3}) in carbon was observed when H_2 was present during growth.

Moreover, a decrease of 19 % in the growth rate was observed in the presence of H_2, as measured by *in situ* laser interferometry shown in Figure 2.4. This decrease in growth rate is consistent with results in MOCVD-grown GaN when H_2 is used as a carrier gas. The linear attenuation of the reflectance intensity, independent of H_2 flow rate, suggests that H_2 is not contributing to additional surface roughening. Instead, this attenuation is believed to be the result of deposition on the incident laser viewport. Although the exact reason for these H_2 effects on growth rate is unclear, the available Ga may be reduced in the presence of H_2 as growth is Ga-limited. This is consistent with reports of increased gallium desorption in the presence of excessive H_2.

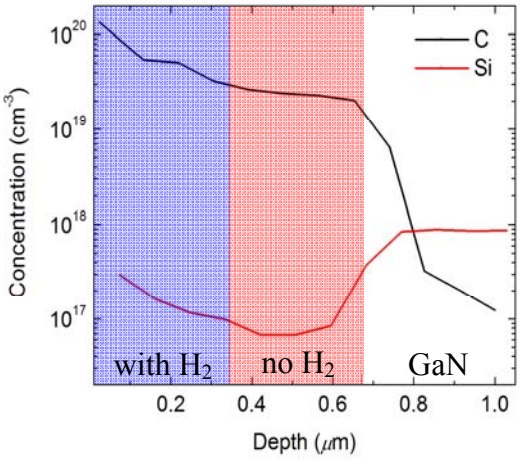

Figure 2.3: Carbon concentration, as determined by SIMS, for GaN epilayers grown with and without H_2.

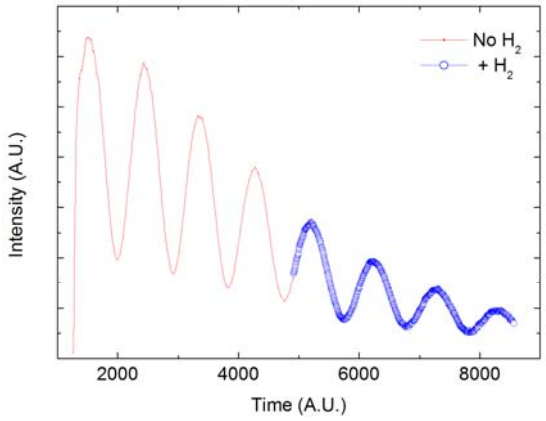

Figure 2.4: Laser interferometry data showing a decrease in the growth rate of GaN when grown in the presence of H_2.

2.5 Conclusions

To observe the effect on both the film quality and carbon concentrations, H_2 was introduced during various growth stages of GaN growth. Results indicate that H_2 used as a pre-treatment prior to ammonia nitridation of sapphire decreases the XRD rocking curve FWHM by ~30 % when treated at 1000 °C. The pre-treatment is speculated to increase the efficiency of the ammonia nitridation, resulting in an improvement in the resulting GaN film quality. Also, when pre-treated at 1000 °C, a growth rate decrease of ~56 % is observed for samples treated for 10 min, while samples treated for 30 min showed a growth rate decrease of ~29 %. The decrease in the growth rate is expected to be the result of polarity inversion caused by the high temperature sapphire pre-treatment. The effect of molecular hydrogen on the carbon concentration of GaN was also investigated on a two-layer GaN structure with one layer exposed to H_2. SIMS results show that the introduction of hydrogen during growth results in increased GaN carbon incorporation, as well as a reduction in the growth rate. The 57 % increase in carbon incorporation and 19 % decrease in growth rate of GaN are attributed to increased gallium desorption when in the presence of excessive H_2. Investigation into the effect of atomic hydrogen on the control of carbon incorporation are presented in Chapter 6.

CHAPTER 3: GROWTH AND CHARACTERIZATION OF $Al_xGa_{1-x}N$

3.1 Introduction

While the highly resistive (~10^{12} Ω-cm) NH_3-MOMBE GaN has shown potential as a low-leakage buffer for HEMTs [54], the realization of these electrical devices is not possible without an AlGaN capping layer. AlGaN grown by NH_3-MOMBE provides a significant challenge, because although few publications of GaN grown by NH_3-MOMBE exist [53, 100, 106], there has been no prior publications on the growth of $Al_xGa_{1-x}N$ via NH_3-MOMBE. $Al_xGa_{1-x}N$ is a functional alloy because of its direct, and tunable bandgap, which spans from ~3.42 eV to ~6.2 eV. To utilize the benefits of a tunable bandgap, precise control over the growth rates and compositions of $Al_xGa_{1-x}N$ films is imperative. AlGaN is routinely grown at lower Al compositions, yet the growth of AlGaN at higher compositions proves more difficult [107, 108]. Because of its lower growth pressures compared to MOCVD, NH_3-MOMBE is advantageous for the growth of $Al_xGa_{1-x}N$ since the possibility of parasitic gas phase reactions between NH_3 and TEAl is eliminated [106-108]. As described previously, NH_3-MOMBE also has advantages over traditional MBE since the use of gaseous precursors increases the potential operational time compared to solid sources that need periodic opening of the vacuum system, which requires reloading and baking as well as subsequent conditioning of sources and chamber.

In this chapter, the first reported instance of $Al_xGa_{1-x}N$ layers grown via NH_3-MOMBE is described. The films were grown across the entire range of compositions from GaN to AlN. The films were characterized extensively to determine the effect of growth conditions on a variety of film properties; including strain, composition, surface morphology, crystalline quality and growth rate.

3.2 Experimental Procedure

All films were grown in a custom NH_3-MOMBE showerhead reactor [54] on Lumilog silicon-doped GaN templates**.** The details regarding sample preparation and cleaning procedures are discussed in Appendix A.1. For the growth of AlGaN films, NH_3, TEGa and triethylaluminum (TEAl) were used as the precursors without the use of carrier gases. The specifics of the precursor flow control system and flow rate calculations are explained in Appendix A.2. Herein all values for TEGa and TEAl will be presented as flow rates.

Two sets of $Al_xGa_{1-x}N$ growths were conducted for this experiment. An initial set involved a 60 min $Al_xGa_{1-x}N$ layer, which was used to determine composition and growth rate. The second set of films was grown to a thickness of ~850 Å to study strain, morphology and crystalline quality. Besides the growth rate, all figures presented herein are from data taken from the constant thickness samples.

Once the samples were annealed in the growth chamber, the temperature was increased to a growth temperature of 870 °C, at a rate of 2 °C/s under NH_3. For all

growths, the total metal flux was maintained at 0.14 Torr (~0.017 sccm) with only the ratio of Al to Ga being altered. The bulk layers were grown at a temperature of 870 °C with an NH_3 flow rate of 26 sccm, resulting in a V/III ratio of ~156. The average chamber pressure during growth was ~1 x 10^{-5} Torr. After growth, the temperature was decreased to 15 °C at a rate of 4 °C/s.

3.3 Growth of $Al_xGa_{1-x}N$

To study the incorporation of Al into $Al_xGa_{1-x}N$ grown by NH_3-MOMBE, the entire range of Al compositions was grown. To accurately measure the composition of the strained $Al_xGa_{1-x}N$ films, Equation 3.1 was solved iteratively to determine the composition to within ± 2 % [109].

$$\frac{c_{exp}-[x\cdot c_{AlN}+(1-x)c_{GaN}]}{x\cdot c_{AlN}+(1-x)c_{GaN}}\,\frac{x\cdot a_{AlN}+(1-x)a_{GaN}}{a_{exp}-[x\cdot a_{AlN}+(1-x)a_{GaN}]}=-\frac{2\cdot[x\cdot C_{13}^{AlN}+(1-x)C_{13}^{GaN}]}{x\cdot C_{33}^{AlN}+(1-x)C_{33}^{GaN}} \quad (3.1)$$

It was assumed that the stiffness coefficients $\left(C_{13}^{AlN}=100, C_{33}^{AlN}=392, C_{13}^{GaN}=82, C_{33}^{GaN}=411\right)$ are linearly related to the composition of the $Al_xGa_{1-x}N$ film. Theoretical lattice parameters for GaN (a_{GaN} = 3.189 Å, c_{GaN} = 5.185 Å) and AlN (a_{AlN} = 3.112 Å, c_{AlN} = 4.982 Å) are combined with measured lattice constants c_{exp} and a_{exp}, determined from reciprocal space maps, and the equation is solved iteratively to determine *x*, the $Al_xGa_{1-x}N$ film composition. The composition values were

then verified using fitting of the XRD 2θ-ω $Al_xGa_{1-x}N$ (002) scans with the strain in the films included in the fits. Figure 3.1 shows the solid phase Al composition (X^S_{Al}) with respect to the gas phase composition of Al (X^G_{Al}). The entire range of Al compositions was attainable by adjusting the Ga/Al ratio, with a linear trend line, with a slope of 2, fitting the curve between $0.2 < X^G_{Al} < 0.8$.

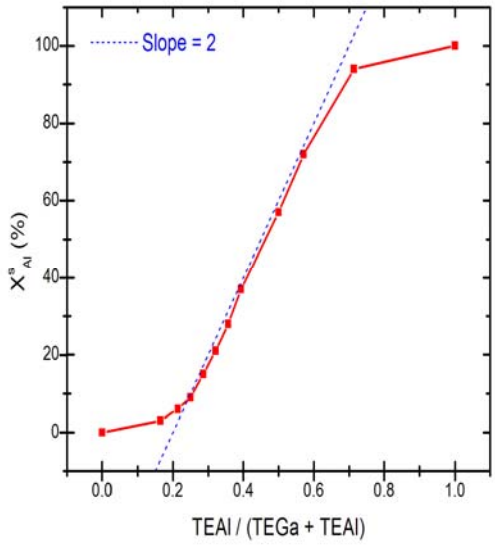

Figure 3.1: Aluminum content in $Al_xGa_{1-x}N$ versus gas phase aluminum composition for NH_3-MOMBE.

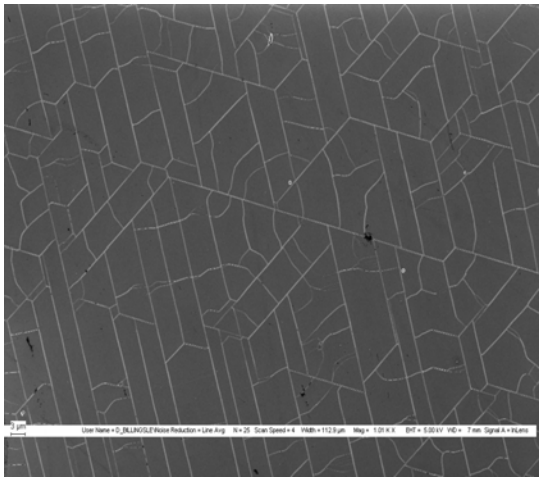

Figure 3.2: Example of surface cracking in $Al_{0.72}Ga_{0.28}N$, as seen by scanning electron microscopy at 1000x magnification.

Cracking occurs in $Al_xGa_{1-x}N$ samples with Al compositions greater than ~30 %, although very low density microcracks can be seen in films with Al compositions above ~15 %. It is unknown whether the cracking is a result of the tensile stress induced by the lattice mismatch [110, 111] or a result of the difference in coefficients of thermal expansion between GaN and AlN [110, 112]. An example of cracking seen via scanning electron microscopy (SEM) in an $Al_{0.72}Ga_{0.28}N$ film is shown in Figure 3.2. Cracking preferentially occurs along the $<11\bar{2}0>$ directions with smaller cracks scattered throughout. The cracks oriented along the $<11\bar{2}0>$ direction have varying lengths and can extend up to several millimeters. These results agree with those seen in other works [110].

Reciprocal space mapping (RSM) was conducted via XRD around the $(\bar{1}04)$ reflection to calculate the strain in the $Al_xGa_{1-x}N$ films, relative to the GaN [113]. The relative strain was obtained through Equation 3.2

$$\text{Relative Strain} = 1 - \frac{a_{GaN} - a_{AlGaN}}{a^0_{GaN} - a^0_{AlGaN}} \tag{3.2}$$

where a^0_{GaN} = 3.185 Å, and a^0_{AlN} = 3.112 Å. The scattering vectors Q_x and Q_y, obtained from the RSMs, were used to calculate a_{GaN} and a_{AlGaN} through Equation 3.3.

$$a = \frac{\lambda_{K\alpha 1}}{\sqrt{3} \cdot Q_x} \tag{3.3}$$

In films exhibiting cracking, the density of cracks was estimated through histogram analysis of the SEM images by highlighting the surface cracks to determine an area percentage covered by cracks. The density of cracks and relative strain in the film were plotted against the aluminum composition, as seen in Figure 3.3. For fully strained films the relative strain is 1, where a strain of 0 corresponds to a fully relaxed sample. As seen in the graph, the onset of cracking corresponds with the alleviation of strain in the films. Although cracking reduces strain in the films, the strain is never completely eliminated. The cracking density saturates at ~5 % of the total area being composed of cracks, which corresponds to an aluminum composition of ~80 % or greater.

Figure 3.4 shows the growth rate of $Al_xGa_{1-x}N$ versus the Al composition. The growth rate of the $Al_xGa_{1-x}N$ films were measured *in-situ* through optical interferometry (OI) and verified *ex-situ* by profilometry. The change in refractive index with Al composition was taken into account when the growth rates were calculated. The growth rate of $Al_xGa_{1-x}N$ is suspected to be controlled by the competition between the increased

cracking efficiency of ammonia in the presence of Al and the increased sticking coefficient of Al over Ga [114, 115]. Since the films are already grown in the N-rich regime, the increased cracking efficiency of ammonia acts to slow the growth rate of films grown at low Al compositions. This decreased growth rate is most likely a result of either increased nitrogen recombination [54] or ammonia and/or ammonia radical (NH_x) site blocking [116] in excessive nitrogen-rich environments, which ultimately reduces the TEGa β-elimination reaction. These catalytic effects dominate over the increased sticking coefficient of Al until the Al composition is above ~30 %. Since the total group-III flux was held constant in these experiments, the decreased desorption of Al species over Ga at 870 °C results in an increased growth rate. Thus, when the growth of $Al_xGa_{1-x}N$ is Al-dominated, the increased metal coverage resulting from the high relative sticking coefficient of Al is able to efficiently consume the increased available nitrogen resulting from the aforementioned catalytic effect and the growth rate increases. When the growth rate begins to increase at ~30 % Al composition, significant increases in the RGA signals for mass 15 and 30, attributed to ethane, are seen downstream of the growth surface. The increase in desorption of ethane at higher Al composition films corresponds to the increase in growth rate, presumably resulting from a reduction in hydrocarbon site blocking. This desorption of hydrocarbons may also lead to a decrease in carbon incorporation into the film, which has been seen in other work on this system.

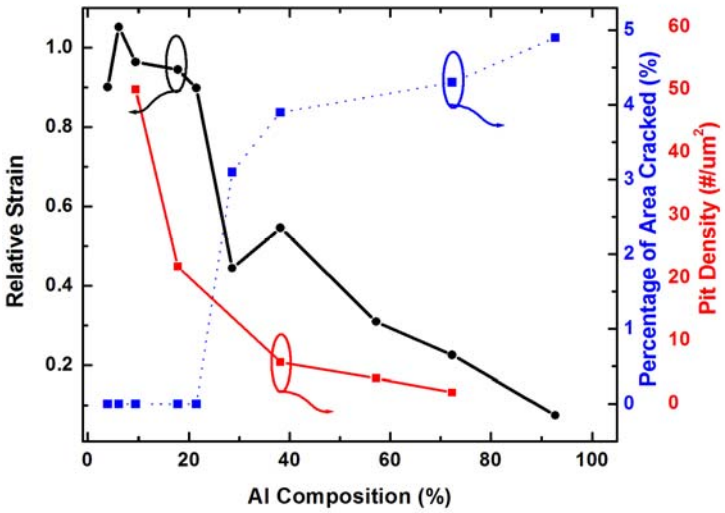

Figure 3.3: Relative strain, dislocation pit density and average crack density of $Al_xGa_{1-x}N$ versus aluminum composition for 85 nm thick films.

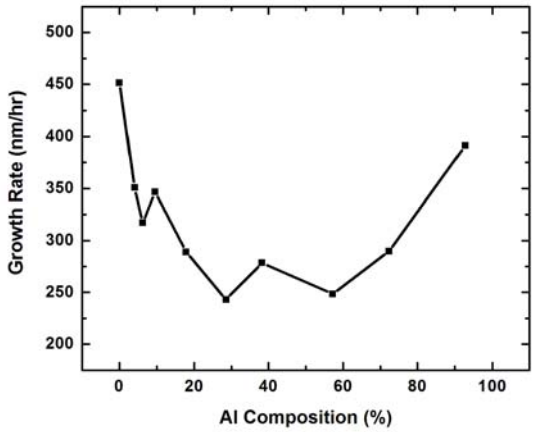

Figure 3.4: Growth rate variations in $Al_xGa_{1-x}N$ as a function of the solid aluminum composition.

3.4 Morphology and Crystal Quality of $Al_xGa_{1-x}N$

Symmetric and asymmetric XRD rocking curve FWHMs of $Al_xGa_{1-x}N$ films were used to determine the crystalline quality of the deposited films. Figure 3.5 plots the symmetric (002) and asymmetric (104) FWHMs of the $Al_xGa_{1-x}N$ films with respect to the Al composition. Data points obtained for $Al_{0.02}Ga_{0.98}N$ were intentionally disregarded because of the difficulty in separating x-ray contributions from GaN and the AlGaN peaks. The (002) FWHM results mimic the FWHM of the GaN template, indicating the GaN films are of high quality, and are limited by the quality of the growth template. The immediate increase of asymmetric FWHM with the introduction of aluminum suggests that the defect density is increased when aluminum is incorporated into the film.

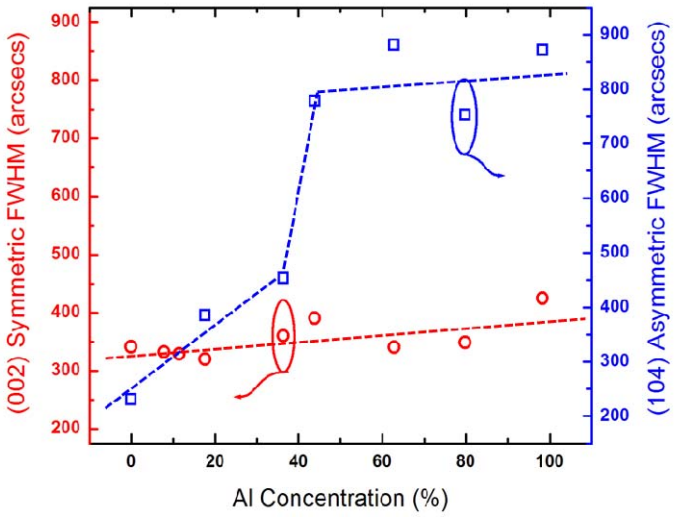

Figure 3.5: Symmetric (002) and asymmetric (004) FWHMs for $Al_xGa_{1-x}N$ as a function of the solid aluminum composition.

Atomic force microscopy (AFM) was used to determine the morphology and roughness of the $Al_xGa_{1-x}N$ films. The films clearly show morphology variations as more Al is incorporated, as seen in Figure 3.6. For pure GaN growth, the film is grown under N-rich conditions, which leads to a heavily pitted surface morphology as described elsewhere as being terminated at threading dislocations [117]. Thus, the pit density under N-rich conditions is correlated with the number of dislocations in the film. A polarity etch in hot potassium-hydroxide (KOH) was conducted to assure that the film maintained Ga-polar growth [118, 119]. When Al is introduced to the gas phase, the cracking efficiency of the ammonia is increased [115]. This increased nitrogen abundance at the surface results in more heavily pitted morphologies when $X^S_{Al} < 0.15$, as a result of the more N-rich growth conditions. When $X^S_{Al} = \sim 0.15$, the formation of microcracks is seen in the AFM scans. These microcracks are only nanometers in length and do not contribute to a significant reduction in the relative strain of the film, but they do contribute to the reduction of the dislocation pit density. The reduction of dislocation pits is suspected to be a result of dislocation gettering by the surface cracks. The dislocation pit density as a function of the Al composition is shown in Figure 3.3. The density of pits in the films steadily decreases as Al composition and crack density increases. At the onset of microcrack formation, the rms roughness decreases by ~50 % and atomic step edges are visible, mimicking the morphology of the GaN templates. An example of these atomic steps is shown in Figure 3.7. As X^S_{Al} increases beyond 0.5, the films become heavily cracked, with regions between the cracks having an rms roughness of less than 0.5 nm. In films with $0.5 > X^S_{Al} > 0.9$, the surface pits attributed to N-rich growth are

eliminated, and the pitting seen in the AFM scans is suspected to originate solely from the propagation of screw dislocations from the GaN template. In these cases, the density of pits in the $Al_xGa_{1-x}N$ film is approximately equal to pitting in the GaN template. When $X^S_{Al} > 0.9$ the film quality (morphology, XRD) quickly degrades, resulting in a heavily cracked film with a granular growth morphology. This granular morphology is most likely a result of the low mobility of Al adatoms at the un-optimized growth temperature. The film degradation is verified by both the symmetric and asymmetric FWHMs, which increase to their highest values over the entire range of $Al_xGa_{1-x}N$ films.

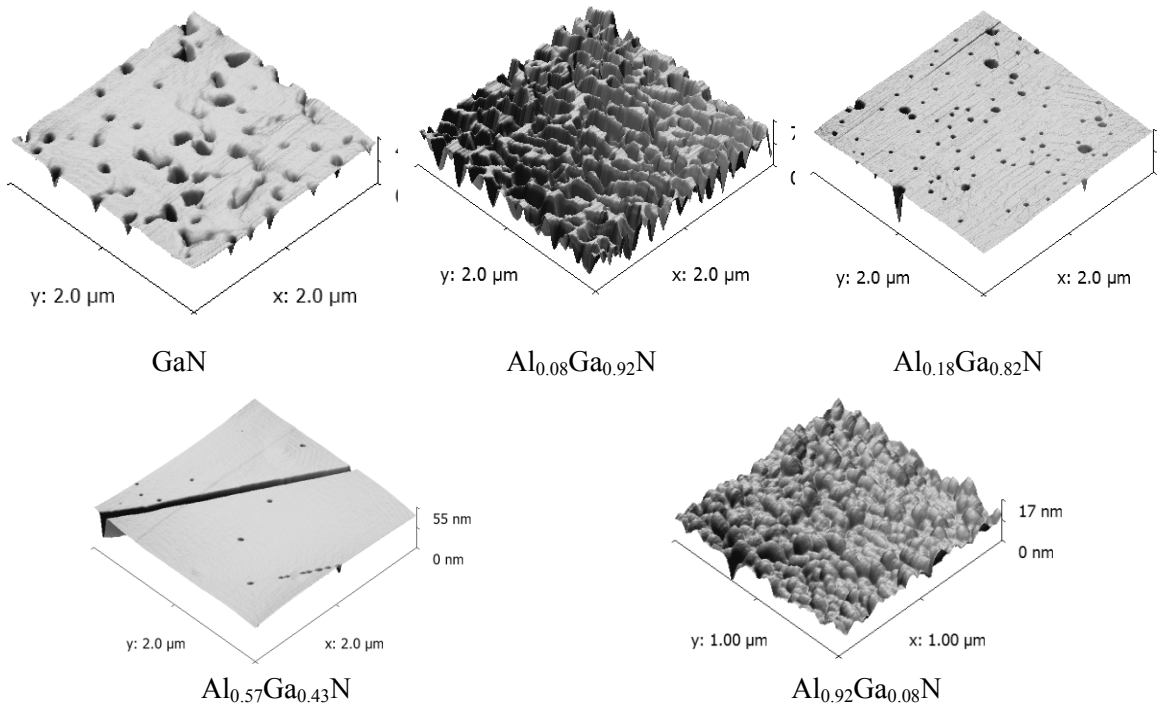

Figure 3.6: Representative AFM scans showing the morphology progression with increasing aluminum composition in $Al_xGa_{1-x}N$ films.

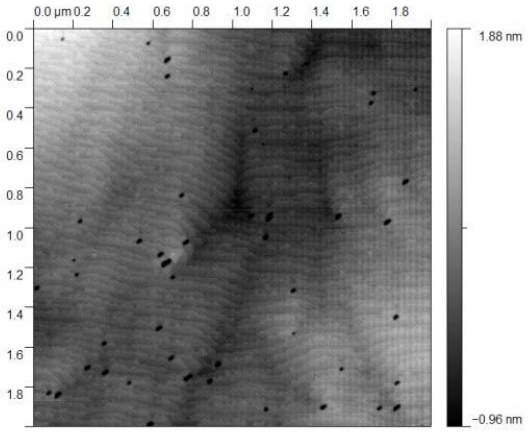

Figure 3.7: An example of atomic steps seen between surface cracks in AFM of $Al_{0.72}Ga_{0.28}N$ film.

3.5 Conclusions

The first reported case of $Al_xGa_{1-x}N$ ($0 < x < 1$) grown via NH_3-MOMBE was introduced. AlGaN films were deposited throughout the Al composition range and characterized extensively via XRD, SEM, AFM, and OI. XRD FWHMs were found to range from 300 – 450 arcsecs, with the GaN template FWHM of ~320 arcsecs, which indicates that the $Al_xGa_{1-x}N$ films mimic the quality of the template. The growth rates of the $Al_xGa_{1-x}N$ films reached a maximum of 0.4 μm/hr for $Al_{0.92}Ga_{0.08}N$, and decreased to 0.25 μm/hr for $Al_{0.3}Ga_{0.5}N$. The competing mechanisms of increased ammonia cracking and increased Al sticking coefficient over Ga were identified as the primary causes for the growth rate variations. Ammonia site blocking and nitrogen recombination that result from the excessive nitrogen produced from the catalytic effect of Al on NH_3 are

suspected to be responsible for the growth rate reduction at lower Al compositions. At higher Al compositions, the growth rate increases and is accompanied by an increase in desorption of ethane, indicating a reduction in hydrocarbon site blocking. Surface cracking along the <11$\bar{2}$0> planes occurred in $Al_xGa_{1-x}N$ films with Al compositions greater than 30 %. The cracking was found to partially relieve strain in the films, as calculated from reciprocal space maps around the ($\bar{1}$04) reflection. The crack density is also found to increase with increasing Al composition with a maximum crack area of ~5 %. The morphology and density of dislocation pits were found to be dependent on Al composition, with the pit density decreasing with increased Al composition. The decrease in pit density is attributed to the dislocation gettering property of the surface cracks. This study provides the basis for further studies on the growth of $Al_xGa_{1-x}N$ via NH_3-MOMBE. Further optimization of the growth parameters is necessary because of the complexities of the introduction of Al, namely its catalytic effect on NH_3 as well as its increased sticking coefficient over Ga. In the following chapter, these complex kinetics are explored and quantified to better understand the growth of AlGaN by NH_3-MOMBE.

CHAPTER 4: GROWTH KINETICS OF $Al_xGa_{1-x}N$ GROWN VIA AMMONIA-BASED METAL-ORGANIC MOLECULAR BEAM EPITAXY

4.1 Introduction

As described in the previous chapter, we have reported the first AlGaN films grown by NH_3-MOMBE [120]. The complex growth chemistry and lack of gas phase pyrolysis in NH_3-MOMBE complicates the growth of AlGaN. To consistently obtain the precise AlGaN compositions and thicknesses required for HEMT devices, a proper understanding of the growth kinetics of AlGaN grown via NH_3-MOMBE must be obtained. While NH_3-MOMBE provides challenges, our interest in this growth system is rooted in its unique capabilities over other deposition techniques. The vacuum of MOMBE eliminates parasitic gas phase chemical reactions that occur in MOCVD that complicates the control of AlGaN composition [100, 107, 108]. Competitive reactions between ammonia and reactant species, as well as their temperature dependencies, complicate growth in an NH_3-MOMBE environment. Proper understanding of these competitive effects is vital for the consistent control and growth of high quality AlGaN films by NH_3-MOMBE.

In this chapter, the growth regimes for AlGaN growth were determined through growth rate measurements and the characteristics of AlGaN films grown in various regimes were examined. It was determined that the introduction of Al into the gas phase

increases the catalyzation of NH_3, which increases the range of N-rich growth conditions, thereby extending the range of optimal growth conditions for the growth of $Al_xGa_{1-x}N$.

4.2 Experimental Setup

All films were grown in a custom NH_3-MOMBE showerhead reactor [54] with a base pressure of 5 x 10^{-9} Torr. The details of the sample cleaning and preparation are discussed in Appendix A.1. For the growth of AlGaN, NH_3, TEGa, and TEAl were used as precursors, introduced without carrier gases. The specifics of the gas delivery system and precursor pressure conversion are detailed in Appendix A.2. Herein, all TEGa and TEAl fluxes are presented as flow rates, in sccm.

Three sets of growths were conducted, with typical growth pressures of ~4 x 10^{-6} Torr, resulting in growth in the molecular flow regime. The initial set involved the growth of both GaN and AlGaN at 770 and 860 °C with metal flow rates ranging from 0.05 – 0.60 sccm, which were used to determine the growth rate. For the growth of AlGaN, the Al flow rate remained at 20 % of the total metal flow rate. The second set involved the growth of AlGaN at 860 °C with identical growth conditions to the previous set, except that the TEAl flow rate was varied to 25 % and 30 % of the total metal flow rate to examine growth rate variations associated with Al gas phase compositions. After determining the AlGaN growth regimes at both 770 and 860 °C, a third set of representative samples were grown in each regime to a uniform thickness of ~500 nm.

These representative samples were characterized via AFM and XRD to determine the effect of growth regime on surface morphology and aluminum compositions.

4.3 Effect of Al on Growth Regimes

Figure 4.1 and Figure 4.2 show the optical interferometer determined growth rates for both GaN and AlGaN grown at 770 and 860 °C, respectively. Error bars have been included in all growth rate graphs to compensate for variations in the refractive index with Al composition. In all cases, the growth rate increases linearly with the total metal flow rate until a maximum growth rate is achieved. This region where the growth rate slope is positive represents the N-rich growth regime. The local maximum denotes the transition where the growth regimes transition from N-rich to metal-rich growth [121, 122]. This growth rate transition point represents stoichiometric growth conditions, where the active N is equal to the active Ga ($N_{effective} = Ga_{effective}$). In the metal-rich regime, a drastic decrease in the growth rate can be seen in several of the growth rate curves. This decrease in growth rate is attributed to the formation of Ga droplets that results in excessive Ga accumulation on the surface [122, 123], which acts to block available surface sites, decreasing the overall growth rate.

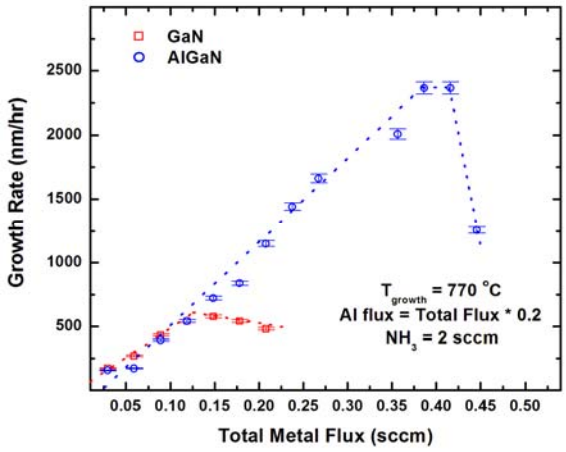

Figure 4.1: Growth rate of GaN and $Al_xGa_{1-x}N$ at 770 °C as a function of the total metal flow rate with an ammonia flow rate of 2 sccm.

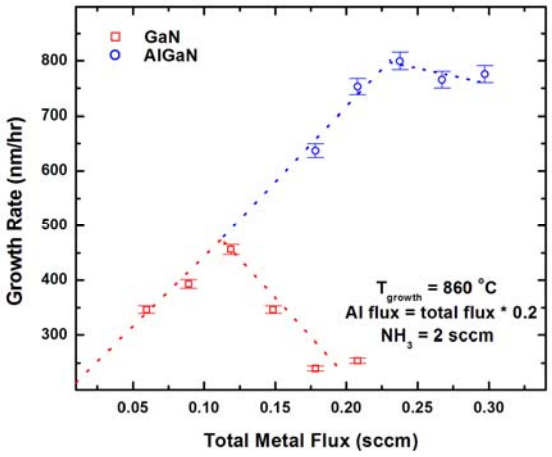

Figure 4.2: Growth rate of GaN and $Al_xGa_{1-x}N$ at 860 °C as a function of the total metal flow rate with an ammonia flow rate of 2 sccm.

By defining the stoichiometric point for all cases, the efficiency at which the ammonia is utilized in the formation of GaN can be calculated. This efficiency is calculated at each growth temperature based on the total metal flow rate necessary for the effective V/III ratio to equal unity divided by the actual ammonia flow. Because of significant species desorption, the calculated efficiencies will not be accurate at the higher growth temperature. Therefore, the calculated values are used solely to indicate the increase in efficiency for the growth of AlGaN as compared to the GaN.

Table 4.1: Extracted NH_3 utilization efficiencies for GaN and $Al_xGa_{1-x}N$ grown at both 770 and 860 °C.

	GaN	**AlGaN**
770 °C	8.3 %	20.7 %
860 °C	6.6 %	13.2 %

The ammonia utilization efficiencies for both temperatures are displayed in Table 4.1. At both growth temperatures, the utilization efficiency of ammonia is 2–2.5 times greater for the growth of AlGaN than measured for GaN. This increase in utilization efficiency is a result of the increased catalytic nature of Al on NH_3 [114, 115] as compared to Ga. As shown in Figure 4.1 and 4.2, the increased concentration of active N produced through this catalyzation requires higher total metal flow rates to reach a metal-rich growth regime, thereby increasing the range of growth conditions that result in N-rich growth. At 860 °C, the growth rates calculated for both AlGaN and GaN are lower

than those calculated for growth at 770 °C. The growth rate decrease seen for GaN and AlGaN (~100 nm/hr) is a result of increased GaN decomposition [101] and Ga/N desorption [101, 124], which occur above 800 °C. In MOCVD, desorption is typically prevented by the use of an NH_3 overpressure [124]. The low NH_3 flow rates (2 sccm) used in this experiment did not provide sufficient overpressure to prevent species desorption.

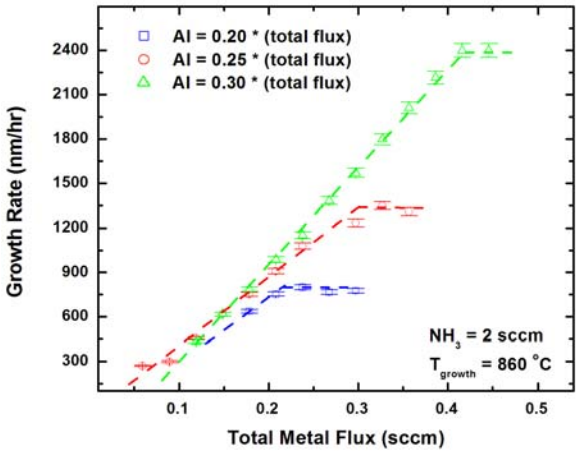

Figure 4.3: Growth rate of $Al_xGa_{1-x}N$ grown with varying Al gas phase compositions as a function of the total metal flow rate.

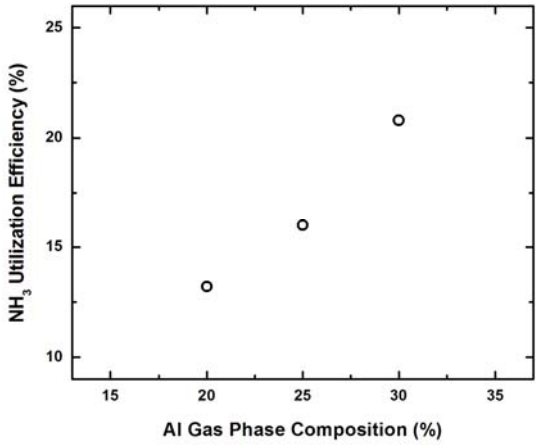

Figure 4.4: NH_3 utilization efficiency versus Al gas phase composition for $Al_xGa_{1-x}N$ grown at 860 °C.

The growth regimes for the growth of AlGaN were determined when the Al gas phase composition varied. The growth rates for AlGaN grown with varying Al gas phase compositions are shown in Figure 4.3. As done previously, the stoichiometric point was used to determine the NH_3 utilization efficiency for the growth of AlGaN. The NH_3 utilization efficiency is directly proportional to the TEAl flow rate within the studied regime, as shown in Figure 4.4. By making the Group-III flux more Al-rich, the catalyzation of NH_3 increases as well. Experimental limitations in the amount of Al flow able to be sourced prevented the investigation of the ammonia utilization saturation at higher Al compositions.

4.4 Morphology and Aluminum Composition Variations with AlGaN Growth Regime

XRD 2θ-ω of AlGaN (002) films grown in each growth regime at 770 °C are shown in Figure 4.5. The Al composition increases as the growth regime progresses from N-rich towards metal-rich. For N-rich growth, the Al composition is ~8.5 %, increasing to ~15.6 % for stoichiometric growth, and to ~29.5 % for metal-rich growth conditions. This increase in Al composition is seen even though the Al gas phase composition remains at 20 % of the total metal flow rate. This increase in solid Al composition is explained as preferential incorporation of Al over Ga that occurs when growth becomes N-limited [114, 125]. In this case, Ga will be incorporated only when the nitrogen requirements for the available Al have been met.

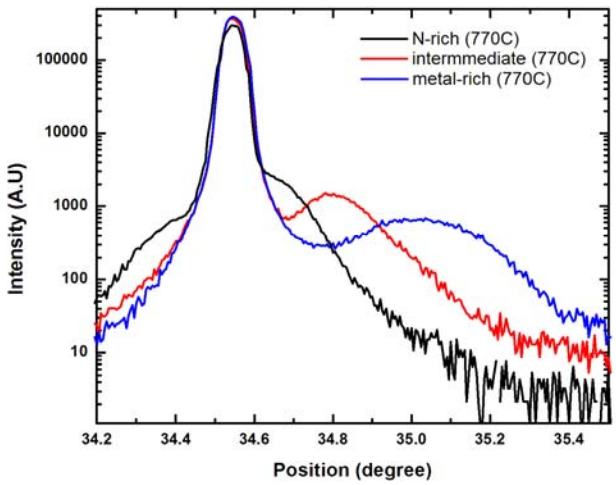

Figure 4.5: XRD 2θ-ω of $Al_xGa_{1-x}N$ (002) films grown at 770 °C with varying V/III ratios.

Figure 4.6 shows the resultant surface morphologies of AlGaN films grown under metal-rich, stoichiometric, and N-rich growth conditions, corresponding to V/III ratios of 6.7, 8.4, and 11.2 respectively. As the V/III ratio of the AlGaN films increases by only a factor of ~2, dramatic surface roughening on the order of ~100 times increase in the rms roughness occurs indicating a very sensitive relationship between V/III ratio and morphology. Growth of AlGaN in the metal-rich regime, the preferred growth mode for traditional MBE [126], results in granular surfaces with ~88 nm rms roughness. This morphology results from the decreased migration length of group III adatoms at decreased V/III ratios [101]. Near the stoichiometric point, surface pitting can be seen in the AlGaN films. These pits originate at threading dislocations (TDs) that form both at the interface of and propagate from the GaN template into the AlGaN bulk layer [121]. By increasing the V/III ratio, these surface pits are decreased and the surface roughness decreases further, which has been reported for the growth of AlGaN by MOCVD as well [127]. N-rich conditions result in an optimal rms roughness (~0.82 rms), consistent with previous GaN studies of NH_3-MOMBE [68].

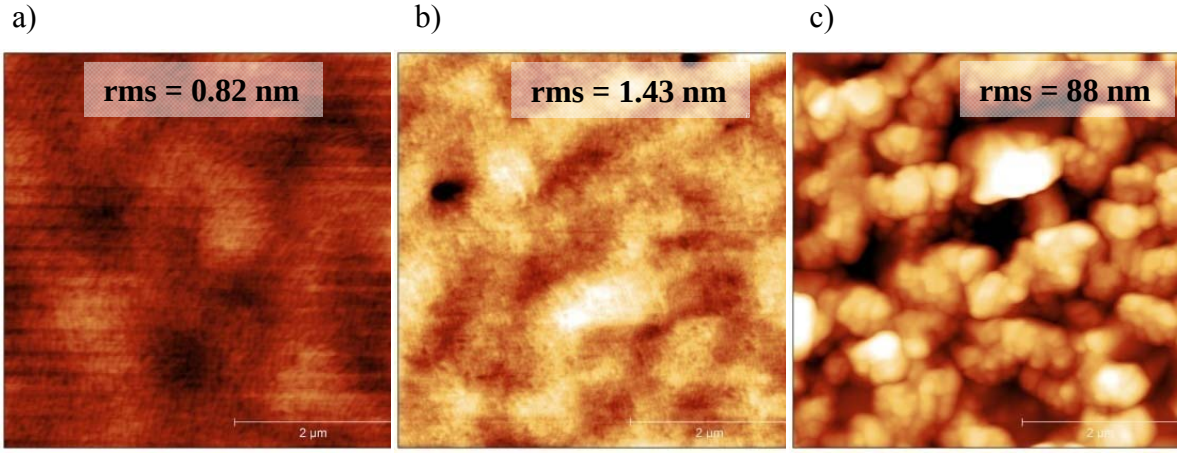

Figure 4.6: 5x5 µm AFM scans of $Al_xGa_{1-x}N$ films grown in a) N-rich b) near-stoichiometric and c) metal-rich growth regimes at 860 °C. Figure 4.6 (a) & (b) have z scales of 10 nm, with 4.6 (c) having a z scale of 400 nm.

4.5 Conclusions

An improved understanding of the growth of AlGaN was established by determining growth regimes and NH_3 utilization efficiency at varying growth temperatures. It was found that although growth occurs in the molecular flow regime (~4 x 10^{-6} Torr), the $Al_xGa_{1-x}N$ growth kinetics typically follow results seen in MOCVD literature, specifically, optimal surface morphologies occur under N-rich conditions as in MOCVD, not under Ga-rich conditions as in MBE. The NH_3 utilization efficiency for the growth of AlGaN was found to increase by a factor of ~2, as compared to GaN growth, due to the catalytic nature of Al on NH_3. Increasing the NH_3 utilization efficiency, the N-rich regime was extended, leading to larger ranges of growth conditions that yield smooth surface morphologies. The higher growth temperature (860 °C) used in

this study resulted in lower NH_3 utilization efficiencies, compared to 770 °C, because of decreased N surface coverage resulting from Ga/N desorption and/or GaN decomposition. The NH_3 utilization efficiency was found to vary with Al gas phase composition, with a higher percentage of Al in the gas phase leading to greater NH_3 catalyzation. When the Al gas phase composition was held constant, a preferential incorporation of Al over Ga was responsible for increased Al solid phase composition in films grown with lower V/III ratios. The growth regime also contributes to surface morphology variations, with the smoothest films associated with higher V/III ratios. Surface pitting, associated with TD density, was dependent on the V/III ratio of films grown with N-rich conditions. Growth in the metal-rich regime yields extremely rough films with granular growth morphologies, associated with decreased metal adatom mobility. Through this study, a better understanding of the influence of growth regime on the growth of AlGaN has been determined.

CHAPTER 5: HIGH-TEMPERATURE GROWTH OF GaN AND $Al_xGa_{1-x}N$ VIA AMMONIA-BASED METAL-ORGANIC MOLECULAR BEAM EPITAXY

5.1 Introduction

To realize NH_3-MOMBE grown GaN-based devices, high quality, planar films are necessary for proper device function. For transistor structures, interface roughness has been shown to affect the mobility of the 2DEG [86, 128]. In addition, higher quality films are necessary to achieve the bulk properties required for device applications [129]. The planarity of samples grown via the previously described growth conditions was found to be unsatisfactory. Thus, in an effort to achieve high quality, planar nitride films, an investigation of GaN and $Al_xGa_{1-x}N$ grown at higher growth temperatures (~950 °C) via NH_3-MOMBE was conducted. These high growth temperatures are typically difficult to achieve in the vacuum environment for large wafers and are rarely reported for traditional MBE due to the need for excessive nitrogen flow to prevent thermal etching. These conditions can be achieved in NH_3-MOMBE due to the strong temperature dependence of NH_3 pyrolysis but can only be achieved for smaller exploratory samples due to the power requirements of high temperature growth.

Despite the challenges associated with the more complex growth chemistry, NH_3-MOMBE has advantages over traditional MBE. In NH_3-MOMBE, the use of gaseous precursors increases the potential operational time compared to solid sources that need periodic openings of the vacuum system for reloading and subsequent baking. Higher

growth temperatures are beneficial for the growth of nitrides via NH_3-MOMBE because of the more efficient pyrolysis of NH_3 [115, 130], longer adatom diffusion lengths [101], and decreased carbon incorporation [32, 53, 131]. Although significant adatom desorption and GaN decomposition will occur at these elevated temperatures [32, 101, 124], mitigation of these effects can be achieved through an NH_3 overpressure [124].

In this chapter, the effects of growth temperature on the deposition of GaN and AlGaN by NH_3-MOMBE are reported. Ultimately, realization of high quality, planar nitride films grown via NH_3-MOMBE was achieved; exhibiting an optimal rms surface roughness of ~0.8 nm.

5.2 Experimental Procedure

GaN and AlGaN layers were grown in a custom NH_3-MOMBE showerhead reactor [54] on Lumilog silicon-doped GaN templates. The details regarding sample preparation are discussed in Appendix A.1. For this study, NH_3, TEGa, and TEAl were used as the precursors, which were introduced without carrier gases. Appendix A.2 explains the gas delivery system and discusses the conversion of source pressure to flow rate. Herein, all references to source precursors will be presented as flow rates, in sccm.

Growth of GaN and $Al_xGa_{1-x}N$ was conducted at 950 °C, with NH_3 flow rates of both 19 and 26 sccm. Growth rates were determined *in situ* using a custom laser interferometry system [68]. Crystalline quality of the films was determined using symmetric x-ray rocking curve measurements of the GaN (002) and AlGaN (002)

reflections. Vegard's Law, assuming fully relaxed films, was applied to XRD 2θ-ω scans of $Al_xGa_{1-x}N$ to determine aluminum compositions. Surface morphologies and surface roughness measurements were calculated by atomic force microscopy (AFM), using a Veeco Nanoscape III AFM.

5.3 High-Temperature Growth of GaN

The growth rates for GaN with NH_3 flow rates of 19 and 26 sccm are shown with increasing Ga flow rates in Figure 5.1. The ~37 % increase in NH_3 flow rate from 19 to 26 sccm results in ~10 % decrease in growth rate for all metal flow rates. This decrease in growth rate with increased NH_3 flow rate is consistent with other reports and is explained as increased NH_x site blocking in excessive NH_3 environments [101, 116]. Maximum GaN growth rates for this study were ~3.2 μm/hr, yet higher growth rates (> 4 μm/hr) are expected with a further increase in TEGa flow rates. The Ga flow rates used in this study resulted in N-rich growth, which has previously been shown to result in optimal GaN growth morphologies [68]. The crystalline quality of the GaN films, regardless of growth rate, mimicked that of the template with (002) XRD FWHMs of ~350 arcsecs.

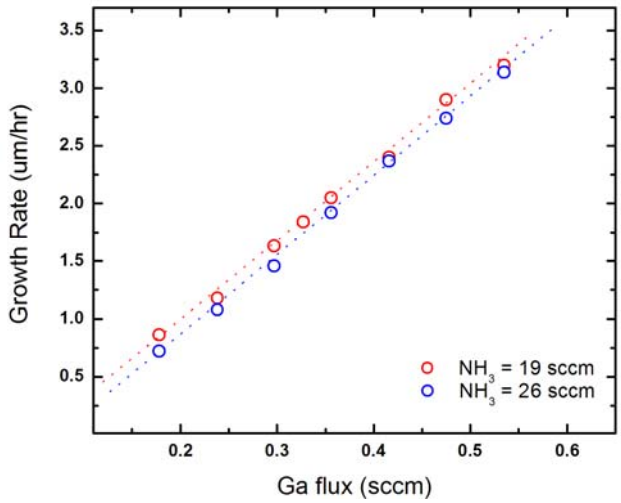

Figure 5.1: Growth rate of GaN grown with varying Ga flow rates for two NH_3 flow rates, 19 and 26 sccm.

Figure 5.2 shows GaN surface morphologies obtained by AFM with varying TEGa flow rates. For consistency, all GaN samples were grown to an equal thickness of 500 nm. For samples grown with TEGa flow rates less than 0.42 sccm, the films exhibit large steps of ~2 nm. The density of steps increases with increasing TEGa flow rates. In addition, spiral hillocks originating from screw dislocations were visible in films grown with TEGa flow rates below 0.42 sccm, as highlighted by the insets in Figure 5.2 (c) and (d). Increasing the TEGa flow rate above 0.42 sccm results in granular surface morphologies exhibiting increased rms roughness values. As seen in Figure 5.2, an optimal rms roughness of ~0.7 nm was achieved at 19 sccm NH_3 with a TEGa flow rate of 0.33 sccm, resulting in a V/III ratio of ~58. All references to V/III ratio refers to the supplied V/III ratio, and may be better understood as NH_3 flow rate versus total metal species (TEGa + TEAl) flow rate. When the NH_3 flow rate is increased to 26 sccm, excessive N-rich growth conditions are achieved and surface pits are formed, as seen in

Figure 5.3. These pits have been recorded previously in excessive NH_3 environments as a result of decreased adatom surface diffusion on a N-saturated surface [101, 117]. The pit formation can be eliminated by decreasing the V/III ratio, which results in surface morphologies similar to the lower NH_3 case.

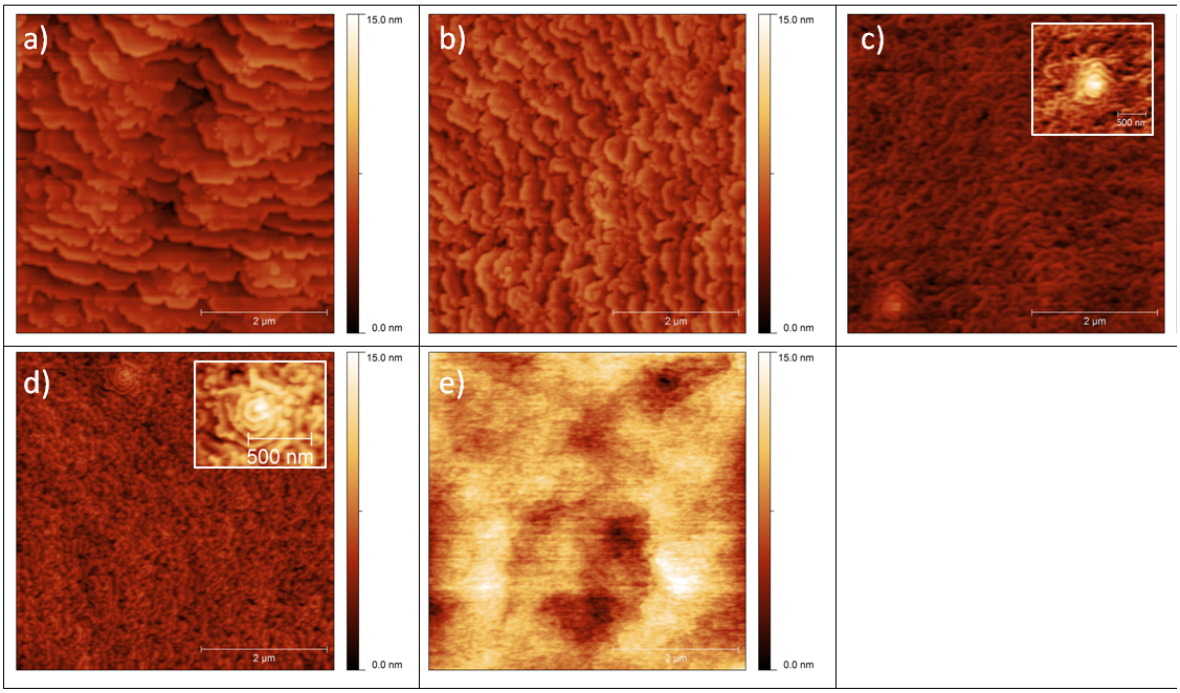

Figure 5.2: 5x5 μm AFM scans of 500 nm thick GaN films grown at 950 °C with an NH_3 flow rate of 19 sccm and TEGa flow rates of (a) 0.24 sccm, (b) 0.3 sccm, (c) 0.33 sccm, (d) 0.35 sccm, and (e) 0.42 sccm. The z height scale for all scans is 15 nm. The rms roughness was calculated as (a) 1 nm, (b) 1 nm, (c) 0.7 nm, (d) 0.85 nm, and (e) 2 nm. Insets in figures (c) & (d) highlight the spiral hillocks addressed in the text.

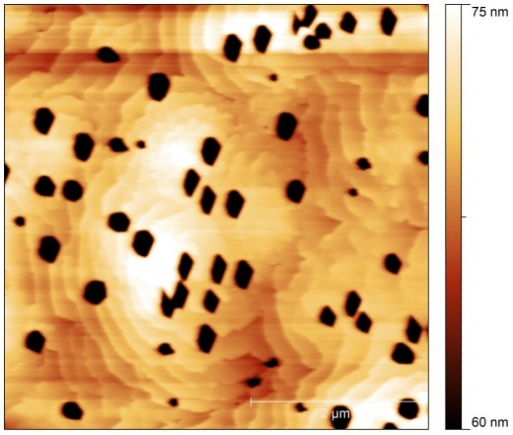

Figure 5.3: Representative AFM scan showing surface pitting in GaN films grown with excessive NH_3 flow. The AFM image has a z scale of 15 nm.

5.4 High-Temperature Growth of $Al_xGa_{1-x}N$

Figure 5.4 shows the growth rate variation between GaN and AlGaN with increasing total metal (TEGa + TEAl) flow rates, with the Al gas phase composition maintained at 20 % of the total metal flow rate. Error bars have been included for the $Al_xGa_{1-x}N$ growth rates to account for the change in refractive index with the aluminum content. The AlGaN growth rate is consistently lower than that of the GaN, with as much as a ~35 % difference. The difference between the AlGaN and GaN growth rates decreases with increasing metal content, with a minimum percent difference of ~16 %. The lower growth rate for the AlGaN is assumed to be related to a more N-rich growth,

which has previously been shown to reduce growth rate in NH_3-MOMBE [68]. The more efficient pyrolysis of NH_3 in the presence of Al results in more active N, which slows the growth rate due to an increased recombination of active N [101, 124]. With increasing total metal flow rate, more of the available N can be consumed; therefore the difference in growth rates between AlGaN and GaN decreases with increasing metal flow rate.

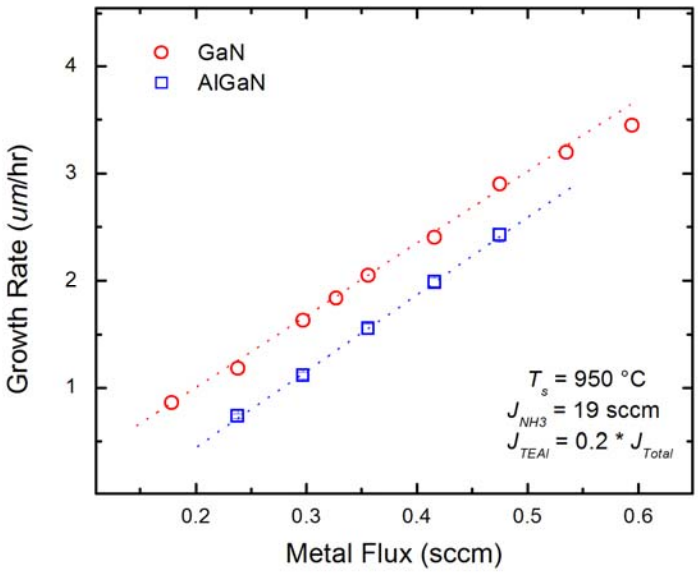

Figure 5.4: Growth rate of GaN and AlGaN grown with metal flow rates varying from 0.15 to 0.6 sccm, with a constant NH_3 flow rate of 19 sccm.

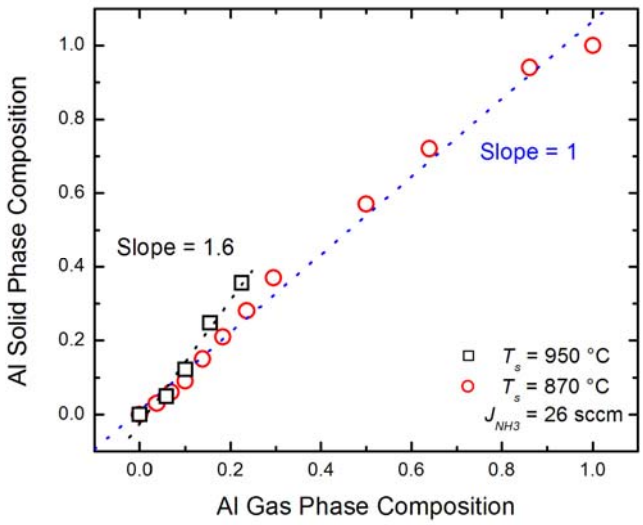

Figure 5.5: Al solid phase composition with increasing Al gas phase composition for AlGaN grown at 870 & 950 °C. The total metal flow rate was maintained at 0.33 sccm.

To investigate the Al composition and surface morphology, $Al_xGa_{1-x}N$ samples with varying total metal flow rates were grown to a thickness of ~200 nm. For all growths, the total metal flow rate was held constant at 0.33 sccm and the TEGa/TEAl ratio was varied. The Al composition with varying metal flow rates at temperatures of 870 and 950 °C is shown in Figure 5.5. Compared with previously published AlGaN growths [120], the Al composition for the same metal flow rate is higher when grown at higher temperatures. The slope of the curve is ~1.6 for 950 °C, as compared to the previously measured slope of ~1 for the AlGaN films grown at 870 °C. The increase in the Al incorporation at the increased growth temperature is a result of the increased Ga desorption flux. The increase in Ga desorption flux between 870 and 950 °C has been calculated as an order of magnitude [101].

AFM (5x5 μm) scans of $Al_xGa_{1-x}N$ with varying Al compositions are shown in Figure 5.6. These films exhibit surface pitting due to the enhanced pyrolysis of NH_3 in the presence of Al as compared to Ga, resulting in a more N-rich growth environment. Adatom mobility decreases in excessive N-rich growth environments, resulting in the formation of faceted surface pits [117, 121]. The pit density decreases with increasing Al content as the excess N is more efficiently consumed by the higher metal flow rate. Figure 5.6 (a) and (b) show large, ~2 nm steps similar to those seen in the GaN films, resulting in an rms roughness of 1.5 and 1 nm, respectively. Figure 5.6 (c) shows $Al_{0.25}Ga_{0.75}N$, which exhibits hillocks with atomic steps and an rms roughness of ~0.8 nm. Although not visible in the AFM scans, growth of $Al_{0.25}Ga_{0.75}N$ resulted in surface cracking as a result of the tensile strain [110, 111]. In addition, Pendellösung fringes are visible in $Al_xGa_{1-x}N$ films with lower Al compositions, as seen in Figure 5.7 showing the XRD 2θ-ω scans of $Al_xGa_{1-x}N$ (002). The x-ray Pendellösung fringes indicate a planar surface morphology and an abrupt interface between the AlGaN layer and the GaN template.

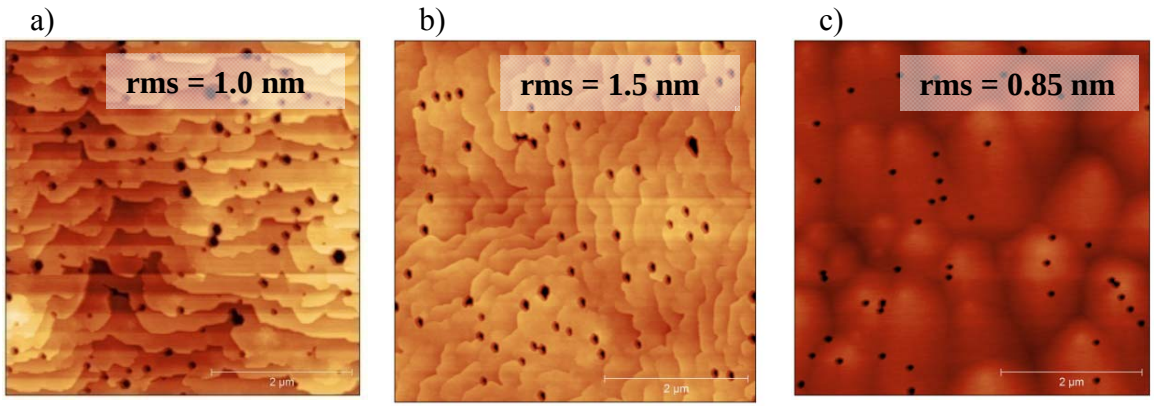

Figure 5.6: 5x5 µm AFM scans of a) $Al_{0.05}Ga0_{.95}N$ b) $Al_{0.12}Ga_{0.88}N$ c) $Al_{0.25}Ga_{0.75}N$ films illustrating morphological variations with varying Al compositions. For all scans, the z scale is 15 nm.

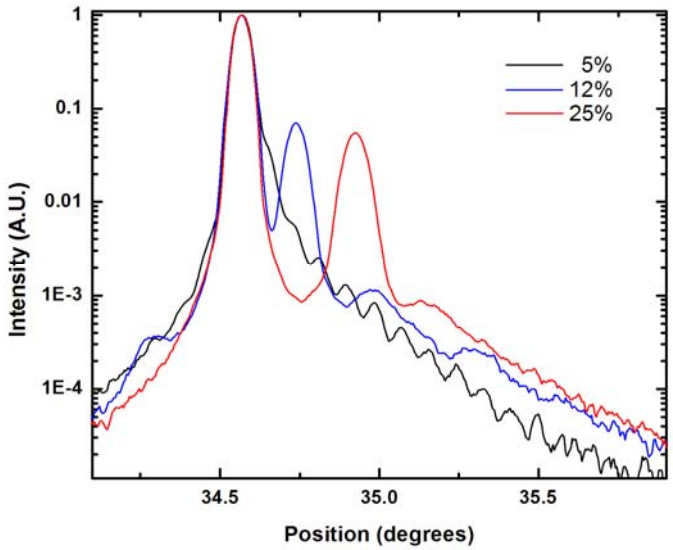

Figure 5.7: XRD 2θ-ω scans of AlGaN with varying Al compositions showing an AlGaN/GaN interface that exhibits Pendellösung fringes.

5.5 Conclusions

The improvement of surface morphology and understanding in the growth kinetics of GaN and AlGaN grown at high substrate temperatures by NH_3-MOMBE has been investigated. The influence of V/III ratio and gas phase composition on the growth of GaN and AlGaN was identified for a growth temperature of 950 °C. The crystalline quality of GaN and AlGaN was found to mimic the crystalline quality of the GaN template with (002) XRD FWHMs of ~350 arcsecs. The growth rate of III-nitrides by NH_3-MOMBE was found to be reduced under excessive N. This issue is further exaggerated for the growth of AlGaN, due to the increased catalytic nature of Al over Ga. The surface morphology is also affected by the excessive N, resulting in the formation of faceted surface pits at higher V/III ratios, due to the formation and propagation of threading dislocations from the interface. Optimized growth conditions for both GaN and AlGaN lead to an rms roughness of ~0.7 nm and ~0.85 nm, respectively. Higher growth temperature was found to increase the Al composition for a given Al gas phase composition due to higher Ga desorption at increased growth temperatures. AlGaN films grown directly on GaN templates exhibited Pendellösung fringes when measured by XRD, indicating planar growth and abrupt interface transitions. The smooth surface morphologies, combined with the presence of Pendellösung fringes for AlGaN films, indicate that these morphologies should be suitable for application in transistor devices.

CHAPTER 6: EFFECT OF GROWTH CONDITIONS ON CARBON INCORPORATION IN GaN GROWN BY AMMONIA-BASED METAL-ORGANIC MOLECULAR BEAM EPITAXY

6.1 Introduction

NH_3-MOMBE has shown its potential in C-doping to provide highly resistive GaN films, with a resistivity in excess of 10^{12} Ω-cm [132]. The growth of GaN and AlGaN at high temperature has also improved the planarity and crystal quality of the III-Nitride films, as described in the previous chapter. With these successes, the highly resistive GaN films can now be considered for low leakage buffers in GaN-based HEMTs, to further improve device performance [62, 64, 65, 69]. While C-doped GaN films have shown significant promise [64, 65, 132], the high [C] desired for device isolation can also result in trap states that will adversely affect device performance by affecting the 2DEG [65, 132-135]. Several groups have adopted GaN layers near the AlGaN/GaN interface with lower [C] to prevent these adverse affects [136, 137]. To utilize the highly resistive C-doped GaN films produced by NH_3-MOMBE, a means of reducing C near the AlGaN/GaN interface may be necessary to realize operational HEMTs.

In this chapter we explore the effect of NH_3-MOMBE growth conditions, such as growth temperature and V/III ratio, on the GaN surface morphology and ultimate C incorporation. Step bunching in GaN surface morphologies is suspected to result from the production of additional H at higher growth temperatures and higher NH_3 flow rates,

with H's preferential affinity for certain crystalline faces affecting growth kinetics. Additional, increases in both growth temperature and V/III ratios are reported to reduce the amount of C incorporated for the growth of GaN by NH_3-MOMBE.

6.2 Experimental Procedure

All films grown for this chapter were deposited in a custom NH_3-MOMBE growth reactor [54], with a base pressure of ~5 x 10^{-9} Torr. Appendix A.1 explains the steps performed to prepare the substrates for growth. NH_3 and TEGa were used as the precursors, which were introduced without carrier gases. The gas delivery system and precursor conversion equations are discussed in Appendix A.2. Herein, all references to source precursors will be presented as flow rates.

To investigate the influence of growth conditions on carbon incorporation, the growth temperature for GaN was varied between 770, 860 and 950 °C, with NH_3 flow rates of both 19 and 50 sccm. GaN growth rates were calculated *in situ* using a custom laser interferometry system [68]. Surface morphologies and surface roughness measurements were calculated by AFM, using a Veeco Nanoscape III AFM. To determine carbon levels in the films, samples were externally characterized by SIMS, at Evans Analytical Group, utilizing a positive Cesium beam (Cs+).

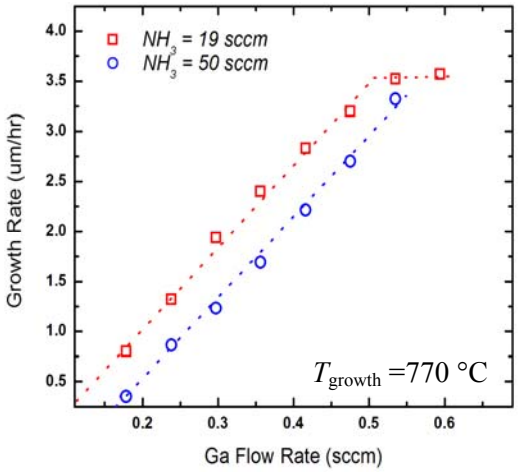

Figure 6.1: Growth rate versus TEGa flow rate at 770 °C with NH_3 flow rates of 19 and 50 sccm.

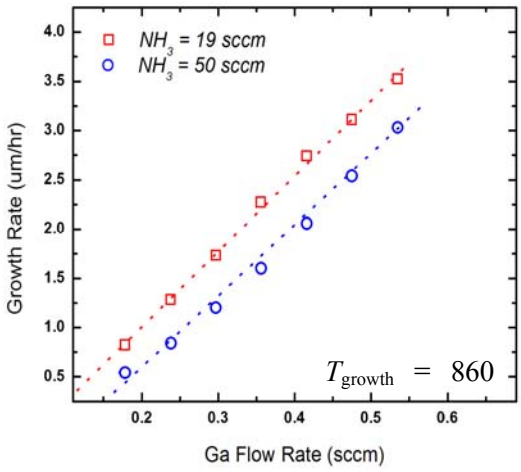

Figure 6.2: Growth rate versus TEGa flow rate at 860 °C with NH_3 flow rates of 19 and 50 sccm.

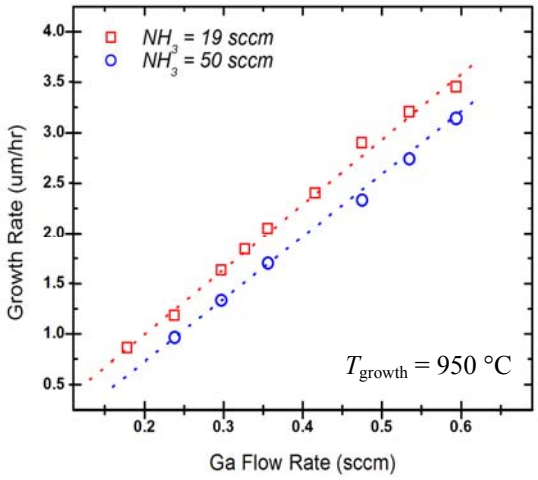

Figure 6.3: Growth rate versus TEGa flow rate at 950 °C with NH_3 flow rates of 19 and 50 sccm.

6.3 Optimization of Surface Morphologies

Planar GaN surface morphologies are imperative for this work, since these films are ultimately purposed for use in transistor devices. While examining the effect of growth conditions on carbon concentrations, emphasis on maintaining smooth surfaces was also maintained. Therefore, experimentation began with determining the optimal growth conditions at each growth temperature and NH_3 flow rate combination. To determine ideal GaN growth conditions, the growth rates at each varying temperature/NH_3 combination were measured and are plotted in Figures 6.1, 6.2 and 6.3. As seen in the figures, the increase in NH_3 from 19 to 50 sccm decreases the growth rate of GaN by ~30 %, independent of growth temperature. This decrease in growth rate with

increasing NH_3 flow rate is assumed to be a result of NH_x site blocking, preventing Ga species from effectively adsorbing onto the growth surface [101, 116]. This reduction in site blocking allows for increased surface Ga accumulation [124], which increases GaN formation and NH_3 catalyzation [115, 138]. The growth rate curves also indicate that there is a decrease in GaN growth rate with increasing growth temperature. This decrease in growth rate between growth temperatures is enhanced as the TEGa flow rate is increased. The maximum growth rate difference (~17.5 %) occurs for GaN films grown 950 and 770 °C, with 0.53 sccm TEGa and 50 sccm NH_3. This decrease in growth rate at increased temperatures is a result of increased species desorption [101, 124] and GaN decomposition [101] at increased growth temperatures. The effects of GaN growth parameters on the GaN growth rate for NH_3-MOMBE are summarized in Table 6.1. The figures also indicate that the only condition in which Ga-rich growth was achieved occurred in the films grown at the lowest temperatures (770°C) with the lowest NH_3 flow rates (19 sccm). Not achieving Ga-rich growth is beneficial because, as stated in previous chapters, the optimal growth conditions for GaN films grown by NH_3-MOMBE occur in the N-rich growth regime. After calculating growth rates and growth regimes for GaN, several GaN films were grown at each condition and then characterized via AFM to determine the optimal surface morphology.

Table 6.1: Quantification of the influence of NH_3-MOMBE GaN growth parameters on the growth rate, carbon incorporation and surface roughness.

Parameter	Range	Surface Roughness	Growth rate	Carbon Content
NH_3 Flow Rate	15 to 50 sccm	↓ by 2x	↓ by 1.25x	↓ by 5x
Growth Temperature	770 – 950 °C	↑ by 4x	constant	↓ by 4x
TEG Flow Rate	0.24 – 0.6 sccm	↑ by 4.5x	↑ by 3.7x	↑ by 4x

After determining the growth rates, ~300 nm thick GaN films were grown with NH_3 flow rates of 19 and 50 sccm and growth temperatures of 770, 860 and 950 °C. The TEGa flow rate was varied to determine the optimal surface morphologies. Figure 6.4 shows the optimized GaN surface morphologies at each temperature and NH_3 flow rate. In each GaN sample, the surface rms roughness was below ~2 nm. Although each film exhibited smooth surface morphologies, there are several differences noticeable between the samples. In all instances, the GaN films grown with NH_3 flow rates of 19 sccm exhibited macroscopic steps of ~2 nm in height. These step heights are multiple times greater than the GaN unit cell height of ~5 Å. These increased steps sizes are suspected to results from step bunching that occurs in the presence of H [139]. The H is formed at increased growth temperatures as NH_3 is catalyzed. Feenstra *et al.* have seen similar morphologies when using hydrogen for MBE growth of GaN [139], in which they postulate that the H allows for more efficient capture of growth species along certain growth planes, resulting in step bunching or faceting. These assumptions have also been concluded through theoretical simulations for MOVPE growth of GaN [140]. When the NH_3 flow is increased to 50 sccm, the GaN morphologies improve, with atomic steps

becoming clearly visible when grown at 770 °C, as a result of step-flow growth. Increasing the temperature above 770 °C results in step bunching since the increased growth temperature provides more atomic H from the dissociation of NH_3. It should be noted that at temperatures of 860 and 950 °C, with NH_3 flow rates of 50 sccm, smaller step heights corresponding to the GaN unit cell are also visible among the large steps. With the GaN surface morphologies optimized, the influence of growth conditions on the amount of carbon incorporated into the film was explored.

\

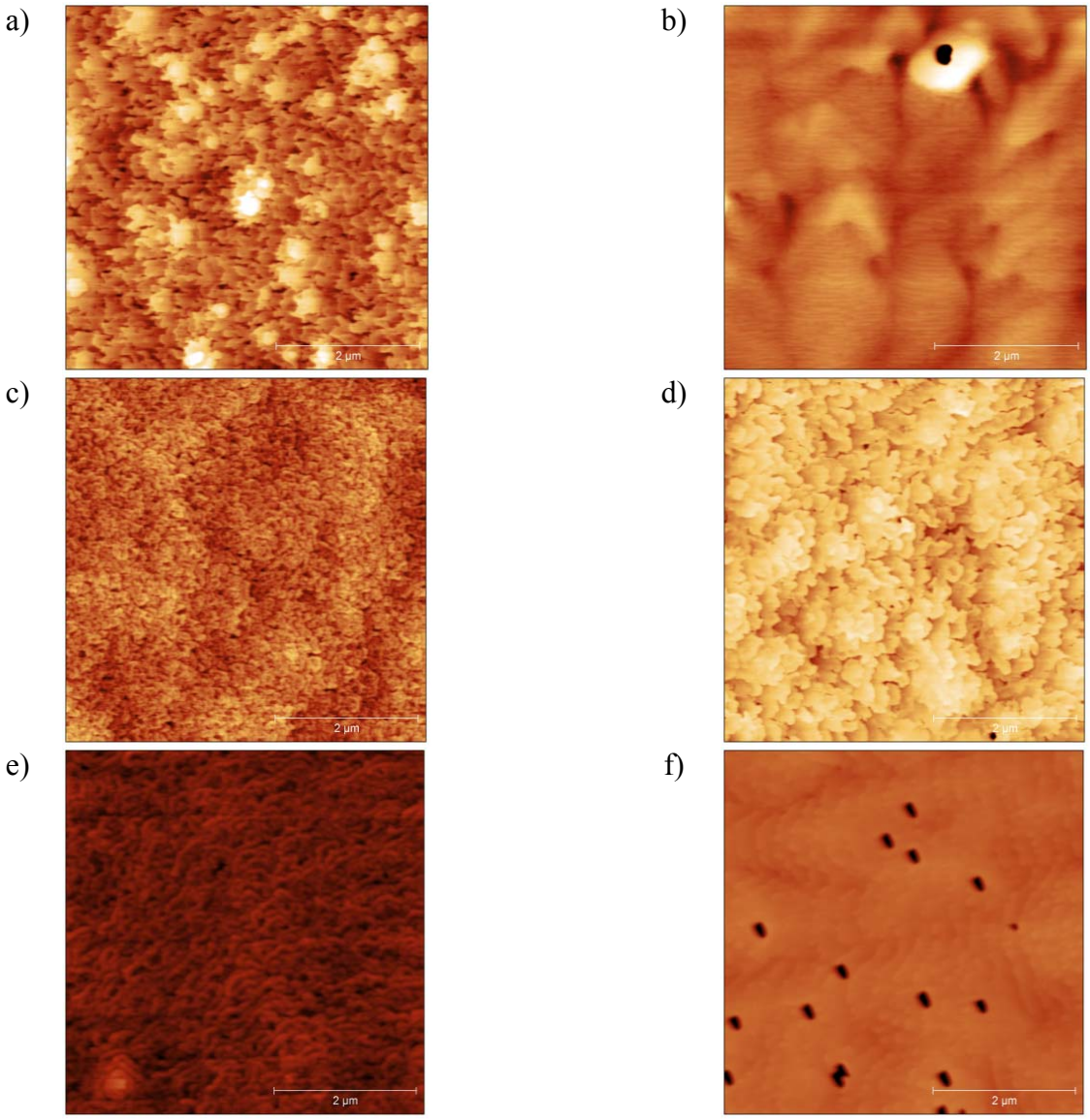

Figure 6.4: AFM images of 5x5 μm surface morphologies of 300 nm thick GaN films grown with varying growth conditions. Figures a), c) and e) were grown with NH_3 = 19 sccm, figures b), d), and f) were grown with NH_3 = 50 sccm. Figures a) and b) were grown at 770 °C, c) and d) were grown at 860 °C and e) and f) were grown at 950 °C. The supplied V/III ratios are a) 80, b) 168, c) 53, d) 120, e) 58 and f) 140. The rms roughness values are a) 1.3 nm, b) 1 nm, c) 0.9 nm, d) 0.7 nm, e) 1.7 nm and f) 2.1 nm. All images have z scales of 10 nm, except for f) which has z scale of 50 nm.

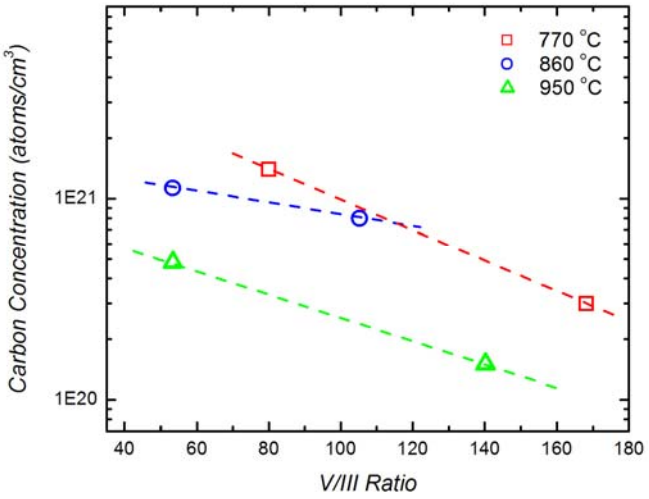

Figure 6.5: Average carbon concentrations in GaN films grown with varying V/III ratios at substrate temperatures of 770, 860 and 950 °C. C concentrations determined through SIMS.

6.4 Effect of Growth Conditions on Carbon Incorporation

To quantify the carbon levels, GaN films were deposited and measured using SIMS at Evans Analytical Group, with the results plotted in Figure 6.5. Increasing the supplied V/III ratio for the deposition of GaN decreases the [C], independent of growth temperature. The increased V/III ratio during growth provides more NH_3, which is subsequently catalyzed on the surface, providing H that liberates adsorbed ethyl groups from the growing surface. These ethyl groups are responsible for the incorporation of C because of the C-H bond that forms on the growth surface. By providing more H, adsorbed ethyls are removed from the surface, resulting in lower [C]. This trend of

decreased [C] with increasing V/III ratio agrees with other published results for GaN [131] and GaAs [49] grown with metal-organics. In addition, increasing the GaN growth temperature also results in lower [C]. Higher growth temperatures increase the NH_3 catalyzation efficiency, providing additional H for ethyl removal [130, 141]. Whether the growth temperature or the V/III ratio is increased, the mechanism responsible for decreased [C] is the same. Less carbon is incorporated because of an increased liberation of adsorbed ethyls resulting from increased available H. Quantitative values of the effect of growth parameters on the C levels in GaN for NH_3-MOMBE are shown in Table 6.1.

6.5 Conclusions

The optimization of GaN growth parameters for the realization of planar films, as well as the effect of the growth parameters on carbon incorporation in GaN by NH_3-MOMBE has been investigated. The variation in GaN growth rate and growth mode with varying growth parameters was determined for growth temperatures of 770, 860 and 950 °C. The growth rate of GaN was found to be influenced by NH_3 flow rate, TEGa flow rate and growth temperature. Optimized surface morphologies for GaN were discovered at NH_3 flow rates of 19 and 50 sccm with growth temperatures of 770, 860 and 950 °C. The increased H available at increased temperatures and decreased NH_3 flow rates leads to step bunching and surface faceting due to H's preferential affinity for certain growth surfaces and attraction to growth species. Atomic steps were visible in GaN films grown with sufficient NH_3 flow rates. The incorporation of C in GaN is dependent on both

growth temperature and V/III ratio. Increased growth temperatures and V/III ratios provide increased available H, allowing for increased liberation of adsorbed ethyls that are responsible for C. Increasing GaN growth temperature results in C decreases of 250 %, while increasing the V/III ratio resulted in C decreases of ~475 %. Through this study, a detailed understanding of the effect of GaN growth parameters on the growth rate, surface morphology, and C incorporation has been developed. Control and ultimate reduction of C incorporation is a promising step in the realization of transistors grown by NH_3-MOMBE.

CHAPTER 7: EFFECT OF ATOMIC HYDROGEN ON THE LIBERATION OF ADSORBED ETHYLS FROM GaN GROWN BY AMMONIA-BASED METAL-ORGANIC MOLECULAR BEAM EPITAXY

7.1 Introduction

While results from the previous chapter showed modest reductions in carbon incorporation in GaN, further progress is necessary to realize devices grown by NH_3-MOMBE. Control of the doping near the 2DEG is needed to prevent negative effects from the dopants [136]. While NH_3-MOMBE has been utilized to produce GaN films with a resistivity exceeding 10^{12} Ω-cm, the carbon levels ($>10^{21}$ cm^{-3}) [54] have presented significant challenges in forming a 2DEG. Since the carbon incorporation in III-Nitrides grown by NH_3-MOMBE is a result of incomplete reactant pyrolysis, and not a result of intentional doping, methods to control the incorporation of adsorbed ethyl groups are necessary to reduce the carbon levels. Atomic hydrogen has been studied as a possible means of increasing ethyl desorption, thereby decreasing carbon incorporation [142, 143] and has been shown to influence the growth kinetics of GaN [139, 140]. In addition to growth parameter optimization as described in Chapter 6, the use of thermally pyrolyzed hydrogen is explored in this chapter as a means of carbon incorporation reduction. In addition, the effect of hydrogen addition on the morphology and growth rate of GaN is explored.

7.2 Design of Thermal Hydrogen Cracker

To provide atomic hydrogen to the growth surface, a custom thermal hydrogen cracker was developed, as seen in Figure 7.1. Although commercial hydrogen crackers are available [144-146], cost and system restrictions necessitated the design of a custom component. For the custom cracker, a stainless steel tee with a 1.5" inner diameter and 2.75" conflat flanges was used for the system housing. The housing was connected to the growth chamber through reducer flanges, converting the 2.75" conflat flanges to 0.25" stainless tubing, allowing for integration onto the system showerhead through VCR fittings. The traditional copper gaskets used for the reducer flanges were substituted with niobium (Nb) gaskets, which were chosen since Nb is malleable enough to ensure vacuum integrity, yet able to withstand the increased temperatures produced by the filament. These gaskets were specifically milled to specifications, with a thickness of 2 mm, an outer diameter of 21.25 mm, and an inner diameter of 4.6 mm. An additional purpose of these Nb gaskets was to confine a Ta rod across the longitudinal axis of the cracker assembly. The Ta rod had a 1 mm diameter hole drilled through the center to confine the flow of molecular hydrogen. By confining the flow of hydrogen, it was presumed that the cracking efficiency of the hydrogen would be increased. Unfortunately, proper isolation of the W filament and the Ta rod could not be achieved without impeding radiation heating. The filament used was provided by Midwest Tungsten and consisted of triple-braided, 0.55 mm Tungsten (W) wire in an open helix filament design. The filament measured 16 mm wide and 35 mm high, with an inner diameter of 6.5 mm. The filament was heated by a Xantrex XFR 35-35 power supply,

which supplies a maximum power of 1225 W (35V, 35A). The flow of hydrogen through the cracker was controlled by a Celerity 20 sccm mass flow controller, which was automated through custom LabVIEW software.

Similar thermal hydrogen cracker systems have been designed in the past, yet efficiencies of these systems vary greatly. Several reports have suggested that filament temperatures in excess of 1500 °C result in cracking efficiencies greater than 80 % [147, 148], while others have reported cracking efficiencies as low as 1.5 % at similar filament temperatures [149].

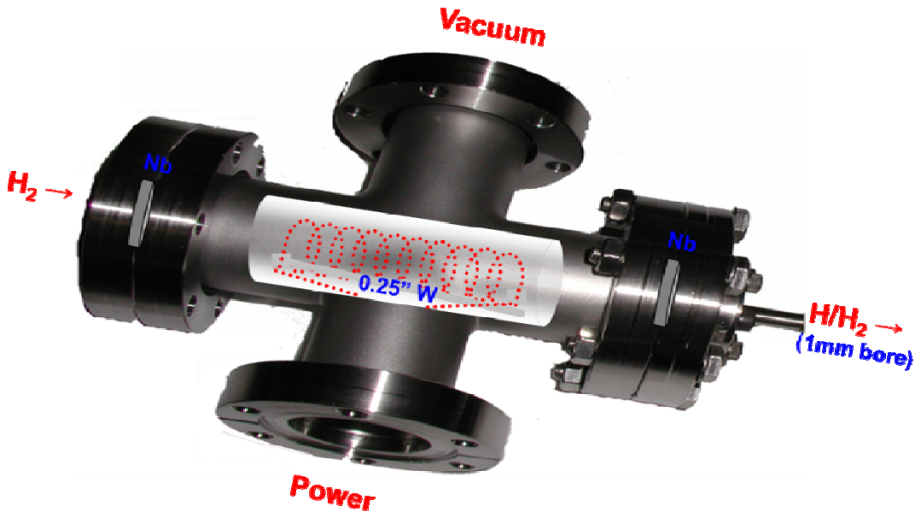

Figure 7.1: Illustration of the custom hydrogen cracker installed on NH_3-MOMBE system to provide atomic hydrogen.

7.3 Experimental Procedure

All films grown for this chapter were deposited in a custom NH_3-MOMBE growth reactor [54], with a base pressure of ~5 x 10^{-9} Torr. The details of the substrate cleaning and preparation are discussed in Appendix A.1. NH_3 and TEGa were used as the precursors, which were introduced without carrier gases. H_2 was introduced during the growth of GaN, with the flow controlled by a MFC before flowing through the thermal hydrogen cracker. The gas delivery system used for the remaining precursors and the conversion of the source pressures to flow rates is detailed in Appendix A.2. Herein, all references to source precursors will be presented as flow rates.

To investigate the influence of atomic hydrogen on carbon incorporation, GaN films grown at 950 °C with an NH_3 flow rate of 50 sccm and a TEGa flow rate of 0.45 sccm. The sample was also exposed to 15 sccm of H_2 for the second half of the growth. The H_2 was introduced through a thermal hydrogen cracker with a W filament powered to ~250 W (30 V, 8.4 A). The approximate filament temperature can be determined with Equation 7.1.

$$T^4 = \frac{P}{\epsilon \sigma A} \tag{7.1}$$

In Equation 7.1, P is the filament power in Watts, ε is the emissivity of tungsten (0.28 @ 2000 °C), σ is the Stefan-Boltzmann constant (5.7 x 10^{-8} $Wm^{-2}K^{-4}$), A is surface area of the filament (~7.8 x 10^{-4} m^2), and T is temperature in °K. Assuming all power across the

filament is lost as radiative heat, the approximate filament temperature is estimated as 1850 °C.

GaN growth rates were measured *in situ* using a custom laser interferometry system [68]. Surface morphologies and surface roughness measurements were measured by AFM, using a Veeco Nanoscape III AFM. To determine carbon levels in the films, samples were externally characterized by SIMS at Evans Analytical Group, utilizing a positive Cesium beam (Cs+).

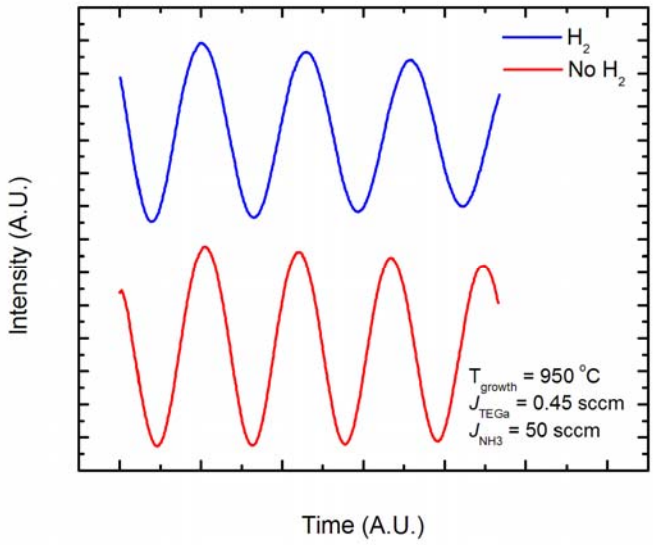

Figure 7.2: Laser interferometry signals for the growth of GaN at 950 °C, with and without H_2 present during growth showing reduced growth rate when H_2 was used.

7.4 Effect of Atomic Hydrogen on the Growth of GaN

Although carbon reduction is the ultimate goal of atomic hydrogen addition, hydrogen may also have adverse consequences, therefore the growth rate and morphology of the grown GaN films was monitored to ensure the films remain suitable for device applications. Figure 7.2 illustrates the variation in growth rate, as detected by the laser interferometry system, for GaN when H_2 is introduced. The growth rate variations calculated from the interferometry signals result in a 15 % decrease in growth rate when H_2 is introduced during growth. This decrease in growth rate is a result of recombination of the pyrolyzed reactants on the growth surface, effectively reducing the available growth species on the growth surface [140]. In addition, the introduction of molecular hydrogen has been determined to result in a reversible decomposition of GaN.

$$GaN(s) + (ads) + 1.5H_2 \leftrightarrow Ga(ads) + NH_3 \quad (7.1)$$

$$Ga(ads) \leftrightarrow Ga(g) + (ads) \quad (7.2)$$

In the above equations (ads) represents an available surface adsorption site and Ga(ads) represents an adsorbed Ga adatom [140, 150]. This possible decomposition could also be the source of the reduced growth rate seen when hydrogen is introduced during the growth of GaN.

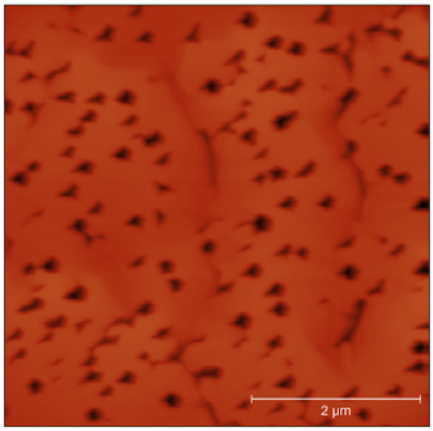

Figure 7.3: Resulting surface morphology (5x5 μm) of GaN grown without atomic hydrogen. GaN film grown at 950 °C with TEGa flow rate of 0.36 sccm and NH_3 flow rate of 50 sccm. The AFM scan is scaled at 20 nm exhibiting a rms roughness of 10 nm.

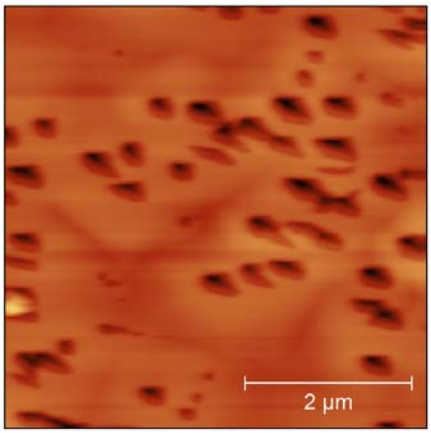

Figure 7.4: Resulting surface morphology (5x5 μm) of GaN grown with atomic hydrogen. GaN film grown at 950 °C with TEGa flow rate of 0.36 sccm and NH_3 flow rate of 50 sccm. The AFM scan is scaled at 20 nm exhibiting a rms roughness of 13 nm.

The effect of atomic hydrogen on the morphology of the resulting GaN films is shown in Figures 7.3 and 7.4. Morphologies exhibit pitted surfaces arising from slight N-rich growth conditions as discussed in previous chapters. These surface pits arise from threading dislocations, which are located below the surface of the film [117, 121]. When atomic hydrogen is introduced during growth, the density of pits is reduced, although the size of the pits increases resulting in a ~30 % increased rms roughness. GaN films grown without hydrogen exposure exhibited surface pitting with average pit areas of ~0.02 μm^2, while hydrogen exposure increases the average pit area to ~0.1 μm^2. These variations in surface morphologies are a result of variations in the growth kinetics of GaN with the introduction of atomic hydrogen and may be related to the previously mentioned tendency of hydrogen to adsorb on preferred crystalline planes. Feenstra *et al.* reported that atomic hydrogen effects the adsorbed growth species, effectively increasing active N species for growth [139]. This increase in active N on the growth surface leads to large surface pits, as higher surface N adatoms has been shown to decrease the overall adatom diffusion lengths [101, 117].

After determining the effect of hydrogen on the growth rate and surface morphologies, as well as achieving suitable surface morphologies, all requiring a complete re-calibration of growth conditions arrived at from years of effort described in previous chapters, a GaN stack structure was deposited for SIMS analysis. Each layer was ~600 nm thick, with one layer exposed to hydrogen and the other without. The addition of atomic hydrogen to the growth of GaN has been reported in literature to lower carbon concentrations through the elimination of adsorbed ethyl groups through two possible reaction pathways, desorbing as either ethane (C_2H_6) or ethylene (C_2H_4).

$$C_2H_5 + H \rightarrow C_2H_6 \quad (7.3)$$

$$C_2H_5 + H \rightarrow C_2H_4 + H_2 \quad (7.4)$$

The spontaneous nature of both reactions is exhibited by their change in the Gibbs free energy, ΔG, at 900 °C, which are -238 kilojoules (kJ) for Reaction 7.3 and -250 kJ for Reaction 7.4.

Figure 7.5 shows the results from the SIMS analysis. The GaN film grown without atomic hydrogen exhibited a carbon concentration of ~5 x 10^{20} cm^{-3}, while the addition of atomic hydrogen resulted in a concentration of ~4 x 10^{20} cm^{-3}, a decrease of 20 %. The nominal decrease in carbon concentration is lower than expected and may result from significant recombination of the atomic hydrogen before reaching the growth surface. The gas phase reaction

$$2H(g) \rightarrow H_2(g) \quad (7.5)$$

exhibits a Gibbs free energy (ΔG) of -300 kJ at a temperature of 1000 °C and decreases to -400 kJ at room temperature, indicating it is highly favorable at all temperatures [151]. Although the high growth pressure during hydrogen introduction does not allow for RGA analysis, the order of magnitude increase in the growth pressure with the introduction of hydrogen indicates it comprises a significant portion of the growth pressure. This large partial pressure of hydrogen, combined with the favorability of Equation 7.5 illustrates the probability of hydrogen recombination. Additionally, the relatively large distance

from cracker to growth surface (~6 in.) combined with the high flow rate of H_2 (15 sccm) results in a high probability of recombination. Also the reduced effectiveness of atomic hydrogen may be a result of increased NH_3 pyrolysis at increased growth temperatures. The increased pyrolysis of NH_3 may provide sufficient hydrogen on the surface, reducing the effectiveness of the intentional introduction of atomic hydrogen. Either explanation may be responsible for the relatively small decrease in carbon concentration in GaN.

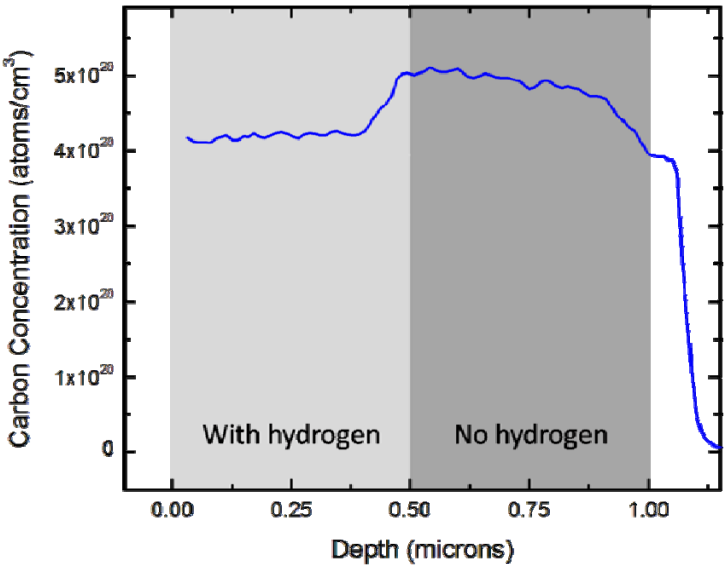

Figure 7.5: SIMS depth profile showing the variation in carbon concentration for GaN films when grown with and without atomic hydrogen. The GaN layers were grown at 950 °C, with TEGa flow rate of 0.36 sccm and NH_3 flow rate of 50 sccm. The H_2 flow rate was ~15 sccm.

7.5 Conclusions

The introduction of atomic hydrogen as a means for adsorbed ethyl liberation during the growth of GaN by NH_3-based MOMBE has been investigated. To produce atomic hydrogen, a custom thermal hydrogen cracker was designed in which a tungsten filament was heated to ~1800 °C under vacuum to provide pyrolysis of molecular hydrogen. The growth rate of GaN was influenced by the introduction of atomic hydrogen, and resulted in a decrease in growth rate of ~15 % resulting from the recombination of pyrolyzed growth species and/or decomposition of GaN. In addition, the surface morphology of GaN was affected by atomic hydrogen, resulting in variations in the size of the surface pits. The variation in the surface morphology is a result of its influence on the surface adsorbed growth species. While the pit density and dimensions are affected, the overall roughness of the GaN layer is not significantly affected thus maintaining morphologies suitable for device applications. Furthermore, the introduction of atomic hydrogen to the growth of GaN has resulted in a ~20 % decrease in the incorporation of carbon. This decrease is associated with the increased liberation of adsorbed carbon-containing ethyl groups from the growth surface. Although a reduction in carbon is detected, the overall reduction is relatively minor and is suspected to be a result of either hydrogen recombination or hydrogen saturation on the growth surface. These results do not conclusively indicate that efficient cracking of molecular hydrogen may ultimately provide an effective means for carbon liberation but some benefit was realized for a first use of an atomic hydrogen source. Challenges in gas phase hydrogen recombination may ultimately limit its effectiveness.

CHAPTER 8: INVESTIGATION INTO THE FORMATION OF A 2DEG BY VARIOUS DEVICE STRUCTURES GROWN BY AMMONIA-BASED METAL-ORGANIC MOLECULAR BEAM EPITAXY

8.1 Introduction

In the previous chapters, epitaxial considerations and optimization for the development of NH_3-MOMBE HEMTs were explored. NH_3-MOMBE provides the ability to produce highly resistive GaN films, which may provide low-leakage buffer layers in HEMTs. Although these GaN layers have potential, no reported instance of III-Nitride HEMTs grown by NH_3-MOMBE exists. To investigate NH_3-MOMBE as a potential system for the deposition of III-Nitride HEMTs various device structures have been investigated to determine if the formation of a 2DEG in a HEMT structure grown by NH_3-MOMBE is feasible. Furthermore, the use of highly C-doped GaN buffers have been employed to determine if these highly resistive buffers can reduce leakage in the structure. In this chapter, several HEMT device structures were grown to determine if 2DEG formation is possible by NH_3-MOMBE.

8.2 Experimental Procedure

All films grown for this chapter were deposited in a custom NH_3-MOMBE growth reactor [54], with a base pressure of ~5 x 10^{-9} Torr. Details regarding the

preparation and cleaning of the substrates are described in Appendix A.1. For the growth of transistor structures, NH_3, TEGa, and TEAl were used as the precursors, which were introduced without carrier gases. The custom gas delivery system and subsequent pressure to flow rate conversions are described in Appendix A.2. Herein, all references to source precursors will be presented as flow rates.

For this study, GaN and AlGaN growth rates were measured *in situ* using a custom laser interferometry system [68]. Surface morphologies and surface roughnesses were measured by AFM, using a Veeco Nanoscape III AFM. Alloy compositions and crystalline quality were determined through 2θ-ω X-ray scans using a Philips XRD system. Additionally, XRD was used for RSMs around the $(\bar{1}04)$ reflection to determine accurate alloy composition and strain in the film. Finally, to verify the existence of a 2DEG, capacitance-voltage (C-V) measurements were done using a mercury probe station and an Agilent 4294A impedance analyzer, operated at a frequency of 10 kHz.

8.3 AlGaN/GaN Transistor Structure

Figure 8.1 shows a schematic of the AlGaN/GaN HEMT structure deposited for this study. The structure consists of a ~500 nm GaN buffer, followed by a ~20 nm $Al_{0.3}Ga_{0.7}N$ capping layer. To investigate the effect of carbon on the 2DEG, two different GaN buffer layers were used, a low temperature (770 °C) buffer and a high temperature (950 °C) buffer.

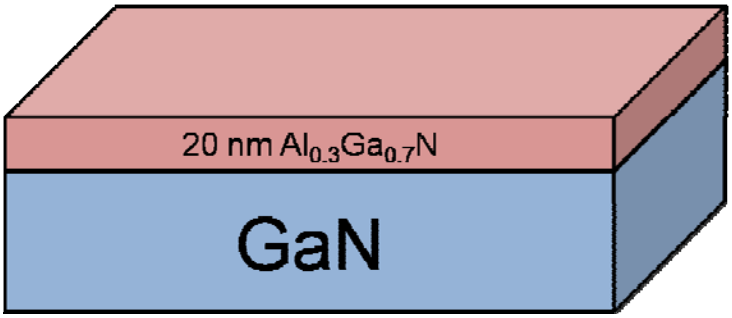

Figure 8.1: Schematic of traditional AlGaN/GaN HEMT structure. The structure consists of a ~500 nm GaN buffer layer and a ~20 nm $Al_{0.3}Ga_{0.7}N$ capping layer.

8.3.1 Low Temperature GaN Buffer

To achieve surface morphologies suitable for device structures, optimization of the low temperature GaN layer was first conducted. An AFM scan taken from a ~500 nm low temperature GaN layer is shown in Figure 8.2. The film exhibits an rms roughness value of ~3.5 nm, with surface pits ~40 nm deep. The regions of the AFM scan with no surface pits exhibit atomic steps, indicating step flow growth. These optimized conditions were grown at 770 °C with a TEGa flow rate of 0.3 sccm and an NH_3 flow rate of 50 sccm.

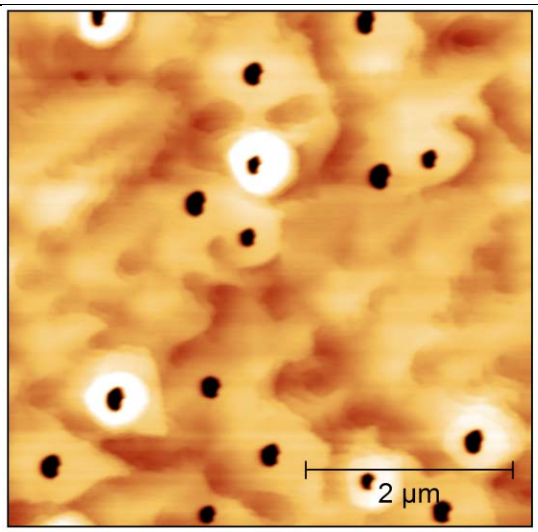

Figure 8.2: 5x5 μm AFM scan of low temperature GaN buffer exhibiting an rms roughness of ~3.5 nm. The z scale is 20 nm.

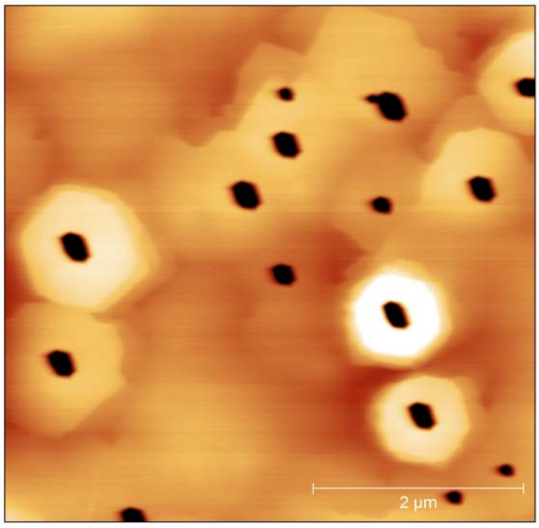

Figure 8.3: 5x5 μm AFM scan of AlGaN/GaN device structure exhibiting an rms roughness of ~3.7 nm. The z scale is 20 nm.

Following GaN deposition, a ~20 nm AlGaN cap layer was deposited at 950 °C with TEAl = 0.07 sccm, TEGa = 0.12 sccm and NH_3 = 10 sccm. The resulting morphology of the AlGaN/GaN device structure is shown in Figure 8.3. The film exhibits an rms roughness of ~3.7 nm, indicating no degradation in the surface morphology from the AlGaN layer. Once ensuring planar surface morphologies are obtainable, the AlGaN/GaN film was characterized by XRD to determine the crystalline quality and alloy composition. Figure 8.4 shows the XRD 2θ-ω scan of $Al_xGa_{1-x}N$ (002), indicating an Al composition of ~35%. XRD rocking curve FWHM of AlGaN (002) was ~350 arcsecs, indicating that material quality is limited by the GaN template. Figure 8.5 shows an XRD RSM around the $(\bar{1}04)$ reflection showing the GaN and AlGaN peaks. By defining the scattering vectors, Q_x and Q_y, the relative strain in the AlGaN film was determined from Equation 3.2, as was done previously. The relative strain between the GaN and AlGaN layers was calculated with a value of 1, indicating that the AlGaN film was fully strained to the underlying GaN buffer layer. This strain in the AlGaN layer is crucial because it provides the piezoelectric polarization which aids in the formation of the 2DEG at the AlGaN/GaN interface. Once verified, the sample was evaluated by C-V analysis to look for the existence of a 2DEG. Although all epitaxial conditions are met for 2DEG formation, no 2DEG was detected by C-V. After failing to form a 2DEG in a traditional AlGaN/GaN HEMT, the use of a high temperature GaN buffer was attempted.

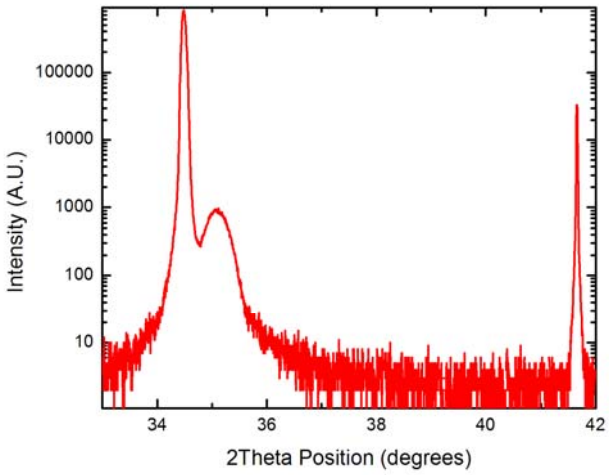

Figure 8.4: XRD 2θ-ω of AlGaN (002) grown on low temperature GaN buffer layer. The AlGaN peak corresponds to an Aluminum composition of ~35%.

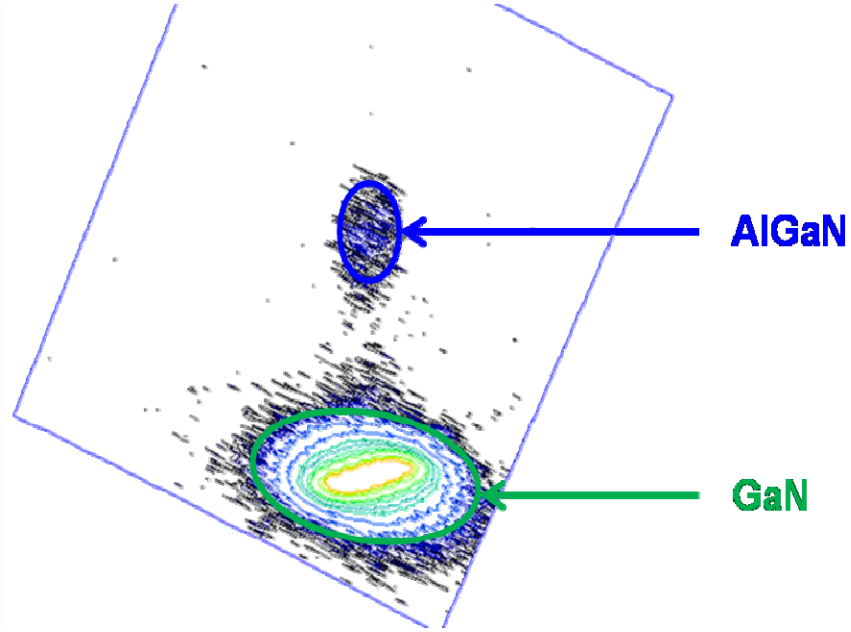

Figure 8.5: XRD Reciprocal Space Map of AlGaN and GaN ($\bar{1}04$) showing that the AlGaN film is fully strained to the underlying GaN buffer layer.

8.3.2 High Temperature GaN Buffer

With difficulties in forming a 2DEG utilizing a low temperature GaN buffer, efforts were focused on attempting HEMT structure on a high temperature (950 °C) GaN buffer. Again, the GaN buffer was optimized to provide high crystalline quality and planar surface morphology for the basis of the structure. The optimized high temperature GaN buffer's growth conditions are 950 °C growth temperature with TEGa = 0.36 sccm and NH_3 = 50 sccm. These growth conditions yield a XRD rocking curve FWHM of ~350 arcsecs with an rms roughness of ~10 nm. Figure 8.6 shows a 5x5 μm AFM scan of the optimized high temperature GaN buffer.

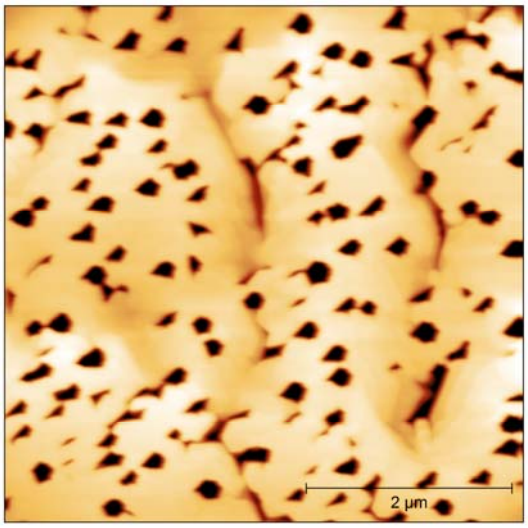

Figure 8.6: 5x5 μm AFM scan of optimized high temperature GaN buffer used for HEMT structures exhibiting an rms roughness of ~10 nm. The z scale is 40 nm.

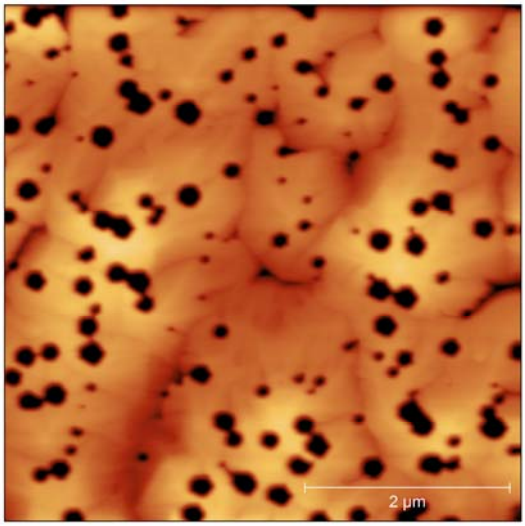

Figure 8.7: 5x5 μm AFM scan of an AlGaN/GaN device structure with a high temperature GaN buffer, exhibiting an rms roughness of ~7.75 nm. The z scale is 40 nm.

Once the GaN buffer was optimized, the AlGaN capping layer was deposited with the same conditions used previously. The resulting surface morphology of the AlGaN/GaN stack is shown in Figure 8.7. The ~20 nm AlGaN capping layer improves the overall surface morphology, exhibiting an overall rms roughness of ~7.75 nm.

To ensure the correct AlGaN composition and crystalline quality, a XRD 2θ-ω scan of the AlGaN/GaN structure was completed, and is shown in Figure 8.8. The peak at 2θ = 34.5° corresponds to GaN, the peak at 2θ = 34.8° corresponds to AlGaN with an Al composition of ~20 %, while the peak at 2θ = 41.6° corresponds to sapphire. The XRD rocking curve FWHM of the AlGaN (002) peak is ~350 arcsecs, again mimicking the quality of the GaN template. To ensure the AlGaN film was fully strained to the underlying GaN, a RSM around the ($\bar{1}$04) reflection was conducted, with the results shown in Figure 8.9. The results from the RSM indicate that the 20 % AlGaN film is fully strained to the underlying high temperature GaN buffer.

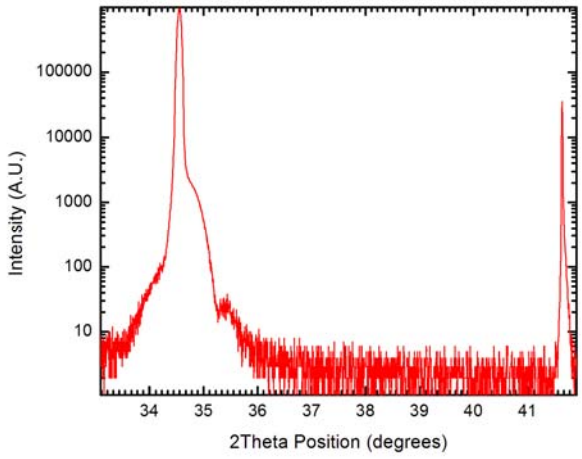

Figure 8.8: XRD 2θ-ω scan of AlGaN/GaN device structure with high temperature GaN buffer. The peak at $2\theta = 34.56°$ corresponds to GaN, the peak at $2\theta = 34.8°$ corresponds to $Al_{0.20}Ga_{0.80}N$, and the peak at $2\theta = 41.65°$ corresponds to sapphire.

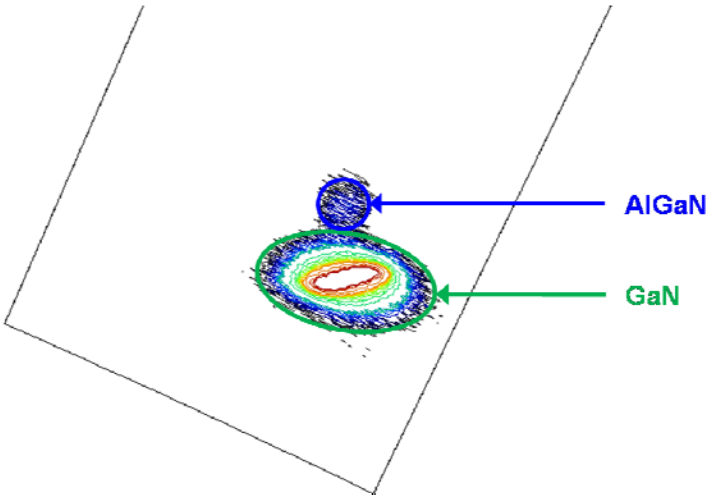

Figure 8.9: XRD Reciprocal space map of the GaN and AlGaN ($\bar{1}04$) reflections showing the existence of a fully strained AlGaN layer and underlying GaN layer. The fully strained AlGaN film is illustrated by the vertical alignment of the peaks.

After ensuring the high temperature GaN buffer and subsequent AlGaN capping layer met the epitaxial requirements for 2DEG formation, C-V measurements were conducted to determine if a 2DEG was formed. Figure 8.10 shows the C-V results taken from the AlGaN/GaN HEMT with a high temperature GaN buffer. These results indicate that a 2DEG is present at the AlGaN/GaN interface. Using the following equations,

$$N_A = 2 \,/\, q\, K_S\, \varepsilon_o\, A^2\, \frac{d(C^{-2})}{dV} \tag{8.1}$$

$$W_D = \frac{K_S\, \varepsilon_o\, A}{C} \tag{8.2}$$

the C-V data can be converted and re-plotted as charge density (N_A) versus W_D. In the above equations q = 1.6 x 10^{-19} C, the relative permittivity (K_S) = 9 (for GaN), the electric permittivity of free space (ε_o) = 8.85 x 10^{-12} F/m, and the contact area (A) = 2.04 x 10^{-6} m^2. Figure 8.11 shows the C-V data re-plotted as N_A versus W. When re-plotted as N_A versus W, the exponential increase in charge density indicates the existence of a 2DEG. The depth at which the charge increase occurs (~20 nm) corresponds to the thickness of the AlGaN capping layer. Additionally, the N_A versus W data illustrates the resistive nature of the C-doped GaN buffer. The decreased free carrier density (~1 x 10^{14} cm^3) of the GaN buffer results from the compensating nature of the C [55], reducing the density of free carriers in the material.

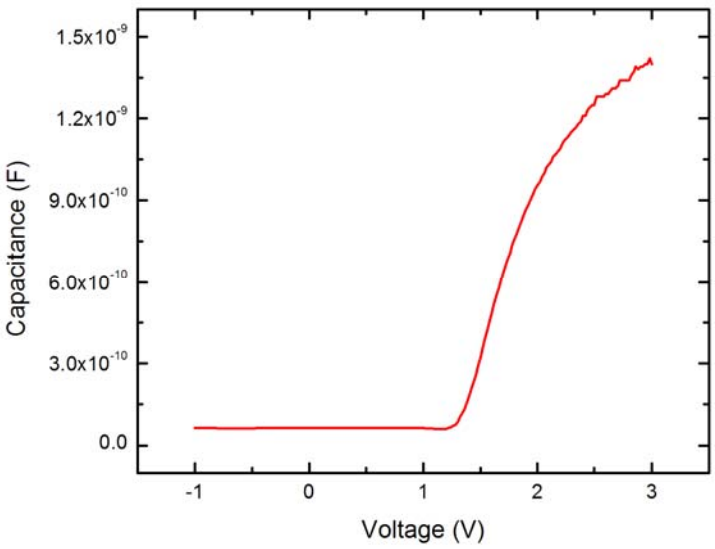

Figure 8.10: Capacitance-voltage data taken from AlGaN/GaN device structure with a high temperature GaN buffer.

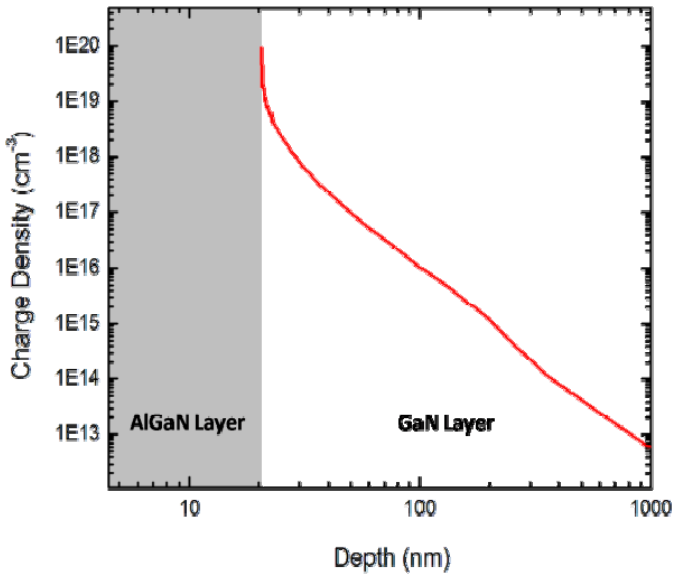

Figure 8.11: Charge density versus depth data calculated from the C-V results indicating the existence of a 2DEG ~20 nm below the surface.

8.3.3 Summary

This is the first reported existence of a 2DEG in an NH_3-MOMBE deposited AlGaN/GaN device structure. The results suggest that low temperature GaN buffers are not suitable for 2DEG formation. This absence of 2DEG at the AlGaN/GaN interface may be due to either increased carbon concentrations resulting from decreased deposition temperatures or degradation of the GaN surface morphology from the temperature ramp to reach the growth temperature for AlGaN. Utilizing high temperature GaN buffer layers, a 2DEG was successfully formed in an AlGaN/GaN structure. In addition, a low (~1 x 10^{14} cm^3) free carrier concentration was measured in the GaN buffer because of the highly resistive nature of the C-doped GaN. These results illustrate the promise of HEMT devices grown by NH_3-MOMBE utilizing a highly C-doped GaN buffer for reduced device leakage. With success in the formation of a 2DEG with a traditional AlGaN/GaN device structure, further studies were conducted in which an AlN interlayer was included in the device structure.

8.4 AlGaN/AlN/GaN Transistor Structure

Figure 8.12 shows a schematic of an AlGaN/AlN/GaN HEMT device structure. By inserting a thin (~10 Å) AlN interlayer between the AlGaN and GaN layers, a larger band discontinuity is formed and alloy scattering is eliminated [72, 152, 153]. Because of these benefits, increased 2DEG mobilities and sheet charge densities can be achieved.

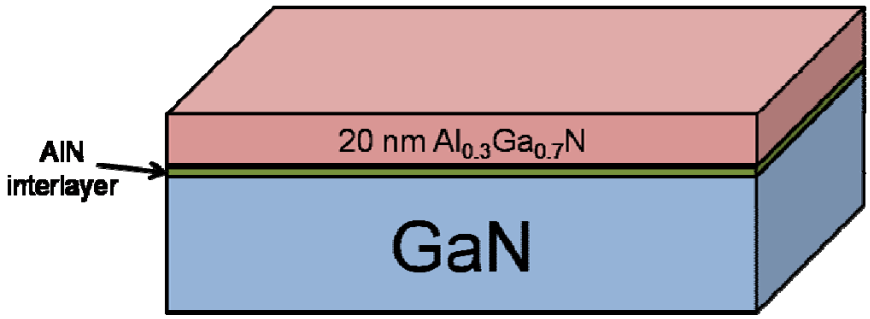

Figure 8.12: Schematic of AlGaN/AlN/GaN device structure. The structure consists of a ~500 nm thick GaN buffer layer, ~10 Å thick AlN interlayer, and a ~20 nm thick $Al_{0.3}Ga_{0.7}N$ layer.

8.4.1 Low Temperature GaN Buffer

Again, the influence of the growth temperature of the GaN buffer was investigated for this transistor structure. The growth of the AlN interlayer was optimized for these devices with the optimized AlN growth conditions consisting of a growth temperature of 950 °C with a TEAl flow rate of 0.06 sccm and NH_3 flow rate of 17 sccm. Precise control of the AlN thickness is imperative to maintain strain in the structure. Figure 8.13 shows a resulting AFM morphology of an AlGaN/AlN/GaN structure with an AlN interlayer that is too thick. Because of the high strain in the AlN layer, surface cracks form to alleviate the strain, which in turn eliminates the piezoelectric polarization in the device, reducing the sheet charge density of the 2DEG.

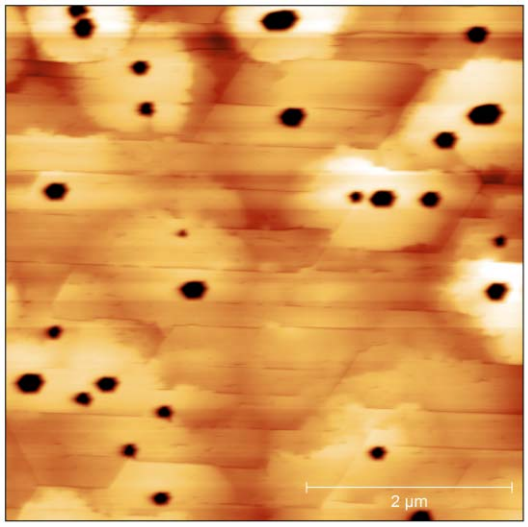

Figure 8.13: 5x5 μm AFM scan of AlGaN/AlN/GaN device structure with an AlN interlayer >10 Å. Surface cracking is seen due to the thick AlN interlayer. The z scale is 20 nm.

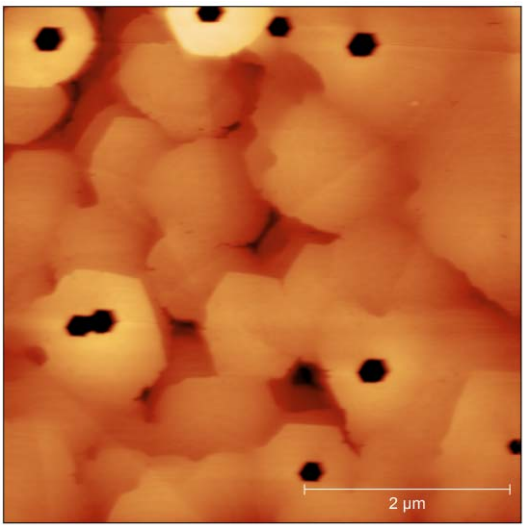

Figure 8.14: 5x5 μm AFM scan of AlGaN/AlN/GaN device structure with an optimized AlN thickness and resulting rms roughness of ~3.4 nm. The z scale is 20 nm.

Figure 8.14 shows an AFM surface morphology of an optimized AlGaN/AlN/GaN device structure with the appropriate AlN interlayer thickness. The addition of an optimized AlN interlayer results in an rms roughness of ~3.4 nm, showing no obvious surface morphology degradation. In addition, when the morphology was examined more closely in regions without surface pitting, it was found that the surface exhibited atomic steps, indicating step-flow growth. Figure 8.15 shows XRD 2θ-ω scans of AlGaN (002) that exhibit Pendellösung fringes. Each layer of the device structure is clearly visible with the GaN peak at $2\theta = 34.56°$, AlGaN at $2\theta = 35.1°$ which corresponds to ~35 % Al composition, and AlN at $2\theta = 36°$. The remaining peaks are Pendellösung fringes, which indicate that the layers exhibit abrupt interfaces and also that the layers are planar. By determining the interference periods of the Pendellösung fringes an accurate calculation of the thickness of the AlGaN layer can be determined using the following equation

$$\Delta\omega = \frac{\lambda * \sin(\Phi)}{t * \sin(2\theta)} \tag{8.3}$$

where $\Delta\omega$ is the fringe spacing, λ is the x-ray wavelength (1.54 Å for Cu-K_α), Φ is angle difference between the diffracted beam and the sample surface, t is the film thickness, and 2θ is the average value of 2Theta for two adjacent fringes. Using this equation and solving for thickness, an accurate thickness for the AlGaN capping layer of 20 nm ± 0.05 Å is determined. Once verifying the correct AlGaN thickness, XRD rocking curves of AlGaN and AlN (002) was conducted to verify the quality of both epitaxial layers. The

XRD rocking curve measurements taken from the AlGaN and AlN (002) reflections of the AlGaN/AlN/GaN device structure are shown in Figures 8.16 and 8.17. The calculated rocking curve FWHM for the AlGaN and AlN layers are 350 and 365 arcsecs, respectively. As indicated by the narrows FWHMs, both layers are of high quality and mimic the quality of the GaN template.

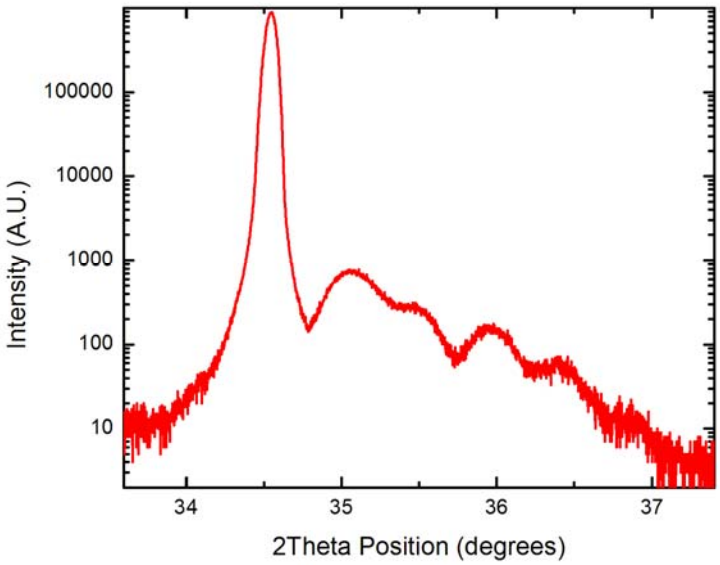

Figure 8.15: XRD 2θ-ω of AlGaN (002) showing GaN (34.5°), AlGaN (35.1°) and AlN (36°) peaks. The scan also shows Pendellösung fringes indicating abrupt interfaces and planar surface morphologies. The spacing between the Pendellösung fringes indicates an AlGaN layer thickness of ~20 nm.

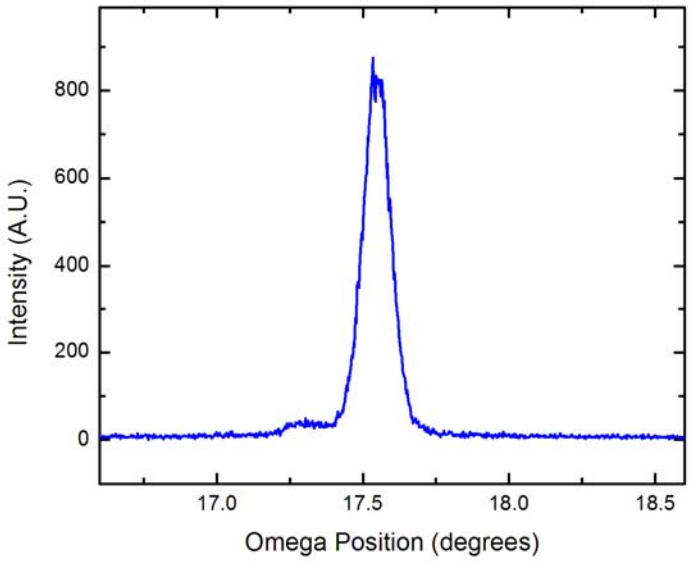

Figure 8.16: XRD rocking curve of $Al_{0.35}Ga_{0.65}N$ (002) with FWHM value of ~350 arcsecs, illustrating the high quality of the AlGaN capping layer.

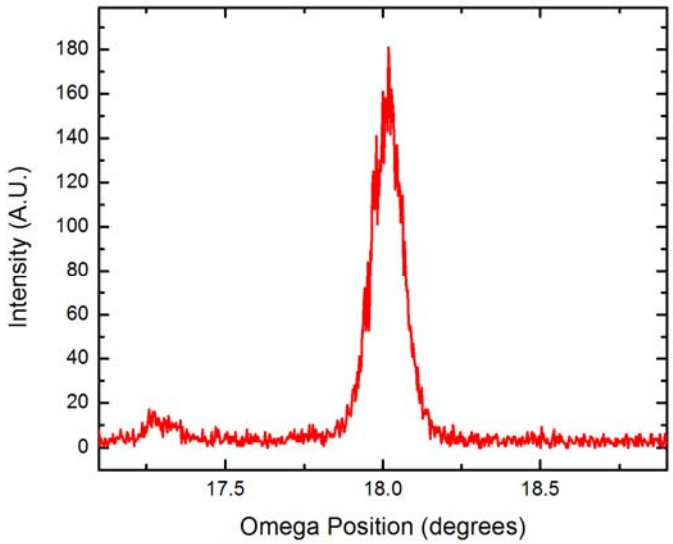

Figure 8.17: XRD rocking curve of AlN (002) with FWHM value of ~365 arcsecs, illustrating the high quality of the AlN interlayer.

Finally, to ensure that both the AlN and AlGaN layers are fully strained to the GaN film, a RSM around the GaN ($\bar{1}04$) reflection was conducted. Figure 8.18 shows the RSM taken around the GaN ($\bar{1}04$) reflection, showing the existence of the GaN, AlGaN and AlN peaks. The vertical alignment of all three peaks indicates that both the AlN and AlGaN films are still fully strained to the GaN film.

Once verifying that all epitaxial aspects (planar morphology, strained AlGaN layers, correct AlGaN composition, and proper crystalline quality) necessary for HEMT operation have been met, the sample was characterized by C-V to determine whether a 2DEG was formed. Again the C-V showed no change in capacitance, similar to the AlGaN/GaN structure grown on the low temperature GaN buffer, indicating that no 2DEG was formed at the interface. Again, either the temperature ramp following the GaN buffer deposition or the increased carbon levels in the GaN buffer are suspected to prevent the formation of the 2DEG.

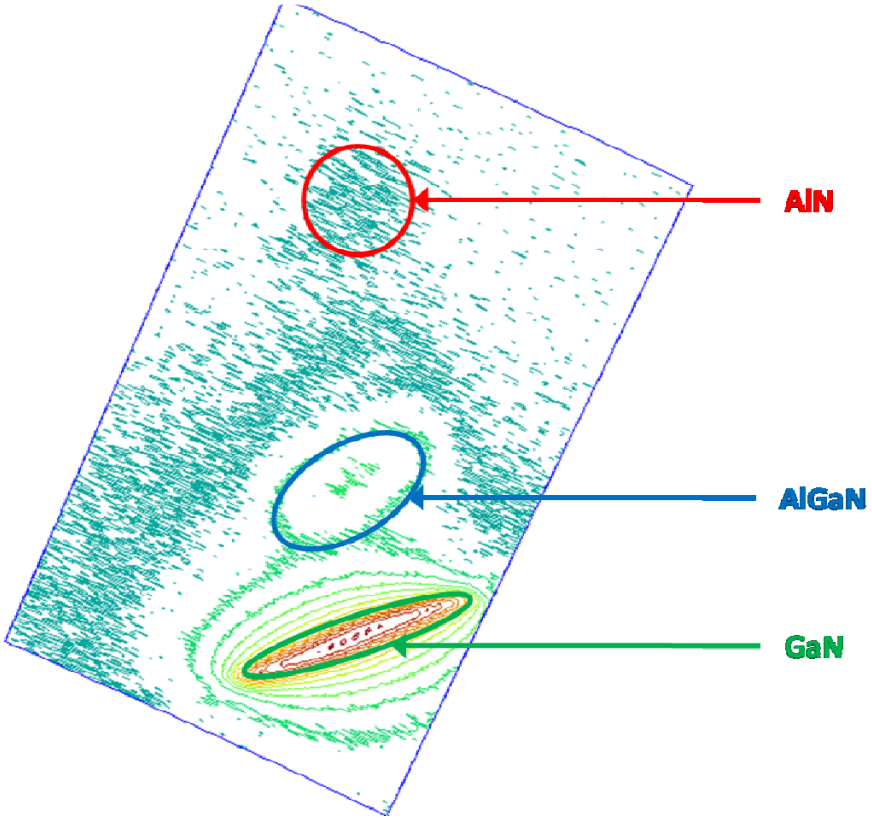

Figure 8.18: XRD Reciprocal space map of the ($\bar{1}$04) reflections showing the existence of AlN and AlGaN layers that are fully strained to the GaN peak. The strain is indicated by the vertical alignment of all three peaks.

8.4.2 High Temperature GaN Buffer

A high temperature GaN buffer was employed in the AlGaN/AlN/GaN structure similarly to what was done with the AlGaN/GaN structure. Again, to verify the device structure maintained suitable surface morphologies, AFM scans were taken of the completed device. Figure 8.19 shows a 5x5 μm AFM scan taken from the final AlGaN/AlN/GaN device structure. The surface morphology of the completed device

exhibits an rms roughness of ~10.5 nm, which mimics the morphology of the high temperature GaN buffer shown in Figure 8.6.

Figure 8.20 shows the XRD 2θ-ω scans of AlGaN (002) which exhibits Pendellösung fringes, which are the reflections not corresponding to GaN (2θ =34.5°) or AlGaN (2θ = 35°). The AlGaN peak (2θ = 35°) corresponds to an Al composition of ~30 % and whose Pendellösung fringe spacing corresponds to a film thickness of ~22 nm. The crystalline quality of the AlGaN layer was quantified through XRD rocking curve of the AlGaN (002) reflection and it was found that the quality again mimicked the GaN template, with a FWHM of ~360 arcsecs.

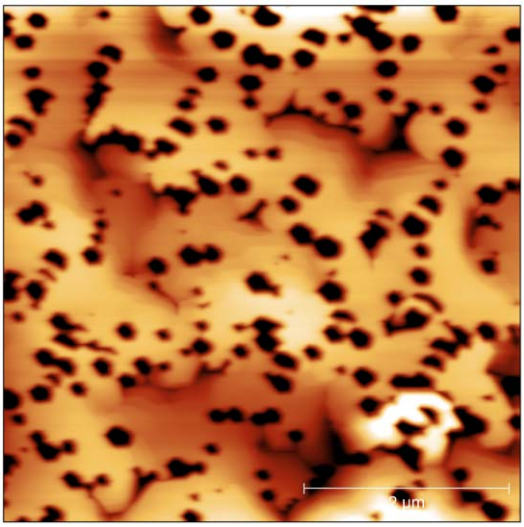

Figure 8.19: 5x5 μm AFM scan of AlGaN/AlN/GaN device structure with high temperature GaN buffer. The device structure exhibits an overall rms roughness of ~10.5 nm. The z scale of the image is 40 nm.

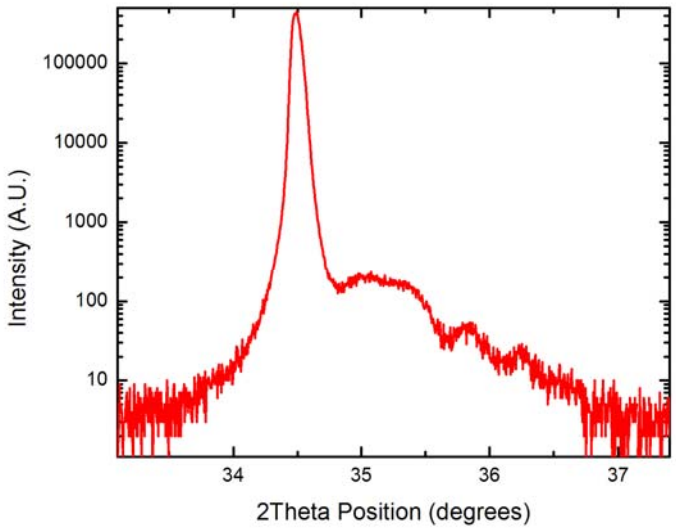

Figure 8.20: XRD 2θ-ω scan of AlGaN (002) reflection showing an AlGaN layer with ~30 % Al composition. The AlGaN layer also exhibits Pendellösung fringes which correspond to a film thickness of ~22 nm.

The AlGaN/AlN/GaN device structure was then analyzed by RSM around the GaN ($\bar{1}$04) reflection to ensure the films were fully strained to the underlying GaN buffer layer. Figure 8.21 shows the results of the RSM. Although the AlN interlayer is not clearly identified in the RSM, the AlGaN capping layer is identified and remains fully strained to the underlying GaN layer.

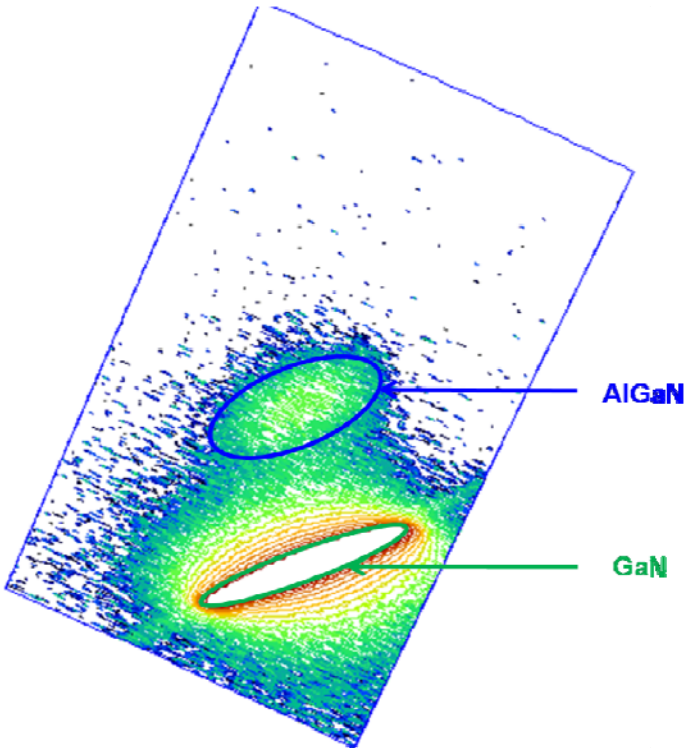

Figure 8.21: XRD Reciprocal space map around the ($\bar{1}$04) reflections of the AlGaN/AlN/GaN device structure with a high temperature GaN buffer. The vertical alignment of the peaks indicates that the AlGaN layer is fully strained to the underlying GaN buffer layer.

Following the characterization to ensure the necessary devices requirements were met for the AlGaN/AlN/GaN device, a C-V measurement was done to determine the existence of a 2DEG at the AlN/GaN interface. Figure 8.22 shows the results of the C-V measurement, showing an abrupt increase in the capacitance at a given voltage. These results were again converted to N_A and W_D using Equations (8.1) and (8.2) and re-plotted in Figure 8.23. Again the charge density increases exponentially indicating the existence of a 2DEG, although the calculated depth of the 2DEG is ~1.75 times greater than what was expected. The target thickness of the AlGaN/AlN layers was ~25 nm, which corresponds to the measured 2DEG depth in Figure 8.23. Similarly to the AlGaN/GaN device structure, the AlGaN/AlN/GaN device structure exhibits a low free carrier

concentration in the GaN buffer of ~5 x 10^{15} cm^3. This illustrates the resistive nature of the C-doped GaN buffer through compensation of the free carriers.

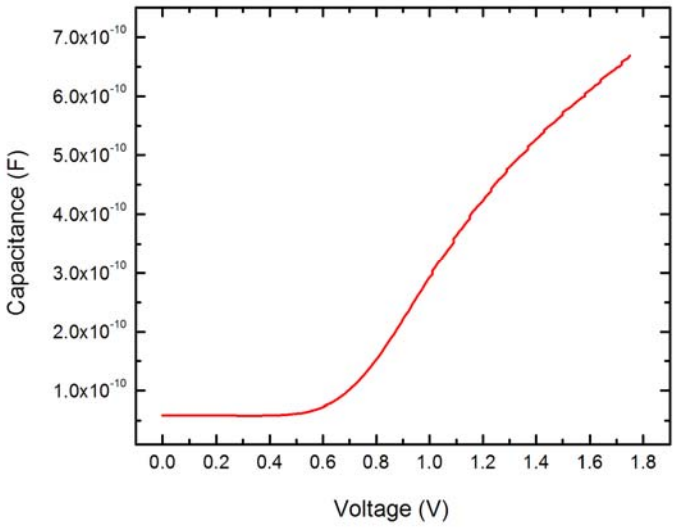

Figure 8.22: Capacitance-voltage measurement taken from the AlGaN/AlN/GaN device structure with a high temperature GaN buffer.

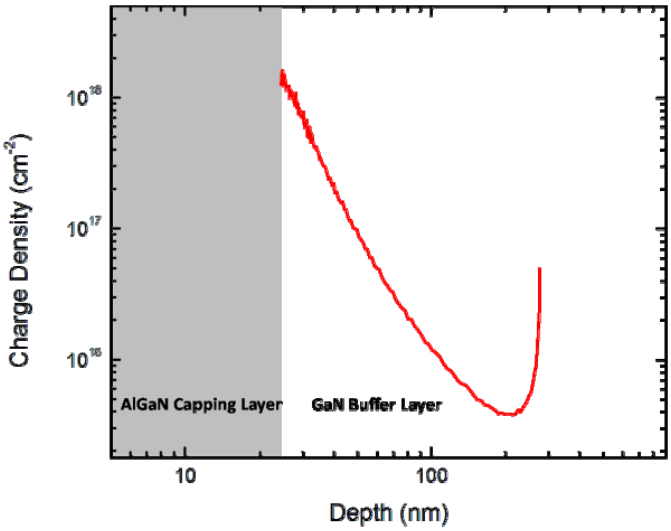

Figure 8.23: Depth versus charge density profile for the AlGaN/AlN/GaN device structure with a high temperature GaN buffer.

8.4.3 Summary

Results from this section demonstrate the first reported AlGaN/AlN/GaN transistor structure grown by NH_3-MOMBE. The study suggests that low temperature GaN buffers are not suitable for 2DEG formation, most likely attributed to either surface morphology degradation from the temperature ramp or increased carbon incorporation. Using high temperature GaN buffers, successful formation of a 2DEG in an AlGaN/AlN/GaN device structure was achieved. In addition, the self-compensation nature of C-doped GaN leads to a low (~1 x 10^{14} cm^3) free carrier density in the GaN buffer, highlighting the promise of this buffer layer to reduce device leakage. These results illustrate the promise in NH_3-MOMBE grown GaN buffer layers for their utilization in HEMTs with reduced device leakage. Further studies were conducted to determining if AlGaN-based device structures grown by NH_3-MOMBE would also be successful in 2DEG formation.

8.5 AlGaN/AlGaN Transistor Structure

Figure 8.24 shows a schematic of an all Al-alloy $Al_xGa_{1-x}N/Al_yGa_{1-y}N$ device structure. This device utilizes the variations in Al composition between the two layers to provide the piezoelectric polarization aspect to induce formation of a 2DEG at the interface. Although increased alloy scattering will occur in AlGaN/AlGaN device

structures [152, 153], an all AlGaN device structure allows for an increased breakdown voltage while retaining the comparable power densities obtainable in AlGaN/GaN device structures.

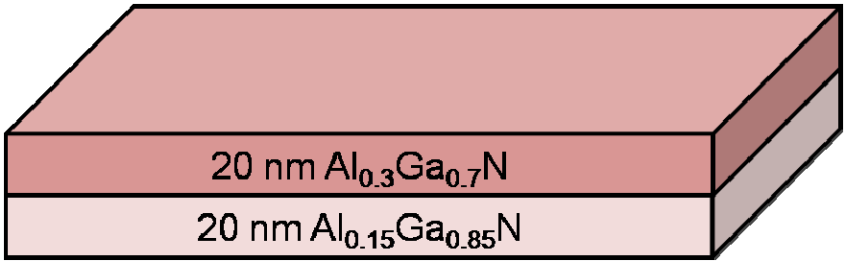

Figure 8.24: Illustration of an $Al_xGa_{1-x}N/Al_yGa_{1-y}N$ device structure. The structure consists of a ~20 nm thick $Al_{0.15}Ga_{0.85}N$ layer and a subsequent ~20 nm thick $Al_{0.3}Ga_{0.7}N$ layer.

For the growth of AlGaN/AlGaN device structures, two ~20 nm AlGaN layers were deposited, with varying Al compositions. The films were deposited at 950 °C, with a constant TEAl flow rate of 0.07 sccm, with a TEGa flow rate of 0.12 for 30 % Al and 0.17 sccm for 15 % Al composition. These layers were deposited directly onto the GaN template, without the use of a NH_3-MOMBE grown GaN buffer. Two structures were deposited, each with identical growth conditions except that the thicknesses of the AlGaN layers were varied from 20nm to 15nm.

Figures 8.25 and 8.26 show the surface morphologies of both structures, as measured by AFM. Because of the deposition of thin AlGaN layers, the surface morphologies mimic the morphology of the GaN template, resulting in rms roughness values of ~0.4 nm. The device structure with AlGaN layer thicknesses of ~20 nm exhibit larger surface pits, as these surface pits enlarge with layer thickness.

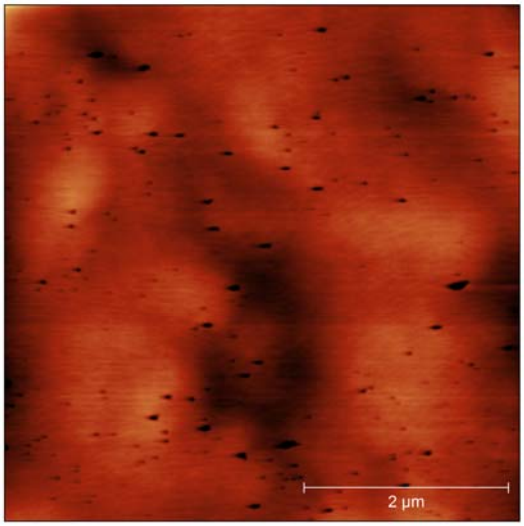

Figure 8.25: 5x5 μm AFM scan of AlGaN/AlGaN device structure with ~20 nm layer thicknesses, exhibiting an rms roughness of ~0.45 nm. The scan z scale is 5nm.

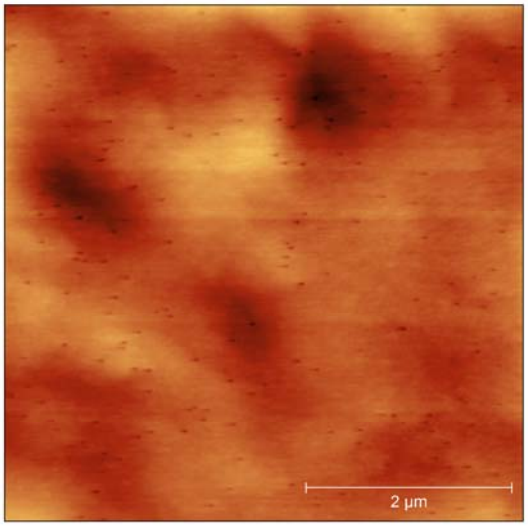

Figure 8.26: 5x5 μm AFM scan of AlGaN/AlGaN device structure with ~15 nm layer thicknesses, exhibiting an rms roughness of ~0.40 nm. The scan z scale is 5nm.

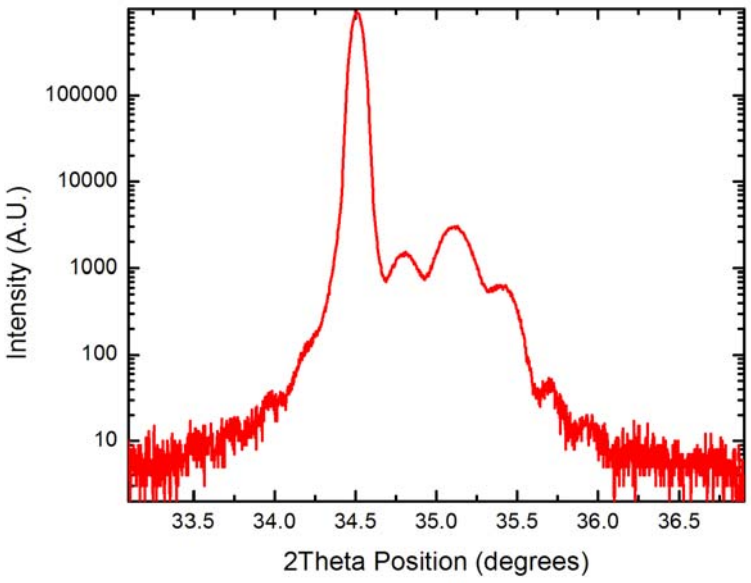

Figure 8.27: XRD 2θ-ω scan of AlGaN (002) indicating two distinct AlGaN compositions of 16 and 30 %. Also the existence of Pendellösung fringes verifies an AlGaN layer thickness of ~18 nm.

Figure 8.27 shows the XRD 2θ-ω scan taken from the AlGaN/AlGaN structure with ~20 nm layers, indicating the two distinct AlGaN compositions of the structure. The XRD scan indicates that the AlGaN layer compositions of the structure are ~16 % Al (2θ = 34.8°) and ~30 % Al (2θ = 35°). In addition, the existence of Pendellösung fringes verify the AlGaN layer thickness at ~18 nm ± 0.7 nm, illustrating the thickness control capability of the NH_3-MOMBE growth system.

Similarly to AlGaN/GaN heterostructures, AlGaN/AlGaN device structures rely partially on piezoelectric strain to form a 2DEG. To confirm that strain in the AlGaN layers is present, a RSM around reflection GaN ($\bar{1}04$) was conducted. The results of the RSM are shown in Figure 8.28. The RSM results show the two distinct AlGaN compositions and also confirm that the AlGaN layers are fully strained to the underlying GaN template.

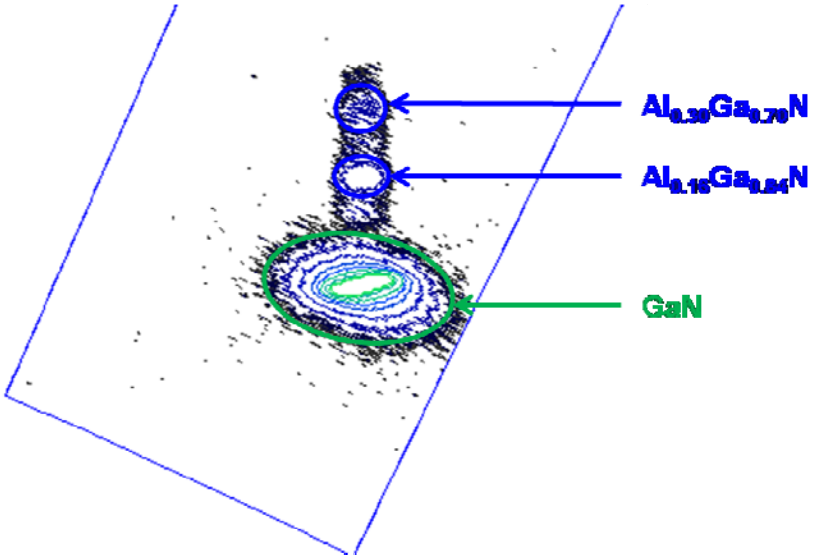

Figure 8.28: XRD Reciprocal space map around the ($\bar{1}04$) reflections of the AlGaN/AlGaN device structure. The vertical alignment of all three peaks indicates that the AlGaN layers are fully strained to the underlying GaN template.

Once all necessary components of 2DEG formation were confirmed through characterization, a C-V measurement was conducted to determine the existence of a 2DEG at the AlGaN/AlGaN interface. Figure 8.29 show the C-V results taken from the AlGaN/AlGaN device structure with ~20 nm layer thicknesses. The C-V data was converted to charge density and depletion width through Equation 8.1 and re-plotted in Figure 8.30. The data verifies the existence of a 2DEG at the AlGaN/AlGaN interface, with a depth of ~20 nm, corresponding to the thickness of the AlGaN layer. The second device structure with AlGaN layer thicknesses of ~15 nm was also characterized by C-V. The charge densities versus depletion depth data for that device structure are shown in Figure 8.31. The AlGaN/AlGaN structure with thinner AlGaN layers also exhibits a 2DEG with a calculated depletion width of ~15 nm, which corresponds to the thickness of the AlGaN layers. This study shows that AlGaN/AlGaN device structures grown by

NH_3-MOMBE are capable of forming 2DEGs, increasing the potential device possibilities of this growth system.

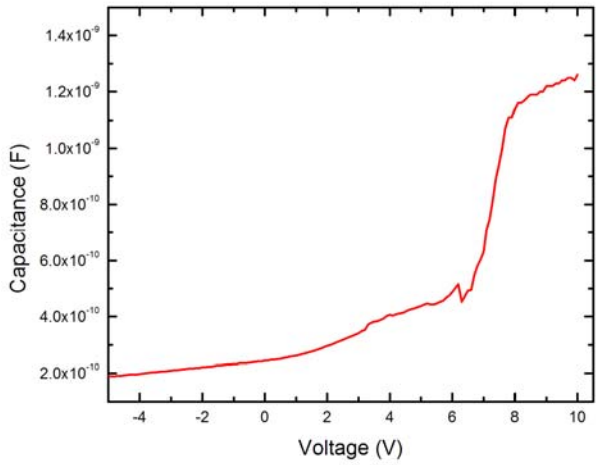

Figure 8.29: Capacitance-voltage data taken from AlGaN/AlGaN device structure with AlGaN layer thickness of ~20 nm.

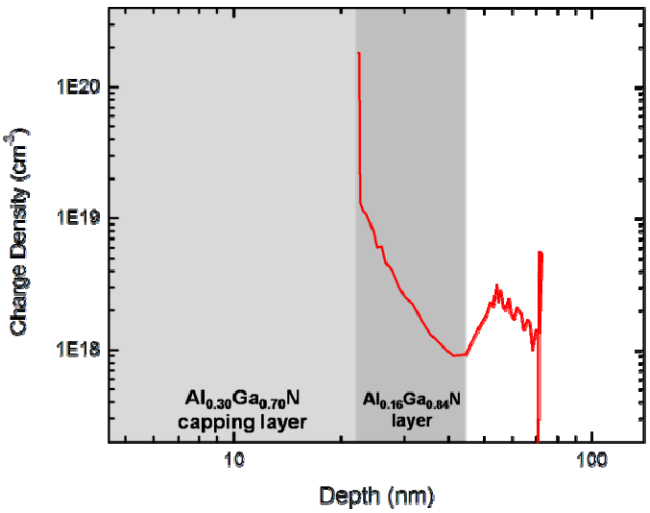

Figure 8.30: Charge density versus depletion width results calculated for the AlGaN/AlGaN device structure with AlGaN layer thicknesses of ~20 nm.

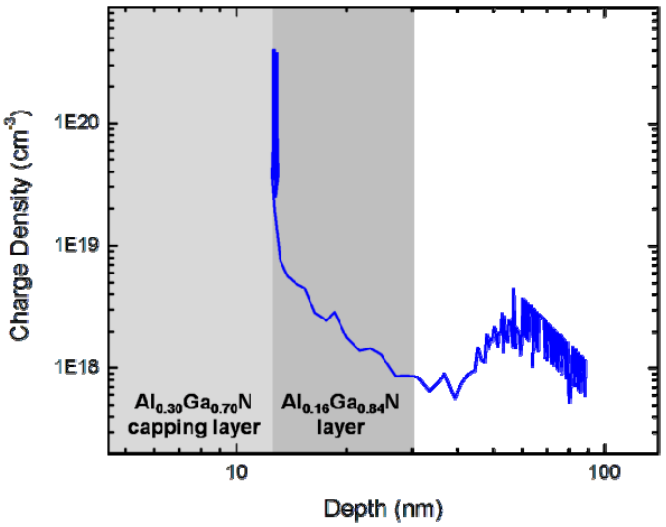

Figure 8.31: Charge density versus depletion width results calculated for the AlGaN/AlGaN device structure with AlGaN layer thicknesses of ~15 nm.

8.6 Device Structures on Non-conductive Substrates

The previous device structures were all deposited on Si-doped GaN templates, which made electrical characterization impossible because of the conductivity of the template. In an attempt to quantify the electrical performance of these structures, the growth parameters were transferred over to Lumilog UID GaN templates. The resistivity of the UID GaN templates is quoted as >1 kΩ-cm, while the Si-doped templates have a resistivity of ~10 mΩ-cm. All device structures in this section were grown with high temperature GaN buffer layers because of the lack of success with low temperature buffers for structures on Si-doped GaN templates.

8.6.1 AlGaN/GaN Transistor Structure on UID GaN

Figure 8.32 shows the surface morphology of an AlGaN/GaN device structure with a ~500 nm high temperature GaN buffer, deposited on a UID GaN template. These morphologies exhibit rms roughness values in excess of 30 nm, which is an order of magnitude greater than the values obtained on Si-doped GaN templates. The laser intensity oscillations obtained by the laser interferometry system during the growth of the GaN buffer showed significant decreases in the laser intensity, indicating a roughening of the surface during deposition [68]. The dampening of the laser oscillations during the growth of the GaN buffer is illustrated in Figure 8.33. The degradation in the surface morphologies of the films is expected to be a result of inconsistencies in the metallization of the templates. Variations in the quality of the back metallization of the templates would result in variations in the emissivity of the material, resulting in growth temperature differences that lead to morphological variations of the film. The morphology of the GaN buffer was optimized through laser oscillation optimization, in which it was found that a 10 °C decrease in the growth temperature resulted in no decrease in laser oscillation intensity, as seen in Figure 8.34. The optimized growth temperature of 940 °C resulted in the surface morphologies seen in Figure 8.35, which exhibit rms roughness values of ~3.5 nm. This ten times increase in surface roughness (3.5 nm → 30 nm) for a relatively minor increase in growth temperature (940 °C → 950 °C) illustrates the complexity of growth for III-Nitrides in an NH_3-MOMBE growth system.

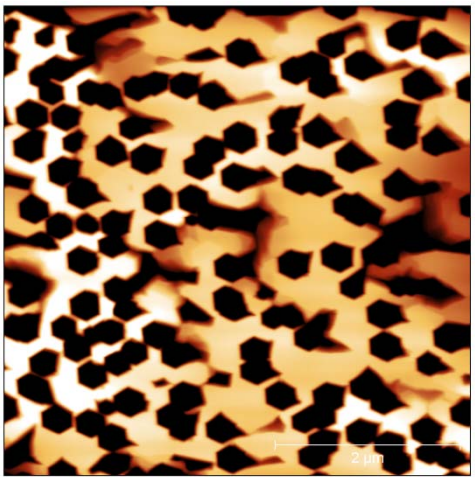

Figure 8.32: 5x5 μm AFM scan of AlGaN/GaN device structure grown with a high temperature GaN buffer on a UID GaN template. The surface exhibits an rms roughness value of ~30 nm. The z scale of the image is 40 nm.

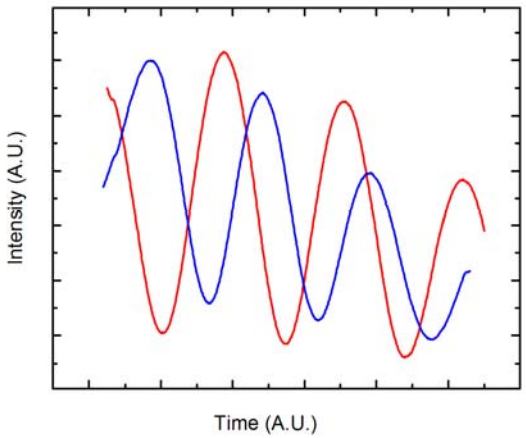

Figure 8.33: Laser interferometry signals from the growth of high temperature GaN on UID templates, showing a dampening of the signal intensity indicating degradation of the GaN surface morphology.

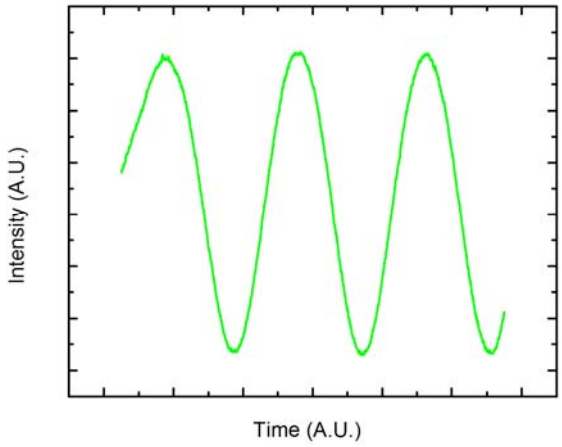

Figure 8.34: Laser interferometry signal from the growth of GaN at the optimized growth temperature of 940 °C resulting in no dampening of the laser oscillation intensity, indicating no degradation of the surface morphology.

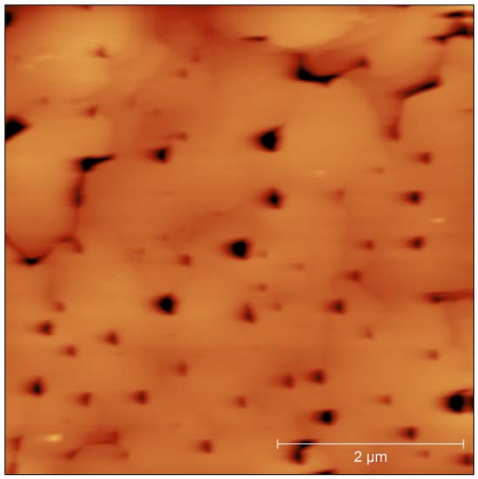

Figure 8.35: 5x5 μm AFM scan of AlGaN/GaN device structure grown at the re-optimized growth temperature of 940 °C, resulting in an rms roughness of ~3.5 nm. The z scale of the AFM image is 40 nm.

Following optimization of growth conditions, the AlGaN/GaN structures were characterized by XRD, with the results of 2θ-ω scan seen in Figure 8.36. The AlGaN peak at $2\theta = 35°$ corresponds to an Al composition of ~30 %. The quality of the AlGaN layer was verified by XRD rocking curve of AlGaN (002), which exhibited a FWHM of ~325 arcsecs, as seen in Figure 8.37. The FWHM value mimics that of the GaN template, indicating the AlGaN layer is of high crystalline quality.

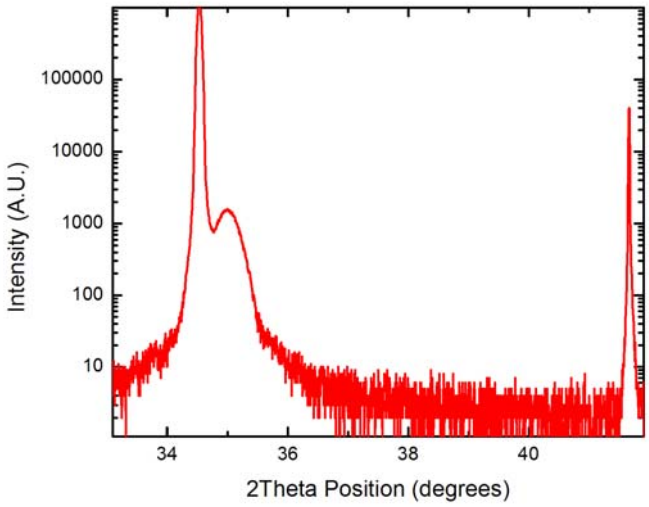

Figure 8.36: XRD 2θ-ω of AlGaN (002) showing an AlGaN peak at $2\theta = 35°$ which corresponds to an Al composition of ~30 %.

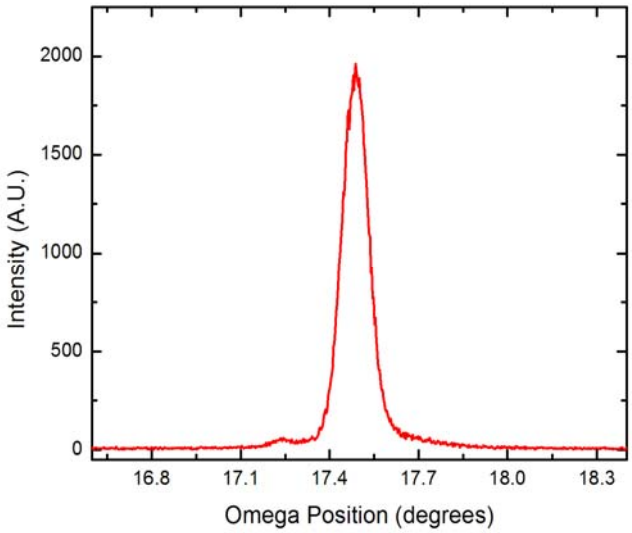

Figure 8.37: XRD rocking curve of AlGaN (002) exhibiting a FWHM value of ~325 arcsecs, indicating high crystalline quality AlGaN.

To verify that the AlGaN capping layer remained fully strained to the underlying GaN buffer layer, a RSM around the GaN ($\bar{1}04$) reflection was conducted and is shown in Figure 8.38. The RSM verifies that the AlGaN layer is strained to the GaN buffer layer, which is determined by the vertical alignment of the peaks.

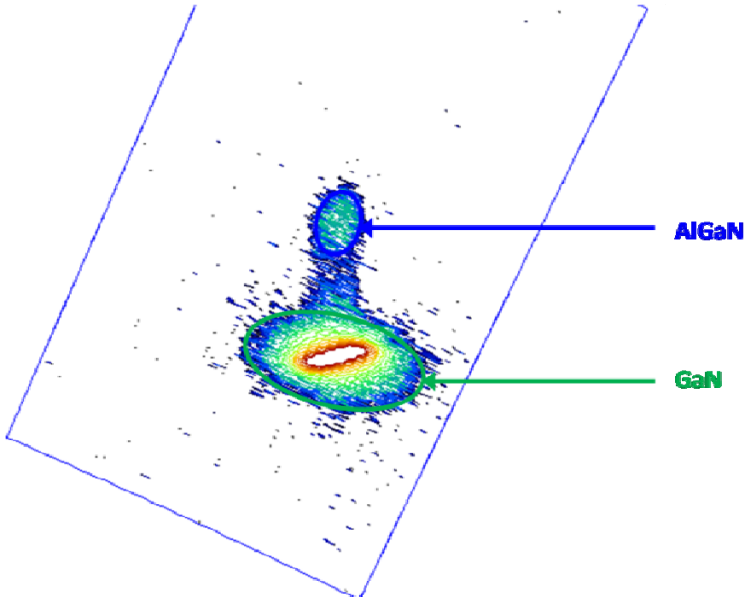

Figure 8.38: XRD reciprocal space map around the ($\bar{1}$04) reflections showing the GaN and AlGaN peaks of the AlGaN/GaN structure. The vertical alignment of the peaks indicates that the AlGaN layer is fully strained to the GaN buffer layer.

Following device characterization, a C-V measurement was conducted to determine the existence of a 2DEG at the AlGaN/GaN interface. The results of the C-V measurements are shown in Figure 8.39. As indicated by the figure, a successful 2DEG was formed at the interface, although the charge density was approximately an order of magnitude lower than the densities obtained on the Si-doped GaN templates, indicating that the charge in the template may contribute to the 2DEG density. In addition, the depletion width indicates a 2DEG depth of ~65 nm, while the target AlGaN thickness was ~25 nm. This discrepancy is a result of a leaky contact between the device and the mercury probe, due to the low Schottky barrier provided by Hg contacts. The work function (φ) of Hg is ~4.5 eV, while GaN has a work function of 4.1 eV. This contact leakage and the series resistance associated with a lateral dimension between H probe

contacts of 0.5 mm and a channel depth of only ~70 angstroms results in an additional series resistance that is not accounted for in the parallel RC model used by the impedance analyzer. This series resistance error results in increased measured impedance. This increased impedance is erroneously calculated as an increased capacitance via the parallel RC model, which in turn results in increased measured depletion widths [154].

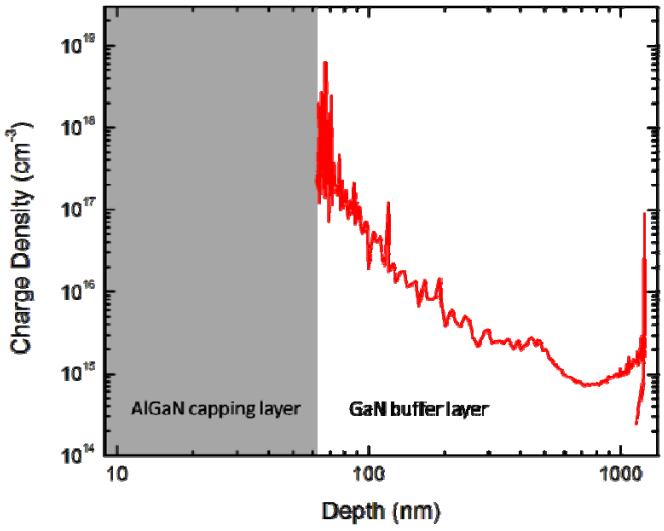

Figure 8.39: Charge density versus depletion width results from AlGaN/GaN structure grown on UID GaN template utilizing a high-temperature GaN buffer layer.

8.6.2 AlGaN/AlN/GaN Transistor Structure on UID GaN

Following the unsuccessful attempts at forming a 2DEG with an AlGaN/GaN structure on UID GaN templates, an AlN layer was inserted into the device structure to

determine if the AlN layer would aid in the formation of a 2DEG. With the insertion of the AlN interlayer, the device structure was characterized to determine if the epitaxial considerations were met for 2DEG formation. Figure 8.40 shows an AFM scan illustrating the surface morphology resulting from the insertion of the AlN interlayer. The structure exhibits an rms roughness of ~4.8 nm, which is comparable to the AlGaN/GaN morphology.

To determine the composition of the AlGaN layer and to verify the existence of the AlN interlayer, a XRD 2θ-ω scan of the (002) reflections was taken and is shown in Figure 8.41. The peaks at $2\theta = 35°$ corresponds to AlGaN with an Al composition of ~30 %, and the peak at $2\theta = 36°$ corresponds to AlN. Also, Pendellösung fringes are again visible for this structure. The spacing of the fringes correspond to an AlGaN layer thickness of 21 nm ± 0.2 nm, which confirms the target AlGaN thickness. To further characterize the individual layers, XRD rocking curves of the AlGaN and AlN (002) reflections were conducted, which are shown in Figures 8.42 and 8.43, respectively. From the XRD rocking curves, the FWHM values for both AlGaN and AlN were determined. The AlGaN layer exhibited a FHWM of ~560 arcsecs, while the AlN interlayer exhibited a FWHM of ~410 arcsecs. These values are higher than those measured for the AlGaN/AlN/GaN device structure grown on the Si-doped GaN templates, which exhibited FWHM values of ~350 and 365 arcsecs, for AlGaN and AlN respectively. The decreased crystalline quality of AlGaN and AlN grown on UID templates may result from the decreased growth temperature necessary to achieve planar GaN.

After determining the crystalline quality of the individual layers, a XRD RSM was conducted to determine the strain in the AlGaN and AlN layers. Figure 8.44 shows the results of the RSM taken around the $(\bar{1}04)$ reflections. Although the low intensity of the AlN peak is not visible on the RSM, the vertical alignment of the AlGaN and GaN peaks indicate that the films are fully strained.

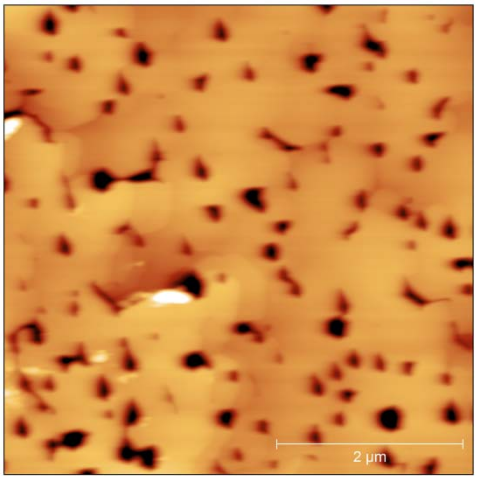

Figure 8.40: 5x5 μm AFM scan showing the surface morphology of an AlGaN/AlN/GaN structure deposited on UID GaN template. The surface morphology exhibits an rms roughness of ~4.8 nm. The image z scale is 40 nm.

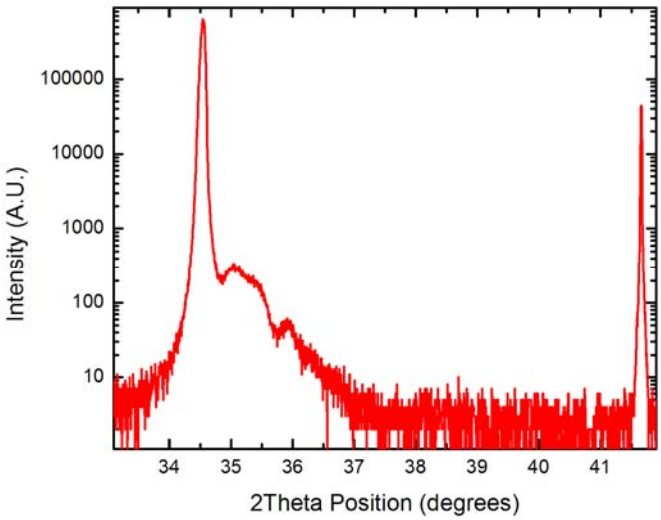

Figure 8.41: XRD 2θ-ω scan of the (002) reflections of GaN, AlGaN, and AlN. The peak at 2θ = 35° corresponds to an AlGaN composition of 30%, Al and the peak at 2θ = 36° corresponds to AlN.

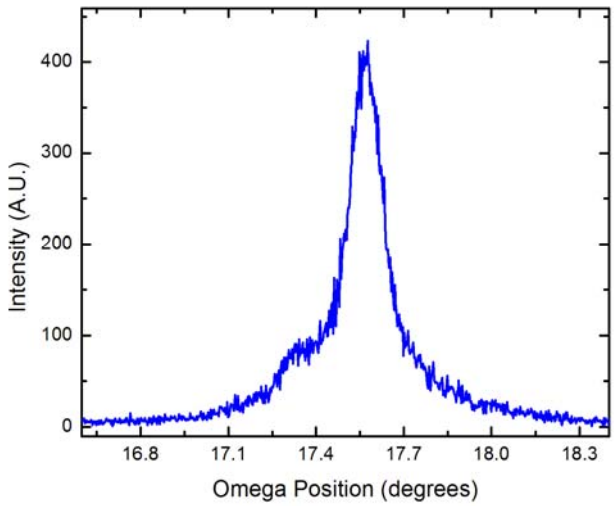

Figure 8.42: XRD rocking curve of AlGaN (002) from the AlGaN/AlN/GaN structure grown on a UID GaN template. The AlGaN peak exhibits a FWHM of ~560 arcsecs.

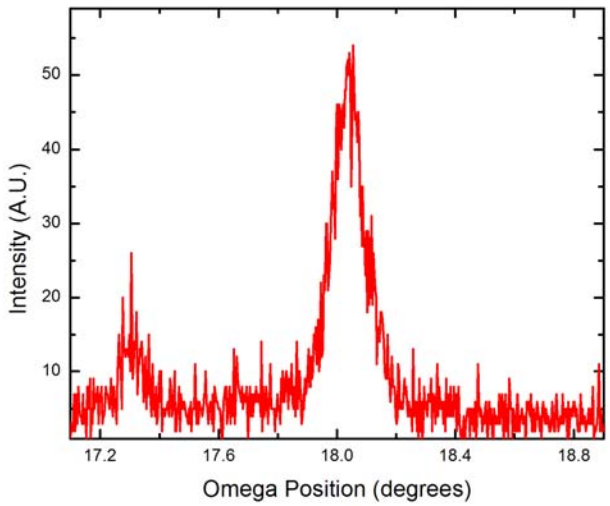

Figure 8.43: XRD rocking curve of AlN (002) from the AlGaN/AlN/GaN structure grown on a UID GaN template. The AlN peak exhibits a FWHM of ~410 arcsecs.

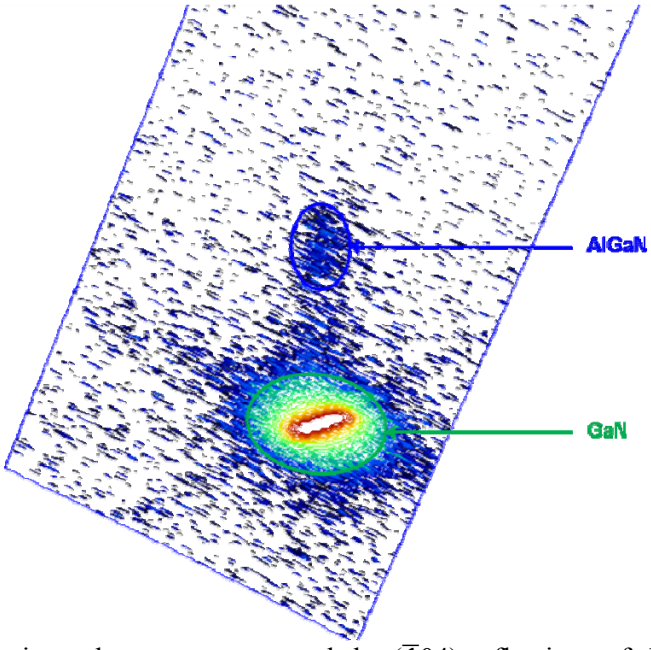

Figure 8.44: XRD reciprocal space map around the ($\bar{1}$04) reflections of the AlGaN/AlN/GaN structure grown on a UID GaN template. The AlGaN layer is fully strained to the underlying GaN as evident by the vertical alignment of the peaks.

Similarly to the previous structures, the AlGaN/AlN/GaN structure was characterized through a C-V measurement. Figure 8.45 shows the charge density versus depth profile calculated from the C-V data. Similarly to the AlGaN/GaN structure, the AlGaN/AlN/GaN structure results in 2DEG formation, yet the low Schottky barrier provided by the Hg contact and the high series resistance due to exaggerated geometry results in a larger measured depletion width.

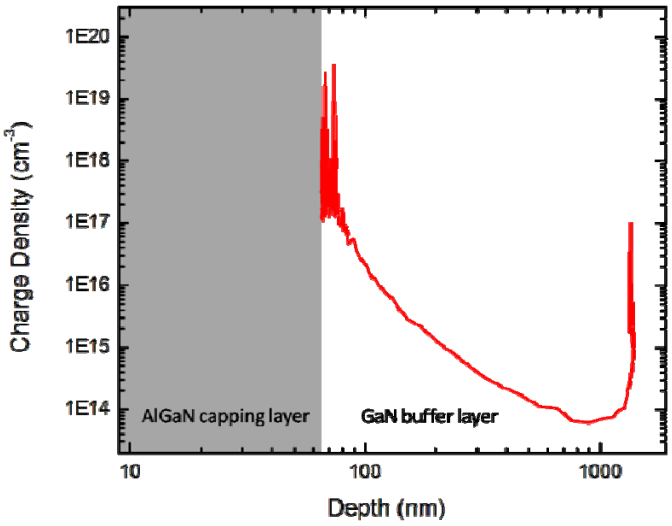

Figure 8.45: Charge density versus depletion width results calculated for an AlGaN/AlN/GaN device structure grown using a high temperature GaN buffer on a UID GaN template.

8.7 Conclusions

In this chapter, a variety of device structures grown by NH_3-MOMBE were investigated as means of forming a 2DEG. These structures included AlGaN/GaN,

AlGaN/AlN/GaN and AlGaN/AlGaN grown on both Si-doped and UID GaN templates. It was determined that AlGaN/GaN and AlGaN/AlN/GaN structures utilizing low temperature GaN buffers were insufficient in forming a 2DEG, which is postulated to be a result of either increased carbon incorporation inherit with lower deposition temperatures or GaN surface degradation resulting from the growth temperature ramp. By implementing a high temperature GaN buffer on Si-doped GaN templates, the first reported formation of a 2DEG in III-Nitride heterostructures grown by NH_3-MOMBE was achieved. In addition to forming a 2DEG, the self-compensating nature of the GaN buffer lead to a free carrier concentration of ~1 x 10^{14} cm^{-3} for the GaN buffer. This illustrates the potential benefit of utilizing the C-doped GaN buffer for reduced current leakage in HEMT devices.

The transfer of the growth parameters to UID GaN templates lead to challenges due to temperature variations. Once solved, successful 2DEG formation was achieved for both AlGaN/GaN and AlGaN/AlN/GaN device structures on UID GaN templates. Electrical characterization of the device structures on the UID templates was not possible as difficulty with achieving ohmic contacts led to inconsistent results. This difficulty in achieving ohmic contacts illustrates the potential difficulties that will need to be addressed in device fabrication. Although these results show potential for the NH_3-MOMBE system to form 2DEGs, there still exist significant challenges that must be overcome to realize NH_3-MOMBE grown HEMTs.

CHAPTER 9: OPTICAL CHARACTERIZATION OF TRAP-RELATED STATES IN CARBON-DOPED GaN GROWN BY AMMONIA-BASED METAL-ORGANIC MOLECULAR BEAM EPITAXY

9.1 Introduction

The results from the previous chapter show the potential of NH_3-MOMBE to produce device structures and subsequent 2DEGs. While the obtainable resistivity of NH_3-MOMBE GaN shows potential for low-leakage buffers, the high levels of incorporated carbon may ultimately negatively affect device performance through the formation of trap states. These carbon-related trap states may be responsible for the complications in 2DEG formation highlighted in Chapter 8. Reports have shown that several C-related trap states exist in GaN, which would adversely affect electrical performance [134, 155]. When the device is biased, the electrons in the 2DEG can become trapped in the C-related trap states, reducing the sheet charge density [156]. To overcome these trap states, determination of the trap densities and their relative energy position inside the material is necessary.

In this chapter, NH_3-MOMBE grown GaN has been characterized by photo-capacitive measurements and photoluminescence. The results of these optical characterization techniques have been utilized to determine the existence of carbon-related trap states in GaN.

9.2 Experimental Setup

All films grown for this chapter were deposited in a custom NH_3-MOMBE growth reactor [54], with a base pressure of ~5 x 10^{-9} Torr. The details regarding sample preparation and substrate cleaning are discussed in Appendix A.1. NH_3 and TEGa were used as the precursors, which were introduced without carrier gases. The choked viscous flow gas delivery system and subsequent gas flow conversions are discussed in Appendix A.2. Herein, all references to source precursors will be presented as flow rates.

For the photoluminescence (PL) measurements, the sample was excited using a continuous wave HeCd (Omnichrom 3056-M-A03, 18 mW, λ = 325 nm) laser. The sample was cooled to 77K using a liquid-nitrogen cooled cryostat and vacuum housing. The emission spectrum of the sample was separated by a spectrometer (Spex 1702) and detected with an equipped photomultiplier tube (PMT) (Products for Research Inc., Model: TE104RF).

For the photo-capacitive measurements, the backside metallization was removed using a hydrofluoric (HF) etch, while the GaN surface was protected with wax. The capacitance was monitored by a Boonton 7200 capacitance meter, while illumination was provided by a Solux MR16 halogen lamp. Figure 9.1 shows the typical emission spectrum of the halogen lamp used in these experiments. Specific wavelengths of the spectrum were isolated using Edmund Optics bandpass filters ranging from 400 – 900 nm, which all exhibit an optical bandwidth FWHM of 10 nm.

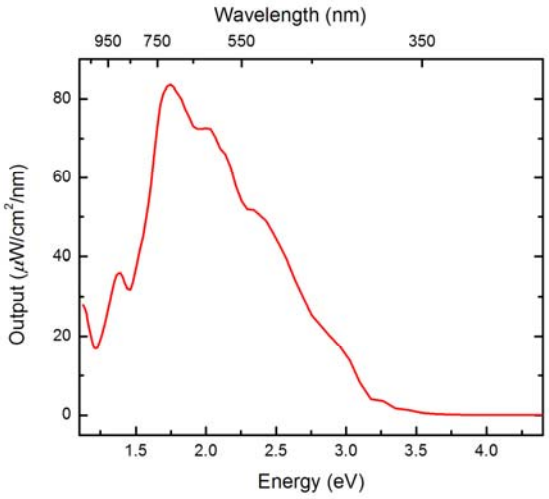

Figure 9.1: Vendor described output spectrum of Solux MR16 halogen lamp used in the photo-capacitive measurements of NH_3-MOMBE grown GaN.

9.3 Photoluminescence Characterization of NH_3-MOMBE GaN

To understand the role of carbon on the formation of trap states in GaN, photoluminescence measurements were conducted to determine the optical transition of the C-related states. Figure 9.2 shows the spectrum obtained from the photoluminescence characterization of a ~500 nm thick GaN film grown at 950 °C with a V/III ratio of ~58. The spectrum exhibits three main transitions, located at ~2.9, 3.0 and 3.45 eV. The transition at 3.45 eV corresponds with the band edge transition associated with GaN, which exhibits a bandgap value of 3.4 eV at 300K. The 0.5 eV increase in the transition value is a result of the measurement temperature, which was 77K to reduce lattice

vibrations and increase measurement accuracy. The remaining transitions located at ~2.9 eV and 3.0 eV have been reported in high resistivity (HR) carbon-doped GaN [55, 57, 133, 135, 156-159], and have been identified as transitions resulting from carbon incorporation. The ~3 eV transition corresponds to a transition between a C_N acceptor (E_V + 0.2 eV) and a C_{Ga} (E_C – 0.2 eV) donor. This indicates that there is sufficient carbon incorporation to compensate the background donor concentration through C_N incorporation as well as sufficient carbon to result in C_{Ga} incorporation. Furthermore, the existence of a transition energy of ~2.8 eV has been detected in both MOCVD and MBE C-doped GaN samples [57, 133, 156], with the magnitude of the transition depending on the magnitude of carbon incorporation. This transition has been postulated to result from a transition between a gallium vacancy (V_{Ga}) and C_{Ga} [133, 156, 160]. This transition at ~2.8 eV is indicative of extremely high carbon doping and only appears when the [C] is much greater than the background n-type dopant concentration. By calculating the ratio between the trap transition intensity and the bandgap intensity, the magnitude of the trap states can be determined. The intensity of the transition at 2.85 eV ($I_{2.85\ eV}$) divided by the bandgap intensity ($I_{3.4\ eV}$) results in a percentage of ~32 %, while $I_{3.0\ eV}$ / $I_{3.4\ eV}$ = ~44 %. These ratios illustrate the strong effect of carbon incorporation on the trap state formation in GaN.

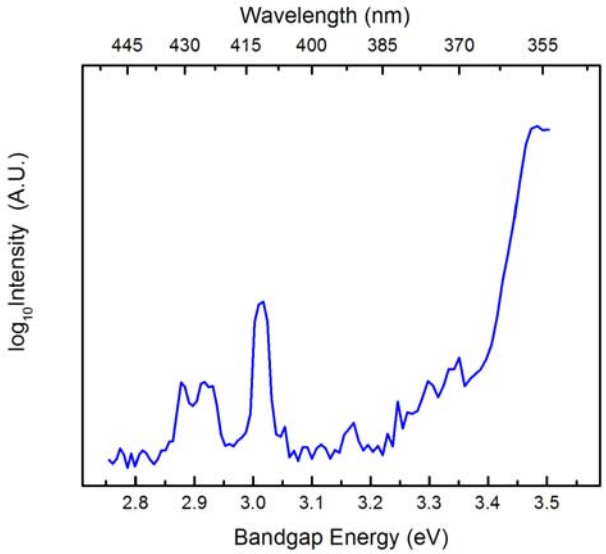

Figure 9.2: Photoluminescence spectrum obtained from NH_3-MOMBE grown GaN at 77K.

9.4 Photo-capacitive Characterization of NH_3-MOMBE GaN

After determining that the carbon contributes to optical transitions, photo-capacitive measurements were conducted to determine the influence of the carbon incorporation on the electrical properties of the material. To investigate the influence of carbon on the trap states present in NH_3-MOMBE grown GaN, two samples were grown. A higher carbon containing GaN film was grown at 770 °C with a supplied V/III ratio of 80.5. Additionally, a separate GaN film was grown at 950 °C with a supplied V/III ratio of 121, which has been shown in Chapter 6 to result in a 5x decrease in carbon incorporation. Each film was characterized through photo-capacitive measurements, with the resulting capacitance variations as a function of excitation wavelength displayed in Figures 9.3 and 9.4. The photo-capacitance variations in both GaN films corresponds to

optical wavelengths above ~2.8 eV and correspond to known defects related to carbon. Although the measured capacitance variation corresponding to the 3.0 eV transition does not explicitly indicate that the 3.0 eV transition is present, the previous PL data shown prove its existence.

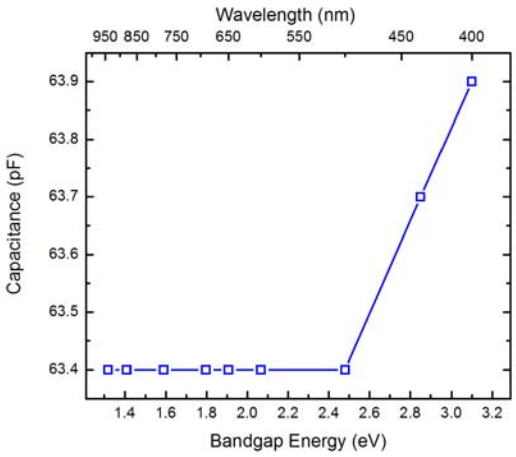

Figure 9.3: Capacitance measurements with varying wavelengths of optical excitation taken from NH_3-MOMBE grown GaN at 770 °C.

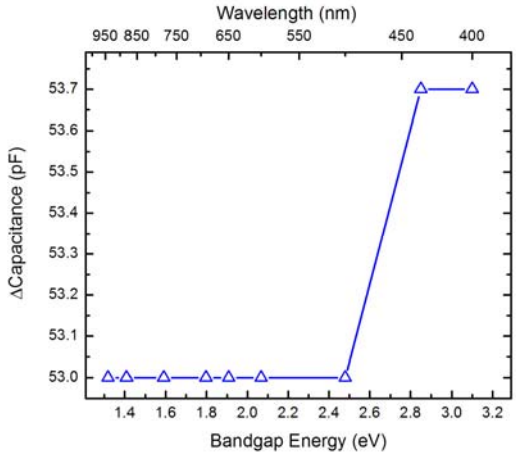

Figure 9.4: Capacitance measurements with varying wavelengths of optical excitation taken from NH_3-MOMBE grown GaN at 950 °C.

These trap states have been reported to result from C incorporation and have been shown to affect the performance of AlGaN/GaN HEMTs [156]. These photo-capacitive results illustrate the effect of C incorporation on the electrical properties of the films. Although the results in Chapter 6 indicate that increased growth temperatures result in lower carbon concentrations, there is no distinguishable variation in the trap densities detected in this study. Therefore, although carbon levels can be decreased, the trap states that are responsible for HEMT performance degradation may not be controllable. These measured values illustrate the difficulties associated with the use of C-doped GaN as an electrically isolating buffer layer. Although the C-doped GaN has been shown to exhibit a resistivity of 10^{12} Ω-cm, the formation of these trap states may ultimately limit its usefulness in electrical devices. Ultimately, the control of the carbon incorporation is paramount for its utilization in device applications.

9.5 Conclusions

The influence of carbon on the properties of GaN grown by NH_3-MOMBE has been investigated by both photo-capacitance and photoluminescence measurements. The results from both characterization techniques indicate that two C-related transitions are present in NH_3-MOMBE GaN. The optical transitions correspond to energies of ~2.85 and 3.0 eV, which have both been reported in literature for intentionally carbon-doped GaN. The transition at 3.0 eV corresponds to a transition between C_{Ga} and C_N while the 2.85 eV energy corresponds to a V_{Ga} to C_{Ga} transition. The trap density at both 3.0 eV

and 2.85 eV showed little to no correlation with the growth temperatures used in this experiment (770 °C and 950 °C). From the PL measurements, $I_{2.85eV}/I_{3.4eV}$ = ~32 % and $I_{3.0eV}/I_{3.4eV}$ = ~44 %, indicating that these transitions are the predominant transitions in NH_3-MOMBE GaN. Additionally, photo-capacitive measurements were conducted illustrating that the incorporated C is electrically active in NH_3-MOMBE grown GaN. These results, combined with literature results, indicate that the carbon incorporation in NH_3-MOMBE GaN poses a significant challenge in the realization of devices and that proper control of the carbon incorporation may ultimately be necessary.

CHAPTER 10: CONCLUSIONS AND FUTURE DIRECTIONS

10.1 Conclusions

This work explores NH_3-MOMBE as a potential candidate for the production of III-Nitride-based HEMTs that utilize a highly carbon-doped GaN buffer to reduced leakage current in the device. The primary results from this work include:

1. NH_3-MOMBE is capable of producing GaN with a crystalline quality limited by the GaN growth template. In addition, GaN surface morphologies suitable for device applications are achievable in this NH_3-MOMBE system.

2. Unlike traditional MBE growth, growth of high quality NH_3-MOMBE GaN is achieved through growth in the N-rich growth regime. The N-rich growth regime is also the preferred growth regime for the realization of planar GaN surface morphologies. Although optimal growth conditions are achieved in N-rich conditions, the growth of GaN by NH_3-MOMBE is extremely sensitive to the NH_3 flow rate, therefore precise control must be maintained.

3. The surface morphology of NH_3-MOMBE films is extremely sensitive to both growth temperature and V/III ratio variations. Minor variations in either parameter can lead to order of magnitude degradations in surface morphology.

4. NH_3-MOMBE can achieve extremely high growth rates exceeding ~4 μm/hr for the growth of GaN and $Al_xGa_{1-x}N$. These improved growth rates over traditional MBE leading to increased system throughput for the growth of III-Nitrides.

5. The growth of $Al_xGa_{1-x}N$ is possible via NH_3-MOMBE, across the entire Al composition range. This system is capable of producing high quality $Al_xGa_{1-x}N$ films with crystalline qualities limited by the GaN growth template. In addition, this NH_3-MOMBE system has demonstrated the ability to consistently obtain targeted $Al_xGa_{1-x}N$ thicknesses and composition, illustrating system repeatability.

6. The growth of AlGaN by NH_3-MOMBE is a highly sensitive growth process because of the interdependent growth parameters. The Al-enhanced pyrolysis of ammonia leads to increased active N, necessitating alteration in growth stoichiometry.

7. N-rich growth of $Al_xGa_{1-x}N$ by NH_3-MOMBE leads to optimal surface morphologies and crystalline qualities. In addition, N-rich growth prevents preferential incorporation of Al over Ga making compositional repeatability easier.

8. Both increased growth temperature and V/III ratio were found to decrease the incorporation of carbon in GaN grown by NH_3-MOMBE. Although carbon levels can be controlled, the concentration of carbon routinely exceeds 10^{20} cm^{-3}.

9. The introduction of atomic hydrogen during the growth of GaN grown by NH_3-MOMBE resulted in minor reductions of carbon incorporation. Significant hydrogen recombination or sufficient atomic hydrogen through ammonia pyrolysis are suspected as the reason for the minor carbon reduction.

10. The first 2DEG produced in an AlGaN/GaN device structure grown by NH_3-MOMBE has been reported. 2DEGs were achieved on both insulating and conductive GaN templates. Although 2DEGs were achieved on UID templates, difficulties in obtaining ohmic contacts limited electrical characterization.

11. Carbon was found to incorporate as substitutionals for N and Ga in GaN grown by NH_3-MOMBE. Additionally, the carbon results in significant V_{Ga}-related trap states in GaN. The incorporation of carbon in GaN grown by NH3-MOBME was also found to be electrically active.

12. Due to the poor mobilites of the 2DEGs obtain in the AlGaN/GaN device structures, further optimization of the growth parameters needs to be completed. The high growth temperatures necessary to reduce carbon incorporation also results in step bunching which negatively affects the 2DEG mobility.

Optimization of the surface morphologies and interface surface roughness needs to be completed in order to improved the electrical characteristics of the 2DEG.

10.2 Future Directions

While this work has produced the conditions necessary to achieve a 2DEG in an NH_3-MOBME environment, there still remain challenges that must be addressed to realize a functioning device. Future work in this area may include:

1. Transfer and optimization of the AlGaN/GaN growth conditions to an insulating substrate. Employing insulating substrates would allow for improved electrical characterization and eventual device fabrication.

2. Investigation of NH_3-MOMBE growth on a non-native substrate, like sapphire or SiC, would reduce operating costs and increase potential device applications. This heteroepitaxial growth would require optimization of nucleation to account for the lattice mismatch. Solving the nucleation issue would allow for realization of electrical devices, while reducing system costs associated with the purchasing of external templates.

3. Optimization of the process conditions for the fabrication of a NH_3-MOBME grown AlGaN/GaN HEMT. Difficulties in process optimization are likely to arise due to the high resistivity (~10^{12} Ω-cm) of the NH_3-MOMBE films.

4. While 2DEGs in NH_3-MOMBE AlGaN/GaN structures have been achieved, the decreased charge density of the 2DEG obtained when deposited on UID GaN templates remains an issue. Modulation doping of the AlGaN/GaN structure may be employed as a means of providing electrons to increase the sheet charge density of the 2DEG.

5. Perhaps the most promising consideration would be to employ the use of metal-organic sources into a traditional MBE environment. This work has shown the potential of achieving extremely resistive GaN buffers, yet the carbon results in additional challenges as a result of trap formation. Combining the metal-organics in MBE would provide a means for highly-resistive GaN films, yet would allow for the deposition of a GaN buffer with traditional effusion cells to eliminate the adverse effects of carbon. The remaining AlGaN capping layer would also be deposited by traditional MBE, allowing for a high mobility 2DEG while maintaining a highly resistive GaN buffer for decreased device current leakage.

APPENDIX A: SUPPLEMENTAL DATA

A.1 Substrate Preparation

The received 2" Lumilog GaN wafers are initially cleaned in a 10 min. piranha solution of H_2SO_4:H_2O_2 (4:1) heated to 90 °C. Following cleaning the wafers are rinsed in de-ionized (DI) water. To promote efficient and uniform heating of the samples, the wafers are backside metalized in a Unifilm multi-wafer DC/RF sputterer. The wafers are metalized with ~2 μm of tantalum, which is deposited at ~150 Å/min. Following metallization, the wafers are covered with Rohm Haas S1313 positive photoresist which is spun on for 30 sec at a speed of 500 revolutions per minute (rpm), before baking for 3 min in a 90 °C oven. The 2" GaN wafers are then diced into 1x1 cm^2 samples for growth. After dicing the wafers are striped of the photoresist using an 1165 photoresist stripper for 3 min, heated to ~60 °C. The samples are then twice immersed in a piranha solution of H_2SO_4:H_2O_2 (4:1) heated to 90 °C for 10 min.

Following cleaning, the substrates are loaded and heated in a custom substrate module [54]. The substrate temperature was monitored by a type C thermocouple positioned approximately 1 mm behind the sample. Once loaded, the samples were initially outgassed in the introductory chamber for 30 min. at 150 °C under cryogenic pumping (1 x 10^{-8} Torr). Once outgassed, the samples are loaded into the growth chamber and annealed at 650 °C for an additional 10 min. while under an NH_3 flow of

~26 sccm. Following a thermal anneal, the samples are brought to growth temperature with a temperature ramp rate of 2 °C/sec while under an NH_3 flow rate of 26 sccm.

A.2 Metal-Organic Precursor Flux Control

Source precursors are delivered individually into the growth chamber via ¼" stainless steel tubing. TEGa, TEAl and Disilane are employed as precursors without the use of carrier gases. TEAl was chosen to maintain an all-ethyl-alkyl growth chemistry to prevent preferential incorporation [162]. These precursors are housed in individual temperature-controlled Lauda RMS6 baths to accurately control their vapor pressures. Additionally, the source delivery lines are independently heated during growth using self-regulating heater cable which is maintained at ~80 °C (~150 °C for TEAl) to prevent condensation of the precursors during delivery. All sources were injected into the growth system from ¼" stainless steel tubes with consistent geometries, making TEGa and TEAl flow rates comparable to NH_3 flow rates.

The flow control of these precursors was done through the closed-loop monitoring of a choked viscous flow delivery system [163], while the flow of NH_3 was controlled by a mass flow controller (MFC). This delivery system monitors and controls a source pressure behind either a 660 or 40 μm leak orifice, which feeds directly to the growth chamber. The source pressures are monitored independently using MKS Bartron capacitance manometers which are positioned upstream of the orifices. A PID control loop monitors the source pressures and adjusts an upstream MKS motor valve accordingly to maintain the appropriate upstream pressure. By controlling this choked upstream pressure, the flow rate of the precursors can be determined through the following equations.

$$Q = C\left(P_{up} - P_{down}\right) \tag{A.1}$$

$$C = 11.6\ {}^{\pi D^2}/_{4} \tag{A.2}$$

In the above equations, Q represents throughput (Torr liters/second), C represents conductance (liters/second), and *D* represents the orifice diameter (centimeters), while P_{up} and P_{down} (in Torr) represent upstream and downstream pressures, respectively. All references to precursor flow rates in this thesis were calculated through the above equations. This delivery system allows for precise precursor flow control over a large dynamic range from ~0.001 – 1 sccm.

APPENDIX B: OPTIMAL GROWTH CONDITIONS

B.1 GaN Optimization

This section describes the optimal growth conditions for GaN at various temperatures. The optimal growth conditions are determined through XRD to determine crystalline quality and through AFM for surface morphology determinations. The GaN films were optimized at a variety of growth temperatures, including 770, 860 and 950 °C. Figure B.1 shows the growth rates for GaN grown with varying growth temperatures and an NH_3 flow rate of 50 sccm. Each growth temperature offers unique benefits with respect to adatom mobility, carbon incorporation, desorption kinetics, etc. The following will describe the optimization of the GaN films at each growth temperature.

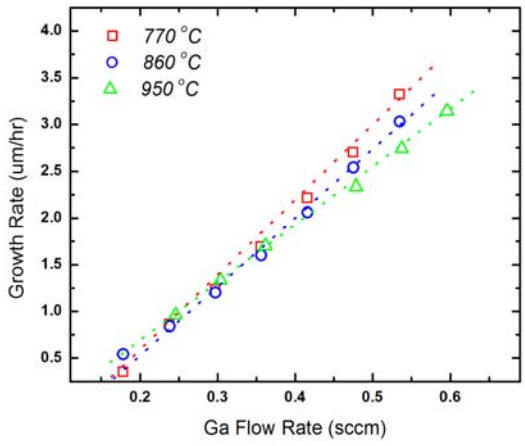

Figure B.1: GaN growth rates at varying growth temperatures. The NH_3 flow rate for all growths was 50 sccm.

B.1.1 GaN Optimization at 770 °C

GaN growth at this reduced growth temperature is not recommended for HEMT devices due to the increased incorporation of carbon, but the reduced growth temperature does offer the benefit of improved surface morphologies for GaN. Figures B.2 and B.3 show the surface morphologies for ~500 and 2000 nm GaN films grown at 770 °C. The samples in the figures were grown at 770 °C, with an NH_3 flow rate of 50 sccm and a TEGa flow rate of 0.295 sccm, resulting in a V/III ratio of ~169.5. The resulting rms roughness values for are ~3.5 nm, and exhibit a decreased value of ~0.5 nm in areas devoid of surface pitting. Additionally, as seen in the inset in Figure B.3, the GaN films grown at 770 °C exhibit atomic steps that indicate step flow growth.

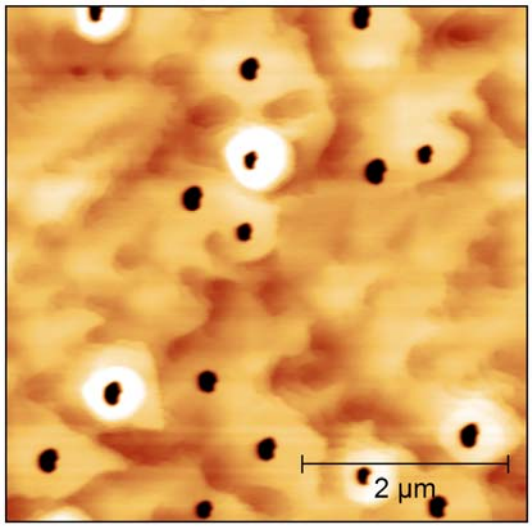

Figure B.2: 5x5 μm AFM scan of ~500 nm GaN sample grown at 770 °C exhibiting an rms roughness value of 3.4 nm. The image z scale is 40 nm.

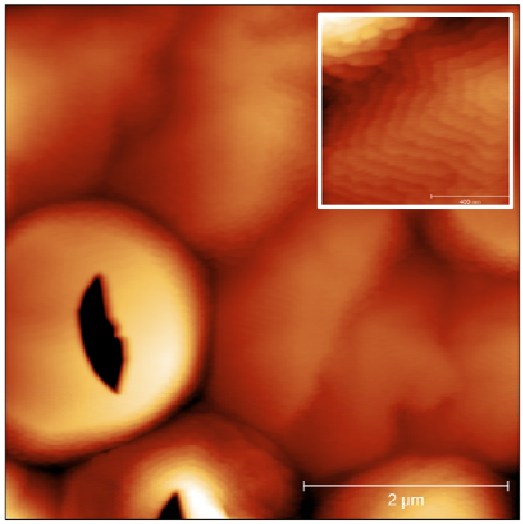

Figure B.3: 5x5 μm AFM scan of ~2 μm GaN sample grown at 770 °C exhibiting atomic steps and a rms roughness value of 3.5 nm. The 1x1 μm inset illustrates the atomic steps and has an rms roughness value of 0.5 nm. The z scales are 40 nm and 10 nm for the 5x5 μm and 1x1 μm scans, respectively

B.1.2 GaN Optimization at 860 °C

By increasing the growth temperature for GaN, surface morphologies are typically improved, although these growth temperatures will results in significant adatom desorption and GaN decomposition. This can be mitigated through the use of an NH_3 overpressure. Figure B.4 illustrates representative surface morphologies obtained with optimized growth conditions at 860 °C. The optimized growth conditions at 860 °C use a TEGa flow rate of 0.413 sccm with an NH_3 flow rate of 50 sccm, resulting in a V/III ratio of ~121. At growth temperatures of 860 °C, the morphology transitions from a pitted surface, to a surface exhibiting macroscopic steps with step heights of ~2 nm. These steps have been observed in work by Feenstra *et al.* and are attributed to the influence of

atomic hydrogen on the surface lifetime of nitrogen [139]. The increased growth temperature provides increased pyrolysis of NH_3, resulting in atomic hydrogen that alters the growth kinetics of GaN. These macroscopic steps may potentially complicate 2DEG formation in AlGaN/GaN HEMTs grown with an 860 °C GaN buffer since the increased step size may result in significant scattering of the 2DEG.

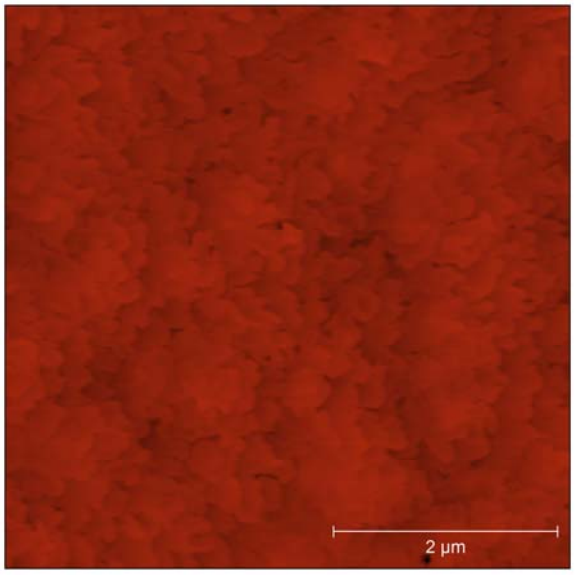

Figure B.4: 5x5 μm AFM scan of ~500 nm GaN sample grown at 860 °C exhibiting and rms roughness value of ~0.88 nm. The image z scale is 40 nm.

B.1.3 GaN Optimization at 950 °C

With the morphological improvements realized through the increase of growth temperature from 770 °C to 860 °C, further experiments involved the growth of GaN at 950 °C. In addition to improved morphology, increased growth temperatures would provide a means for decreased carbon incorporation in GaN. Figure B.5 shows the optimized surface morphology of GaN growth at 950 °C, which exhibits an rms roughness value of ~0.85 nm. The optimized growth conditions at 950 °C used TEGa flow rates of 0.354 sccm and a NH_3 flow rate of 25 sccm, resulting in a V/III ratio of ~70.6. Similarly to the GaN films grown at 850 °C, films grown at 950 °C exhibit ~2 nm steps due to the increased production of H during the pyrolysis of NH_3. As determined in Chapter 6, carbon incorporation is lowest for GaN films grown at 950 °C. Additionally, the C-V results from Chapter 9 showed that 2DEG formation in AlGaN/GaN structures was only obtainable for structures which utilized a GaN buffer growth temperature of 950 °C.

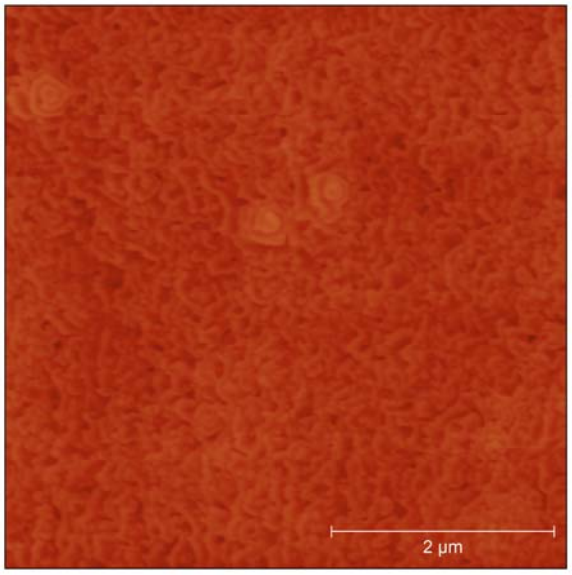

Figure B.5: 5x5 μm AFM scan of ~500 nm GaN sample grown at 950 °C exhibiting an rms roughness value of ~0.85 nm. The image z scale is 40 nm.

Table B.1: Optimized growth conditions for the growth of GaN at various growth temperatures.

T_{growth}	*TEGa flow (sccm)*	NH_3 *flow (sccm)*	*V/III Ratio*	*rms roughness*
770 °C	0.3	50	170	3.4 nm
860 °C	0.41	50	121	0.9 nm
950 °C	0.35	25	70.6	0.9 nm

B.1.4 GaN Summary

GaN growth conditions at various temperatures have been optimized to provide optimal surface morphologies. Table B.1 shows the optimized growth conditions determined for GaN at various growth temperatures. No noticeable influence of growth temperature on the crystalline quality of GaN was detected by XRD, indicating the GaN films at all growth temperatures mimicked the crystalline quality of the GaN template. GaN films grown at 770 °C exhibited surface pitting with atomic steps, while samples grown above 860 °C exhibited ~2 nm steps with improved rms roughness values. Combined with the previous results from Chapters 6 and 9, the optimal growth conditions used primarily for this work were the conditions at 950 °C.

B.2 AlGaN Optimization

The ternary AlGaN was optimized at various temperatures and growth conditions to determine the optimal conditions necessary for the utilization of AlGaN in transistor structures. Because of the low vapor pressure of TEAl, heating of the source bath is necessary to achieve a sufficient vapor pressure. Typical bath temperatures for TEAl are ~55 °C. At these temperatures, subsequent heating of the vapor delivery system is crucial to prevent condensation of the material in the delivery lines, thereby increasing flux repeatability and growth consistency.

B.2.1 AlGaN Optimization at 870 °C

As discussed in Chapter 3, AlGaN films spanning the entire range of Al compositions were grown at 870 °C. All samples grown at 870 °C have an NH_3 flow rate of 25 sccm and a constant total metal flow rate of 0.017 sccm, with only the TEAl/TEGa ratio varied. The increased pyrolysis of NH_3 in the presence of Al led to excessive N-rich growth conditions, which resulted in significant surface pitting as seen in Figure B.6. Although surface pitting existed for AlGaN samples grown at 870 °C, step flow growth was achieved, as evident by the atomic steps seen in Figure B.7. The smoothness of the sample is evident by its rms roughness value of ~0.9 nm, which includes contributions from the surface pits. Further information regarding the strain and crystalline quality of AlGaN films grown at 870 °C can be found in Chapter 3.

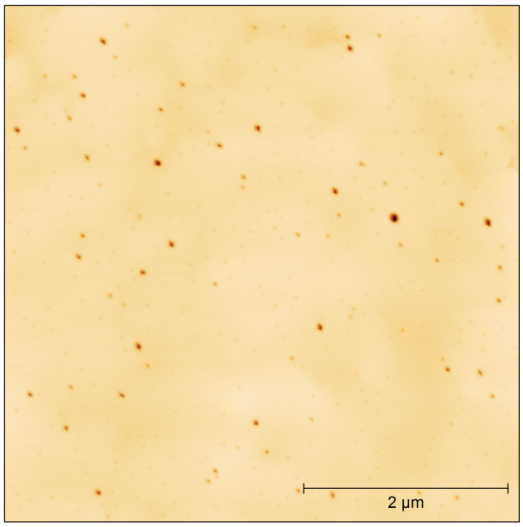

Figure B.6: 5x5 μm AFM scan of $Al_{0.2}Ga_{0.8}N$ sample grown at 870 °C exhibiting significant surface pitting because of the increased pyrolysis of NH_3. The image z scale if 40 nm.

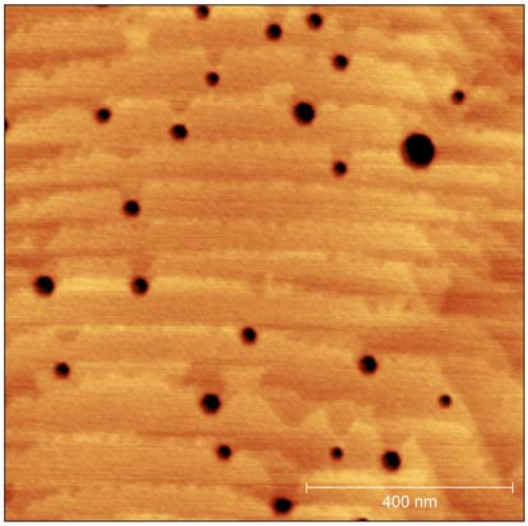

Figure B.7: 1x1 μm AFM scan of $Al_{0.2}Ga_{0.8}N$ sample grown at 870 °C exhibiting atomic steps. The image z scale is 3 nm.

B.2.2 AlGaN Optimization at 950 °C

In an attempt to improve the surface morphology and crystalline quality of AlGaN films with increased Al contents, an increased growth temperature of 950 °C was attempted. As described in Chapter 5, the growth of AlGaN at an increased growth temperature of 950 °C resulted in several improvements over 870 °C growth. Namely, the existence of Pendellösung fringes in XRD 2θ-ω scans indicates that the interface is abrupt and that the film is planar. Figure B.8 shows a typical surface morphology for AlGaN obtained at growth temperatures of 950 °C that exhibits an rms roughness value of ~1 nm. Figure B.9 shows an AFM scan with a reduced scan size, highlighting the atomic steps that are obtainable at 950 °C. The optimized growth conditions for this

sample include a TEGa flow rate of 0.118 sccm, a TEAl flow rate of 0.71 sccm and an NH_3 flow rate of 10 sccm, resulting in a V/III ratio of ~53.

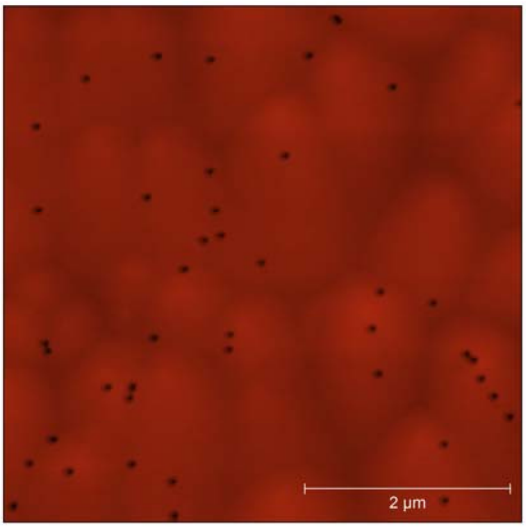

Figure B.8: 5x5 μm AFM scan of $Al_{0.25}Ga_{0.75}N$ grown at 950 °C exhibiting an rms roughness value of ~1 nm. The image z scale is 40 nm.

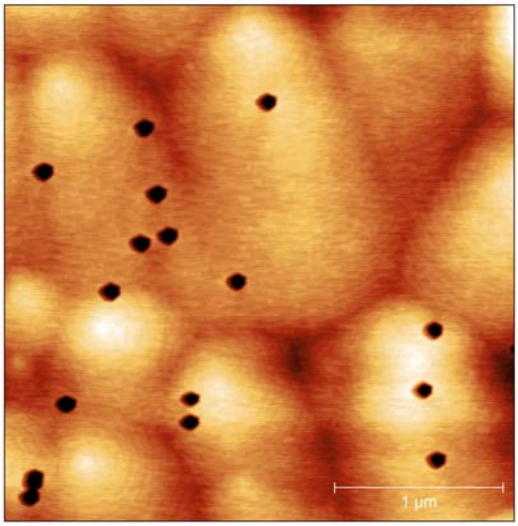

Figure B.9: 3x3 μm AFM scan of $Al_{0.25}Ga_{0.75}N$ grown at 950 °C illustrating the existence of atomic steps. The image z scale is 4.5 nm

B.2.3 AlGaN Summary

Table B.2 illustrates the optimized growth conditions for $Al_{0.25}Ga_{0.75}N$ at various growth temperatures. Although both growth temperatures exhibit similar rms roughness values, the increased growth temperature of 950 °C results in abrupt interface control, as indicated by Pendellösung fringes in the XRD 2θ-ω scans. The AlGaN capping layers for the AlGaN/GaN device structures grown in this work utilized AlGaN films grown at 950 °C. Using the AlGaN capping layers grown at 950 °C, successful 2DEG formation was achieved in both AlGaN/GaN and AlGaN/AlN/GaN device structures.

Table B.2: Optimized growth conditions for the growth of $Al_{0.25}Ga_{0.75}N$ grown at both 870 and 950 °C.

T_{growth}	TEGa (sccm)	TEAl (sccm)	NH_3 (sccm)	V/III Ratio	rms roughness
870 °C	0.118	0.047	26	157	0.9 nm
950 °C	0.118	0.071	10	53	1 nm

APPENDIX C: GROWTH OF AlGaN/GaN STRUCTURE BY PAMBE

With initial difficulties obtaining a 2DEG in NH_3-MOMBE grown AlGaN/GaN device structures, an AlGaN/GaN device structure was grown by MBE to ensure proper epitaxial device considerations were understood. The structure was grown in a Riber 32 MBE chamber equipped with standard effusion cells for aluminum and gallium. Active nitrogen was supplied using a Veeco Unibulb plasma source, operated at 350 W with an N_2 flow rate of 1.3 sccm. Films were grown on c-plane sapphire which was backside metalized with ~2 μm Ta to promote uniform and efficient heating. The substrates were cleaned using the procedures described in Appendix A.

Following a 30 min. outgassing in the introductory chamber at a temperature of 300 °C, the samples were loaded into the growth chamber and underwent a 30 min. 350 °C nitridation under an N flow rate of 1.3 sccm. After nitridation, a 10 min. (~ 135 nm) AlN buffer layer was deposited at a growth temperature of 700 °C with an Al flux of 4.9 x 10^{-7} Torr. This buffer layer was deposited using a metal-modulated epitaxy (MME) technique developed at Georgia Tech by Burnham *et al.* [9, 164, 165]. The Al shutter was modulated during deposition with a modulation scheme of 10 seconds open, followed by 10 seconds closed. Following the buffer deposition, a ~750 nm GaN layer was deposited with a Ga flux of 7.1 x 10^{-7} Torr and a shutter modulation scheme of 10 seconds open, 10 seconds closed. The GaN layer was capped with ~30 nm AlGaN film grown with a Ga flux of 7.1 x 10^{-7} Torr and Al flux of 2.8 x 10^{-7} Torr with a shutter modulation scheme of 5 seconds open, 10 seconds close. The resulting device structure

was characterized by C-V, with the results plotted in Figure C.1, and the converted data using Equation 8.1 and 8.2 is plotted in Figure C.2. As seen in Figure C.2, the charge depth correlates with the expected AlGaN layer thickness, with a maximum charge density of ~10^{20} atoms/cm^3.

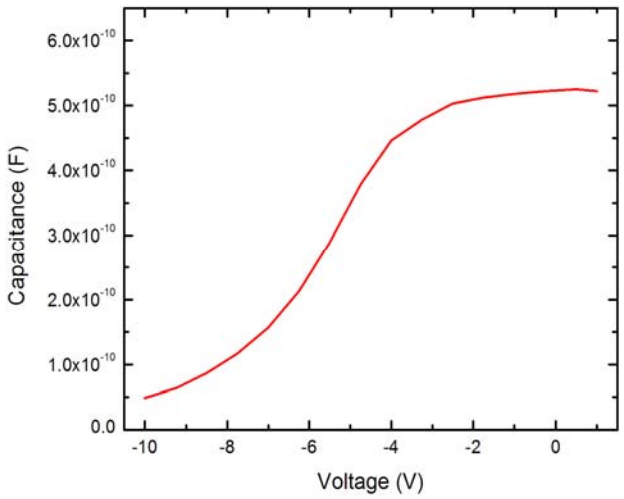

Figure C.1: C-V plot recorded for MBE-grown AlGaN/GaN device structure.

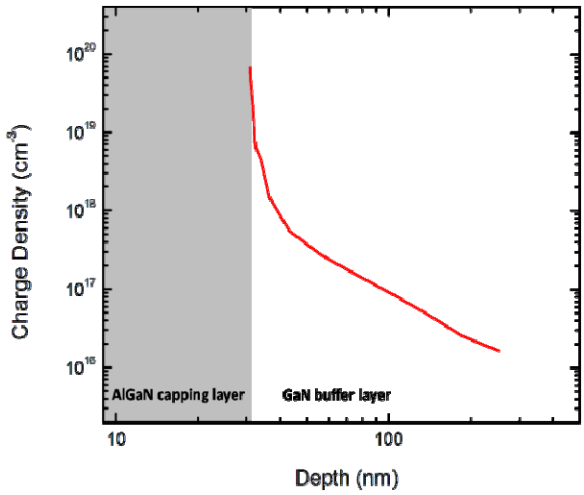

Figure C.2: Charge density versus depletion width of MBE-grown AlGaN/GaN device structure

After determining the existence of a 2DEG in the AlGaN/GaN device structure, indium was deposited onto the sample surface to facilitate electrical characterization. Hall measurements were conducted with a $\mu_{2DEG} \sim 715$ cm^2/V s, and a $N_S = 1.8 \times 10^{13}$ cm^{-3}.

REFERENCES

[1] H. M. Manasevit, "Single-cyrstal gallium arsenide on insulating substrates," *Appl. Phys. Lett.* **12**, 156 (1968).

[2] D. K. Gaskill, N. Bottka, and M. C. Lin, "OMVPE of GaN and AlN films by metal alkyls and hydrazine," *J. Cryst. Growth* **77**, 418 (1986).

[3] S. Miyoshi, K. Onabe, N. Ohkouchi, H. Yaguchi, R. Ito, S. Fukatsu, and Y. Shiraki, "MOVPE growth of cubic GaN and GaAs using dimethylhydrazine," *J. Cryst. Growth* **124**, 439 (1992).

[4] M. Losurdo, P. Capezzuto, and G. Bruno, "Remote plasma MOCVD growth and processing of GaN: A study by real time ellipsometry," *Phys. Stat. Sol. A* **176**, 733 (1999).

[5] W. T. Tsang, "Chemical Beam Epitaxy of GaInAs/InP Quantum Wells and Heterostructure Devices," *J. Cryst. Growth* **81**, 261 (1987).

[6] W. T. Tsang, "From Chemical Vapor Epitaxy to Chemical Beam Epitaxy," *J. Cryst. Growth* **95**, 121 (1989).

[7] A. Y. Cho, "Morphology of epitaxial growth of GaAs by a molecular beam method: The observation of surface structures," *J. Appl. Phys.* **41**, 2780 (1970).

[8] E. Trybus, W. A. Doolittle, M. Moseley, W. Henderson, D. Billingsley, G. Namkoong, and D. C. Look, "Extremely high hole concentrations in c-plane GaN," *Phys. Stat. Sol. C* ***6***, 5788 (2008).

[9] S. D. Burnham, G. Namkoong, D. C. Look, B. Clafin, and W. A. Doolittle, "Reproducible increased Mg incorporation and large hole concentrations in GaN using metal modulated epitaxy," *J. Appl. Phys.* **104**, 1 (2008).

[10] N. Grandjean, J. Massies, P. Vennéguès, M. Leroux, F. Demangeot, M. Renucci, and J. Frandon, "Molecular-beam epitaxy of gallium nitride on (0001) sapphire substrates using ammonia," *J. Appl. Phys.* **83**, 1379 (1998).

[11] Z. Yang, L. K. Li, and W. I. Wang, "GaN grown by molecular beam epitaxy at high growth rates using ammonia as the nitrogen source," *Appl. Phys. Lett.* **87**, 1686 (1995).

[12] M. Henini, "Molecular beam epitaxy: from research to manufacturing," *Thin Solid Films* **306**, 331 (1997).

[13] N. Vodjdani, A. Lemarchand, and H. Paradan, "Parametric Studies of GaAs Growth by Metalorganic Molecular-Beam Epitaxy," *J. Phys. I* **43**, 339 (1982).

[14] T. N. Oder, K. H. Kim, J. Y. Lin, and H. X. Jiang, "III-nitride blue and ultraviolet photonic crystal light emitting diodes," *Appl. Phys. Lett.* **84**, 466 (2004).

[15] M. Razeghi, and A. Rogalski, "Semiconductor ultraviolet detectors," *J. Appl. Phys.* **79**, 7433 (1996).

[16] H. Xing, S. Keller, Y. F. Yu, L. McCarthy, I. P. Smorchkova, D. Buttari, R. Coffie, D. S. Green, G. Parish, S. Heikman, L. Shen, N. Zhang, J. J. Xu, B. P. Keller, S. P. DenBaars, and U. K. Mishra, "Gallium nitride based transistors," *J. Phys.: Condens. Matter* **13**, 7139 (2001).

[17] W. C. Johnson, and J. B. Parsons, "Nitrogen Compounds of Gallium. I, II," *J. Phys. Chem.* **36**, 2588 (1932).

[18] H. Ott, "The grids of aluminium nitride," *Z. Phys. A: Hadrons Nucl.* **22**, 201 (1924).

[19] R. Juza, and H. Hahn, "Crystal structures of Cu_3N, GaN and InN -- Metallic amides and metallic nitrides," *Z. Anorg. Allg. Chem.* **239**, 282 (1938).

[20] L. M. Tolbert, B. Ozpineci, S. K. Islam, and M. S. Chinthavali, "Wide bandgap semiconductors for utility applications," *Proceedings of the Seventh IASTED International Multi-Conference*, Palm Springs, CA (ACTA, Anaheim, 2003) 317.

[21] B. Monemar, G. Pozina, "Group III-nitride based hetero and quantum structures," *Prog. Quantum Electron.* **24**, 290 (2000).

[22] F. Chen, A. N. Cartwright, H. Lu and W. J. Schaff, "Hole transport and carrier lifetime in InN epilayers," *Appl. Phys. Lett.* **87**, 212104-1 (2005).

[23] H. Nakayama, P. Hacke, M. R. H. Khan, T. Detchprohm, T. D. Kazumasa, K. Hiramatsu, and N. Sawaki, "Electrical transport properties of p-GaN," *Jpn. J. Appl. Phys., Part 2* **35**, L282 (1996).

[24] S. Krukowski, A. Witek, J. Adamczyk, J. Jun, M. Bockowski, I. Grzegory, B. Lucznik, G. Nowak, M. Wróblewski, A. Presz, S. Gierlotka, S. Stelmach, B. Palosz, S. Porowski and P. Zinn, "Thermal properties of indium nitride," *J. Phys. Chem. Sol.* **59**, 289 (1998).

[25] Universität Ulm Institut für Optoelektronik, *http://www.opto.e-technik.uni-ulm.de*, Accessed 2009.

[26] S. C. Jain, M. Willander, J. Narayan, and R. V. Overstraeten, "III-nitrides: Growth, characterization, and properties," *J. Appl. Phys.* **87**, 965 (2000).

[27] O. Katz, B. Meyler, U. Tisch, and J. Salzman, "Determination of Band-Gap Bowing for $Al_xGa_{1-x}N$ Alloys," *Phys. Stat. Sol. A* **188**, 789 (2001).

[28] J. Wu, W. Walukiewicz, K. M. Yu, J. W. Ager III, E. E. Haller, H. Lu, and W. J. Schaff, "Narrow bandgap group III-nitride alloys," *Phys. Stat. Sol. B* **240**, 412 (2003).

[29] J. E. Ayers, *Heteroepitaxy of Semiconductors: Theory, Growth and Characterization*, Boca Raton: CRC Press, 2007.

[30] O. Ambacher, B. Foutz, J. Smart, J. R. Shealy, N. G. Weimann, K. Chu, M. Murphy, A. J. Sierakowski, W. J. Schaff, and L. F. Eastman, "Two dimensional electron gases induced by spontaneous and piezoelectric polarization in undoped and doped AlGaN/GaN heterostructures," *J. Appl. Phys.* **87**, 334 (2000).

[31] R. Quay, *Gallium Nitride Electronics*, Berlin: Springer, 2008.

[32] O. Ambacher, "Growth and applications of group III-nitrides," *J. Phys. D: Appl. Phys.* **31**, 2653 (1998).

[33] S. Strite, and H. Morkoç, "GaN, AlN, and InN: A review," *J. Vac. Sci. Technol. B* **10**, 1237 (1992).

[34] D. Huang, P. Visconti, K. M. Jones, M. A. Reshchikov, F. Yun, A. A. Baski, T. King, and H. Morkoç, "Dependence of GaN polarity on the parameters of the buffer layer grown by molecular beam epitaxy," *Appl. Phys. Lett.* **78**, 4145 (2001).

[35] M. Sumiya, and S. Fuke, "Review of polarity determination and control of GaN," *MRS Internet J. Nitride Semicond. Res.* **9**, 1 (2004).

[36] M. Leroux, N. Grandjean, M. Laugt, J. Massies, B. Gil, P. Lefebvre, and P. Bigenwald, "Quantum confined Stark effect due to built-in internal polarization fields in (Al,Ga)N/GaN quantum wells," *Phys. Rev. B: Condens. Matter* **58**, (1998).

[37] I. Akasaki, "Key inventions in the history of nitride-based blue LED and LD," *J. Cryst. Growth* **300**, 2 (2000).

[38] H. Amano, M. Kito, K. Hiramatsu, and I. Akasaki, "P-type conduction in Mg-doped GaN treated with low-energy electron beam irradiation (LEEBI)," *Jpn. J. Appl. Phys.* **28**, L2112 (1989).

[39] H. Amano, N. Sawaki, I. Akasaki, and Y. Toyodo, "Metalorganic vapor phase epitaxial growth of high quality GaN film using an AlN buffer layer," *Appl. Phys. Lett.* **48**, 353 (1986).

[40] X. Wang, C. Wang, G. Hu, J. Wang, and J. Li, "Room temperature mobility above 2100 cm^2/Vs in $Al_{0.3}Ga_{0.7}N/AlN/GaN$ heterostructures grown on sapphire substrates by MOCVD," *Phys. Stat. Sol. C* **3**, 607 (2006).

[41] M. A. Khan, J. N. Kuznia, D. T. Olson, W. J. Schaff, J. W. Burm, and W. S. Shur, "Mircowave performance of a 0.25 μm AlGaN/GaN heterostructure field effect transistor," *Appl. Phys. Lett.* **65**, 1121 (1994).

[42] Y. F. Yu, M. Moore, A. Saxler, T. Wisleder, and P. Parikh, "40-W/mm double field-plated GaN HEMTs," *Device Research Conference (IEEE Cat. No. 06TH8896)* 151 (2006).

[43] J. W. Chung, W. E. Hoke, E. M. Chumbes, and T. Palacios, "AlGaN/GaN HEMT with 300 GHz f_{max}," *IEEE Electron. Device Lett.* **31**, 195 (2010).

[44] A. A. Aquino, and T. S. Jones, "A comparative study of the adsorption and thermal decomposition of triethylgallium and trimethylgallium at GaAs(100) surfaces studied by electron energy loss spectroscopy," *Appl. Surf. Sci* **104**, 304 (1996).

[45] A. C. Jones, "New metal-organic precursors for growth of GaAs and $Al_xGa_{1-x}As$ by chemical beam epitaxy," *Mater. Sci. Eng., B* **17**, 1 (1993).

[46] A. Robertson, T. H. Chiu, W. T. Tsang, and J. E. Cunningham, "A model for the surface chemical kinetics of GaAs deposition by chemical-beam epitaxy," *J. Appl. Phys.* **84**, 877 (1998).

[47] V. M. Donnelly, and J. A. McCaulley, "Products of thermal decomposition of triethylgallium and trimethylgallium adsorbed on Ga-stabilized GaAs(100)," *Surf. Sci.* **238**, 34 (1990).

[48] N. I. Buchan, and M. L. Yu, "ß-Hydride elimination reaction of triethylgallium on GaAs(100) surfaces," *Surf. Sci.* **280**, 383 (1993).

[49] T. F. Kuech, and J. M. Redwing, "Carbon doping in metalorganic vapor phase epitaxy," *J. Cryst. Growth* **145**, 382 (1944).

[50] D. A. Bohling, G. T. Muhr, C. R. Abernathy, A. S. Jordan, S. J. Pearton, and W. S. Hobson, "The search for all-hydride MOMBE: examination of trimethylamine alane, trimethylamine gallane, and arsine," *J. Cryst. Growth* **107**, 1068 (1991).

[51] P. A. Lane, T. Martin, R. W. Freer, P. D. J. Calcott, C. R. Whitehouse, A. C. Jones, and S. Rushworth, "Tri-isopropyl gallium: A very promising precursor for chemical beam epitaxy," *Appl. Phys. Lett.* **61**, 285 (1992).

[52] C. R. Abernathy, P. W. Wisk, A. C. Jones, and S. A. Rushworth, "Comparison of triethylgallium and tri-isobutylgallium for growth of GaAs and AlGaAs by metalorganic molecular beam epitaxy," *Appl. Phys. Lett.* **61**, 180 (1992).

[53] C. R. Abernathy, "Growth of III-V materials by metalorganic molecular-beam epitaxy," *J. Vac. Sci. Technol. A* **11**, 869 (1993).

[54] D. Pritchett, W. Henderson, S. D. Burnham, and W. A. Doolittle, "Influence of growth conditions and surface reaction byproducts on GaN grown via metal organic molecular beam epitaxy: Toward an understanding of surface reaction chemistry," *J. Electron. Mater.* **35**, 562 (2006).

[55] C. H. Seager, A. F. Wright, J. Yu, and W. Götz, "Role of carbon in GaN," *J. Appl. Phys.* **92**, 6553 (2002).

[56] A. F. Wright, "Substitutional and interstitial carbon in wurtzite GaN," *J. Appl. Phys.* **92**, 2575 (2002).

[57] D. S. Green, U. K. Mishra, and J. S. Speck, "Carbon doping of GaN with CBr_4 in radio-frequency plasma-assisted molecular beam epitaxy," *J. Appl. Phys.* **95**, 8456 (2004).

[58] C. G. Van de Walle, C. Stampfl, and J. Neugebauer, "Theory of doping and defects in III-V nitrides," *J. Cryst. Growth* **189**, 505 (1998).

[59] A. J. Ptak, T. H. Myers, L. T. Romano, C. G. Van de Walle, and J. E. Northrup, "Magnesium incorporation in GaN grown by molecular-beam epitaxy," *Appl. Phys. Lett.* **78**, 285 (2008).

[60] H. Tang, J. B. Webb, J. A. Bardwell, S. Raymond, J. Salzman, and C. Uzan-Saguy, "Properties of carbon-doped GaN," *Appl. Phys. Lett.* **78**, 757 (2001).

[61] S. Haffouz, H. Tang, S. Rolfe, and J. A. Bardwell, "Growth of crack-free, carbon-doped GaN and AlGaN/GaN high electron mobility transistor structures on Si (111) substrates by ammonia molecular beam epitaxy," *Appl. Phys. Lett.* **88**, 252114-1 (2006).

[62] S. M. Hubbard, G. Zhao, D. Pavlidis, W. Sutton, and E. Cho, "High-resistivity GaN buffer templates and their optimization for GaN-based HEMTs," *J. Cryst. Growth* **284**, 297 (2005).

[63] S. Heikman, S. Keller, S. P. DenBaars, and U. K. Mishra, "Growth of Fe-doped semi-insulating GaN by metalorganic chemical vapor deposition," *Appl. Phys. Lett.* **81**, 439 (2002).

[64] J. B. Webb, H. Tang, S. Rolfe, and J. A. Bardwell, "Semi-insulating C-dope GaN and high-mobility AlGaN/GaN heterostructures grown by ammonia molecular beam epitaxy," *Appl. Phys. Lett.* **75**, 953 (1999).

[65] S. Haffouz, H. Tang, J. A. Bardwell, E. M. Hsu, J. B. Webb, and S. Rolfe, "AlGaN/GaN field effect transistors with C-doped GaN buffer layer as an electrical isolation template grown by molecular beam epitaxy," *Solid-State Electron.* **49**, 802 (2005).

[66] H. Tang, J. b. WEbb, J. A. Bardwell, S. Rolfe, and T. MacElwee, "Reproducibility of growing AlGaN/GaN high-electron-mobility-transistor heterostructures by molecular-beam epitaxy," *Solid-State Electron.* **44**, 2177 (2000).

[67] D. F. Storm, D. S. Katzer, S. C. Binari, E. R. Glaser, B. N. Shanabrok, and J. A. Roussos, "Reduction of buffer layer conduction near plasma-assisted molecular-beam epitaxy grown GaN/AlN interfaces by beryllium doping," *Appl. Phys. Lett.* **81**, 3819 (2002).

[68] D. Pritchett, Ph.D. Thesis, *Novel III-nitride growth by ultraviolet radiation assisted metal organic molecular beam epitaxy*, Georgia Institute of Technology, 2009.

[69] Y. C. Choi, M. Pophristic, B. Peres, H. -Y. Cha, M. G. Spencer, and L. F. Eastman, "High breakdown voltage C-doped GaN-on-sapphire HFETs with a low specific on-resistance," *Semicond. Sci. Technol.* **22**, 517 (2007).

[70] Y. Cao, and D. Jena, "High-mobility window for two-dimensional electron gases at ultrathin AlN/GaN heterojunctions," *Appl. Phys. Lett.* **90**, 2112 (2007).

[71] Y. -F. Wu, B. P. Keller, S. Keller, D. Kapolnek, S. P. Denbaars, and U. K. Mishra, "Measured microwave power performance of AlGaN/GaN MODFET," *IEEE Electron. Device Lett.* **17**, 455 (1996).

[72] L. Shen, S. Heikman, B. Moran, R. Coffie, N. -Q. Zhang, D. Buttari, I. P. Smorchkova, S. Keller, S. P. DenBaars, and U. K. Mishra, "AlGaN/AlN/GaN high-power microwave HEMT," *IEEE Electron. Device Lett.* **22**, 457 (2001).

[73] T. Nanjo, M. Takeuchi, M. Suita, Y. Abe, T. Oishi, Y. Tokuda, and Y. Aoyagi, "First operation of AlGaN channel high electron mobility transistors," *Appl. Phys. Express* **1**, 011101 (2008).

[74] M. A. Khan, M. S. Shurt, Q. C. Chen, and J. N. Kuznia, "Current/voltage characteristic collapse in AlGaN/GaN heterostructure insulated gate field effect transistors at high drain bias," *Electron. Lett.* **30**, 2174 (1994).

[75] S. C. Binari, K. Ikossi, J. A. Roussos, W. Kruppa, D. Park, H. B. Dietrich, D. D. Koleske, A. E. Wickenden, and R. L. Henry, "Trapping effects and microwave power performance in AlGaN/GaN HEMTs," *IEEE Trans. Electron. Devices* **48**, 465 (2001).

[76] X. L. Wang, T. S. Chen, H. L. Xiao, J. Tang, J. X. Ran, M. L. Zhang, C. Feng, Q. F. Hou, M. Wei, L. J. Jiang, J. M. Li, and Z. G. Wang, "An internally-matched GaN HEMTs device with 45.2 W at 8 GHz for X-band application," *Solid-State Electron.* **53**, 332 (2009).

[77] T. J. Anderson, M. J. Tadjer, M. A. Mastro, J. K. Hite, K. D. Hobbart, C. R. Eddy, and F. J. Kub, "An AlN/Ultrathin AlGaN/GaN HEMT structure for enhancement-mode operation using selective etching," *IEEE Electron. Device Lett.* **30**, 1251 (2009).

[78] M. H. Wong, Y. Pei, J. S. Speck, and U. K. Mishra, "High power N-face GaN high electron mobility transistors grown by molecular beam epitaxy with optimization of AlN interlayer," *Appl. Phys. Lett.* **94**, 2103 (2009).

[79] B. Luo, R. Mehandru, J. Kim, F. Ren, B. P. Gila, A. H. Onstine, C. R. Abernathy, S. J. Pearton, R. Fitch, J. Gillespie, T. Jenkins, J. Sewell, D. Via, A. Cresp, and Y. Irokawa, "Comparison of surface passivation films for reduction of current collapse in AlGaN/GaN high electron mobility transistors," *J. Electrochem. Soc.* **149**, G613 (2002).

[80] J. K. Gillespie, R. C. Fitch, J. Sewell, R. Dettmer, G. D. Via, A. Crespo, T. J. Jenkins, B. Luo, R. Mehandru, J. Kim, F. Ren, B. P. Gila, A. H. Onstine, C. R. Abernathy, and S. J. Pearton, "Effects of Sc_2O_3 and MgO passivation layers on the output power of AlGaN/GaN HEMTs," *IEEE Electron. Device Lett.* **23**, 505 (2002).

[81] M. -W. Ha, Y. -H. Choi, J. Lim, and M. -K. Han, "SiO_2 passivation effects on the leakage current in AlGaN/GaN high-electron-mobility transistors employing additional schottky gate," *Jap. J. Appl. Phys.* **46**, 2291 (2007).

[82] Y. Ando, Y. Okamoto, H. Miyamoto, T. Nakayama, T. Inoue, and M. Kuzuhara, "10-W/mm AlGaN-GaN HFET with a field modulating plate," *IEEE Electron. Device Lett.* **24**, 289 (2003).

[83] J. Bernát, P. Javorka, A. Fox, M. Marso, H. Lüth, and P. Kordoš, "Effect of surface passivation on performance of AlGaN/GaN/Si HEMTs," *Solid-State Electron.* **47**, 2097 (2003).

[84] B. M. Green, K. K. Chu, E. M. Chumbes, J. A. Smart, J. R. Shealy, and L. F. Eastman, "The effect of surface passivation on the microwave characteristics of undoped AlGaN/GaN HEMTs," *IEEE Electron. Device Lett.* **21**, 268 (2000).

[85] T. Li, R. P. Joshi, and C. Fazi, "Monte Carlo evaluations of degeneracy and interface roughness effects on electron transport in AlGaN/GaN heterostructures," *J. Appl. Phys.* **88**, 829 (2000).

[86] D. Zanato, S. Gokden, N. Balkan, B. K. Ridley, and W. J. Schaff, "The effect of interface-roughness and dislocation scattering on low temperature mobility of 2D electron gas in GaN/AlGaN," *Semicond. Sci. Technol.* **19**, 427 (2004).

[87] U. K. Mishra, L. Shen, T. E. Kazior, and Y-F. Wu, "GaN-based RF power devices and amplifiers," *Proc. IEEE* **96**, 287 (2008).

[88] R. Oberhuber, G. Zandler, and P. Vogl, "Mobility of two-dimensional electrons in AlGaN/GaN modulation-doped field-effect transistors," *Appl. Phys. Lett.* **73**, 818 (1998).

[89] J. S. Speck, and S. J. Rosner, "The role of threading dislocations in the physical properties of GaN and its alloys," *Phys. Rev. B: Condens. Matter* **273**, 24 (1999).

[90] N. G. Weimann, L. F. Eastman, D. Doppalapudi, H. M. Ng, and T. D. Moustakas, "Scattering of electrons at threading dislocations in GaN," *J. Appl. Phys.* **83**, 3656 (1998).

[91] A. Usui, H. Sunakawa, A. Sakai, and A. A. Yamaguchi, "Thick GaN epitaxial growth with low dislocation density by hydride vapor phase epitaxy," *Jpn. J. Appl. Phys.* **36**, L899 (1997).

[92] X. H. Wu, L. M. Brown, D. Kapolnek, S. Keller, B. Keller, S. P. DenBaars, and J. S. Speck, "Defect structure of metal-organic chemical vapor deposition-grown epitaxial (0001) GaN/Al_2O_3," *J. Appl. Phys.* **80**, 3228 (1996).

[93] S. T. Sheppard, K. Doverspike, W. L. Pribble, S. T. Allen, J. W. Palmour, L. T. Kehias, and T. J. Jenkins, "High-power microwave GaN/AlGaN HEMT's on semi-insulating silicon carbide substrates," *IEEE Electron. Device Lett.* **20**, 161 (1999).

[94] Y. -F. Wu, A. Saxler, M. Moore, R. P. Smith, S. Sheppard, P. M. Chavarkar, T. Wisleder, U. K. Mishra, and P. Parikh, "30-W/mm GaN HEMTs by field plate optimization," *IEEE Electron. Device Lett.* **25**, 117 (2004).

[95] S. Nakamura, M. Senoh, and T. Mukai, "Highly p-typed Mg-doped GaN films grown wiht GaN buffer laeyrs," *Jpn. J. Appl. Phys.* **30**, L1708 (1991).

[96] S. Nakamura, "GaN growth using GaN buffer layer," *Jpn. J. Appl. Phys.* **30**, L1705 (1991).

[97] I. Akasaki, H. Amano, Y. Koide, K. Hiramatsu, and N. Sawaki, "Effects of AlN buffer layer on crystallographic structure and on electrical and optical properties of GAN and $Ga_{1-x}Al_xN$ ($0 < x \leq 0.4$) films grown on sapphire substrate by MOVPE," *J. Cryst. Growth* **98**, (1989).

[98] I. Akasaki, and H. Amano, "Crystal growth and conductivity control of Group III nitride semiconductors and their application to short wavelength light emitters," *Jpn. J. Appl. Phys.* **36**, 5393 (1997).

[99] W. Kim, Ö. Aktas, A. E. Botchkarev, A. Salvador, S. N. Mohammad, and H. Morkoç, "Reactive molecular beam epitaxy of wurtzite GaN: Materials characteristics and growth kinetics," *J. Appl. Phys.* **79**, 7657 (1996).

[100] J. D. Mackenzie, C. R. Abernathy, J. D. Stewart, and G. T. Muhr, "Growth of group III nitrides by chemical beam epitaxy," *J. Cryst. Growth* **164**, 143 (1996).

[101] D. D. Koleske, A. E. Wickenden, R. L. Henry, W. J. DeSisto, and R. J. Gorman, "Growth model for GaN with comparison to structural, optical, and electrical properties," *J. Appl. Phys.* **84**, 1998 (1998).

[102] Y. Watanabe, and M. Sano, "NH_3 flow rates dependence of crystallinity in GaN thin films grown by reactive close-spaced method at low temperature," *J. Cryst. Growth* **237**, 1042 (2002).

[103] I. T. Ferguson, A. G. Thompson, S. A. Barnett, F. H. Long, and Z. C. Feng, "Epitaxial Film Growth and Characterization," in *Handbook of Thin Film Devices*, San Diego, California: Academic Press, 2000, pp. 1-53.

[104] S. K. Mathis, A. E. Romanov, L. F. Chen, G. E. Beltz, W. Pompe, and J. S. Speck, "Modeling of threading dislocation reduction in growing GaN layers," *J. Cryst. Growth* **231**, 371 (2001).

[105] J. Jasinski, and Z. Liliental-Weber, "Extended defects and polarity of hydride vapor phase epitaxy GaN," *J. Electron. Mater.* **31**, 429 (2002).

[106] Y. G. Zhou, R. Zhang, W. P. Li, B. Shen, P. Chen, Z. Z. Chen, S. L. Gu, Y. Shi, Y. D. Zheng, and Z. C. Huang, "Gas-phase parasitic reactions and Al incorporation efficiency in light radiation heating, low-pressure metal–organic chemical vapor deposition of AlGaN," *Mater. Lett.* **45**, 331-335 (2000).

[107] M. E. Coltrin, J. R. Creighton, and C. C. Mitchell, "Modeling the parasitic reactions of AlGaN organometallic vapor-phase epitaxy," *J. Cryst. Growth* **287**, 566 (2006).

[108] A. V. Kondratyev, R. A. Talalaev, W. V. Lundin, A. V. Sakharov, A. V. Tsatsul'nikov, E. E. Zaravin, A. V. Fomin, and D. S. Sizov, "Aluminum incorporation in AlGaN MOVPE: experimental and modeling study," *J. Cryst. Growth* **272**, 420 (2004).

[109] Q. Paduano, D. Weyburne, and S-Q. Wang, "Determination of alloy composition and residual stress for $Al_xGa_{1-x}N$/GaN epitaxial films," *Phys. Stat. Sol. A* **188**, 821 (2001).

[110] S. Einfeldt, V. Kirchner, H. Heinke, M. Dießelberg, S. Figge, K. Vogeler, and D. Hommel, "Strain relaxation in AlGaN under tensile plane stress," *J. Appl. Phys.* **88**, 7029 (2000).

[111] H. Amano, and I. Akasaki, "Critical issues in $Al_xGa_{1-x}N$ growth," *Opt. Mater.* **19**, 219 (2002).

[112] H. Amano, and I. Akasaki, "Novel aspects of the growth of nitrides by MOVPE," *J. Phys.: Condens. Matter* **13**, 6935 (2001).

[113] O. Briot, S. Ruffenach-Clur, M. Moret, and R. L. Aulombard, "X-ray reciprocal space mapping studies of strained GaN/AlGaN quantum wells," *Mat. Res. Soc. Symp. Proc.* **639**, G6.40.1 (2001).

[114] J. R. Jenny, and J. E. Van Nostrand, "The effect of Al on Ga desorption during gas source-molecular beam epitaxial growth of AlGaN," *Appl. Phys. Lett.* **72**, 85 (1998).

[115] G. W. Wicks, M. W. Koch, and J. R. Pedrazzani, "Studies of ammonia dissociation during the gas source molecular-beam epitaxial growth of III nitrides," *J. Vac. Sci. Technol. B* **23**, 1186 (2005).

[116] O. Briot, S. Clur, and R. L. Aulombard, "Competitive adsorption effects in the metalorganic vapor phase epitaxy of GaN," *Appl. Phys. Lett.* **71**, 1990 (1997).

[117] B. Heying, R. Averbeck, L. F. Chen, E. Haus, H. Riechert, and J. S. Speck, "Control of GaN surface morphologies using plasma-assisted molecular beam epitaxy," *J. Appl. Phys.* **88**, 1855 (2000).

[118] T. Kozawa, T. Kachi, T. Ohwaki, and Y. Taga, "Dislocation etch pits in GaN epitaxial layers grown on sapphire substrates," *J. Electrochem. Soc.* **143**, L17 (1996).

[119] K. Shiojima, "Atomic force microscopy and transmission electron microscopy observations of KOH-etched GaN surfaces," *J. Vac. Sci. Technol. B* **18**, 37 (2000).

[120] D. Billingsley, W. Henderson, D. Pritchett, and W. A. Doolittle, "Growth and characterization of $Al_xGa_{1-x}N$ via NH_3-based metal-organic molecular beam epitaxy," *J. Cryst. Growth* **311**, 1328 (2009).

[121] E. J. Tarsa, B. Heying, X. H. Wu, P. Fini, S. P. DenBaars, and J. S. Speck, "Homoepitaxial growth of GaN under Ga-stable and N-stable conditions by plasma-assisted molecular beam epitaxy," *J. Appl. Phys.* **82**, 5472 (1997).

[122] R. Held, D. E. Crawford, A. M. Johnston, A. M. Dabiran, and P. I. Cohen, "*In situ* control of GaN by molecular beam epitaxy," *J. Electron. Mater.* **25**, 272 (1997).

[123] D. E. Crawford, R. Held, A. M. Jonston, A. M. Dabiran, and P. J. Cohen, "Growth rate reduction of GaN due to Ga surface accumulation," *MRS Internet J. Nitride Semicond. Res.* **1**, 12 (1996).

[124] K. R. Evans, T. Lei, and C. R. Jones, "Gallium incorporation kinetics during gas source molecular beam epitaxy growth of GaN," *Solid-State Electron.* **41**, 339 (1907).

[125] E. Iliopoulos, and T. D. Moustakas, "Growth kinetics of AlGaN films by plasma-assisted molecular-beam epitaxy," *Appl. Phys. Lett.* **81**, (2002).

[126] S. D. Burnham, G. Namkoong, K. K. Lee, and W. A. Doolittle, "Reproducible reflection high energy electron diffraction signatures for improvement of AlN using *in situ* growth regime characterization," *J. Vac. Sci. Technol. B* **25**, 1009 (2007).

[127] S. Keller, G. Parish, P. T. Fini, S. Heikman, C. -H. Chen, N. Zhang, S. P. DenBaars, and U. K. Mishra, "Metalorganic chemical vapor deposition of high mobility AlGaN/GaN heterostructures," *J. Appl. Phys.* **86**, (1999).

[128] Y. Zhang, and J. Singh, "Charge control and mobility studies for an AlGaN/GaN high electron mobility transistor," *J. Appl. Phys.* **85**, 587 (1999).

[129] C. -Y. Hwang, M. J. Schurman, W. E. Mayo, Y-C. Lu, R. A. Stall, and T. Salagaj, "Effect of structural defects and chemical impurities on hall mobilities in low pressure MOCVD grown GaN," *J. Electron. Mater.* **26**, 243 (1997).

[130] M. Mesrine, N. Grandjean, and J. Massies, "Effect of NH_3 as nitrogen source for GaN molecular beam epitaxy," *Appl. Phys. Lett.* **72**, 350 (1998).

[131] D. D. Koleske, A. E. Wickenden, R. L. Henry, and M. E. Twigg, "Influence of MOVPE growth conditions on carbon and silicon concentrations in GaN," *J. Cryst. Growth* **242**, 55 (2002).

[132] Z. -Q. Fang, D. C. Look, B. Clafin, S. Haffouz, H. Tang, and J. Webb, "Thermally stimulated current spectroscopy and photoluminescence of carbon-doped semi-insulating GaN grown by ammonia-based molecular beam epitaxy," *Phys. Stat. Sol. C* **2**, 2757 (2005).

[133] A. Armstrong, D. Green, A. R. Arehart, U. K. Mishra, J. S. Speck, and S. A. Ringel, "Carbon-related deep states in compensated n-type and semi-insulating GaN:C and their influence on yellow luminescence," *Mat. Res. Soc. Symp. Proc.* **831**, E5.7.1 (2005).

[134] O. Lopatiuk, A. Osinsky, A. Dabiran, K. Gartsman, I. Feldman, and L. Chernyak, "Electron trapping effects in C- and Fe-doped GaN and AlGaN," *Solid-State Electron.* **49**, 1662 (2005).

[135] P. B. Klein, S. C. Binari, K. Ikossi-Anastasiou, A. E. Wickenden, D. D. Koleske, R. L. Henry, and D. S. Katzer, "Investigation of traps producing current collapse in AlGaN/GaN high electron mobility transistors," *Electron. Lett.* **37**, 661 (2001).

[136] C. Poblenz, P. Waltereit, S. Rajan, S. Heikman, U. K. Mishra, and J. S. Speck, "Effect of carbon doping on buffer leakage in AlGaN/GaN high electron mobility transistors," *J. Vac. Sci. Technol. B* **22**, 1145 (2004).

[137] S. Rajan, A. Chakraborty, U. K. Mishra, C. Poblenz, P. Walterreit, and J. S. Speck, "MBE-grown AlGaN/GaN HEMTs on SiC," *Int. J. High Speed Electron. Syst.* **14**, 732 (2004).

[138] S. S. Liu, and D. A. Stevenson, "Growth kinetics and catalytic effects in the vapor phase epitaxy of gallium nitride," *J. Electrochem. Soc.* **125**, 1161 (1978).

[139] Y. Dong, R. M. Feenstra, D. W. Greve, J. C. Moore, M. D. Sievert, and A. A. Baski, "Effects of hydrogen on the morphology and electrical properties of GaN grown by plasma-assited molecular-beam epitaxy," *Appl. Phys. Lett.* **86**, 121914 (2005).

[140] E. V. Yakovlev, R. A. Talalaev, A. S. Segal, A. V. Lobanova, W. V. Lundin, E. E. Zavarin, M. A. Sinitsyn, A. F. Tsatsulnikov, and A. E. Nikolaev, "Hydrogen Effects in III-nitride MOVPE," *J. Cryst. Growth* **310**, 4862 (2008).

[141] M. Kamp, M. Mayer, A. Pelzmann, and K. J. Ebeling, "Fundamentals, material properties and device performances in GaN MBE using on-surface cracking of ammonia," *MRS Internet J. Nitride Semicond. Res.* **2**, 26 (1997).

[142] D. Moscatelli, and C. Cavallotti, "Theoretical investigation of the gas-phase kinetics active during the GaN MOVPE," *J. Phys. Chem. A* **111**, 4620 (2007).

[143] S. Goto, Y. Nomura, Y. Morishita, Y. Katayama, and H. Ohno, "Effect of hydrogen radicals on the reduction of carbon incorporation into GaAs grown by using trimethylgallium," *Jpn. J. Appl. Phys.* **33**, 3825 (1994).

[144] TECTRA Physikalische Instrumente, *http://www.tectra.de/hydrogen.htm*, Accessed 2010.

[145] C4 Scientific Systems LLC, *http://c4scientific.com/products/MBE/Effusion-Cell/Atomic-Hydrogen-Source.html*, Accessed 2010.

[146] MBE Komponenten, *http://mbe-components.com/products/special/hcs.html*, Accessed 2010.

[147] U. Bischler, and E. Bertel, "Simple source of atomic hydrogen for ultrahigh vacuum applications," *J. Vac. Sci. Technol. A* **11**, 458 (1993).

[148] T. Sakurai, M. J. Cardillo, and H. D. Hagstrum, "Kinetics of the generation of atomic hydrogen and its adsorption on Si(110)," *J. Vac. Sci. Technol. A* **14**, 397 (1977).

[149] A. Sutoh, Y. Okada, S. Ohta, and M. Kawabe, "Cracking efficiency of hydrogen with tungsten filament in molecular beam epitaxy," *Jpn. J. Appl. Phys.* **34**, L1379 (1995).

[150] H. Suzuki, R. Togashi, H. Murakami, Y. Kumagai, and A. Koukitu, "Theoretical investigation on the decomposition process of GaN(0001) surface under a hydrogen atmosphere," *J. Cryst. Growth* **311**, 3103 (2009).

[151] Outokumpu HSC Chemistry, *http://www.outokumpu.com/hsc*, Accessed 2010.

[152] T. Palacios, L. Shen, S. Keller, A. Chakraborty, S. Heikman, S. P. DenBaars, U. K. Mishra, J. Liberis, O. Kiprijanovic, and A. Mautlionis, "Nitride-based high electron mobility transistors with GaN spacer," *Appl. Phys. Lett.* **89**, (2006).

[153] G. Parish, G. A. Umana-Membreno, S. M. Jolley, D. Buttari, S. Keller, B. D. Nener, and U. K. Mishra, "AlGaN/AlN/GaN high electron mobility transistors with improved carrier transport," *2004 Conference on Optoelectronic and Microelectronic Materials and Devices Proceedings (IEEE Cat. No. 04EX973)* 29 (2004).

[154] Agilent evalution of MOS capacitor oxide C-V characteristics using the Agilent 4294A, *http://cp.literature.agilent.com/litweb/pdf/5988-5102EN.pdf*, Accessed 2010.

[155] M. Gassoumi, O. Fathallah, C. Gaquiere, and H. Maaref, "Analysis of deep levels in AlGaN/GaN/Al_2O_3 heterostructures by CDLTS under a gate pulse," *Physica B* **405**, 2337 (2010).

[156] P. B. Klein, and S. C. Binari, "Photoionization spectroscopy of deep defects responsible for current collapse in nitride-based field effect transistors," *J. Phys.: Condens. Matter* **15**, R1641 (2003).

[157] P. B. Klein, S. C. Binari, K. Ikossi, A. E. Wickendon, D. D. Koleske, and R. L. Henry, "Current collapse and the role of carbon in AlGaN/GaN high electron mobility transistors grown by metalorganic vapor-phase epitaxy," *Appl. Phys. Lett.* **79**, 3527 (2001).

[158] A. Armstrong, A. R. Arehart, B. Moran, S. P. Den Baars, U. K. Mishra, J. S. Speck, S. A. Ringel, "Impact of carbon on trap states in n-type GaN grown by metalorganic chemical vapor deposition," *Appl. Phys. Lett.* **84**, 374 (2004).

[159] M. Wolter, P. Javorka, A. Fox, M. Marson, H. Lüth, P. Kordoš, R. Carius, A. Alam, and M. Heuken, "Photo-ionization spectroscopy of traps in AlGaN/GaN high-electron mobility transistors," *J. Electron. Mater.* **31**, 1321 (2002).

[160] T. Ogino, and M. Aoki, "Mechanism of yellow luminescence in GaN," *Jpn. J. Appl. Phys.* **19**, 2395 (1980).

[161] D. K. Schroder, *Semiconductor Material and Device Characterization: Third Edition*, Hoboken: John Wiley and Sons Inc., 2006.

[162] D. Pritchett, W. Henderson, D. Billingsley, and W. A. Doolittle, "Mixed alkyl exchange and exploitable surface interactions in InGaN by NH3-based metal organic molecular beam epitaxy," *J. Cryst. Growth* **310**, 5297 (2008).

[163] D. J. Santeler, "Exit loss in viscous tube flow," *J. Vac. Sci. Technol. A* **4**, 348 (1986).

[164] S. D. Burnham, and W. A. Doolittle, "In situ growth regime characterization of AlN using reflection high energy electron diffraction," *J. Vac. Sci. Technol. B* **24**, 2100 (2006).

[165] M. Moseley, D. Billingsley, W. Henderson, and W. A. Doolittle, "Transient atomic behavior and surface kinetics of GaN," *J. Appl. Phys.* **106**, 014905 (2009).

VITA

Daniel Billingsley is a native of Lafayette, Louisiana. He graduated Cum Laude with a Bachelor's degree from the University of Louisiana at Lafayette in Electrical and Computer Engineering in 2004. He then attended The Georgia Institute of Technology and studied Electrical Engineering, where he received his Master's degree in 2007 and his Doctor of Philosophy in 2010.

Publications and Conference Proceedings:

D. Billingsley, D. Pritchett, W. Henderson, A. G. Carver, S. D. Burnham, and W. A. Doolittle, "Investigation into the use of Molecular Hydrogen on the Growth of Gallium Nitride via Metal-Organic Molecular Beam Epitaxy," *Phys. Stat. Sol. (c)* **5**, 1723 (2007).

D. Billingsley, W. Henderson, D. Pritchett, and W. A. Doolittle, "Growth and Characterization of $Al_xGa_{1-x}N$ Grown by NH_3-based Metal-Organic Molecular Beam Epitaxy," *J. Cryst. Growth* **311**, 1328 (2008).

D. Billingsley, W. Henderson, D. Pritchett, and W. A. Doolittle, "Growth Kinetics of $Al_xGa_{1-x}N$ Grown via Ammonia-Based Metal-Organic Molecular Beam Epitaxy," *J. Cryst. Growth* **312**, 209 (2010).

D. Billingsley, W. Henderson, and W. A. Doolittle, "High-temperature Growth of GaN and $Al_xGa_{1-x}N$ via Ammonia-Based Metal-Organic Molecular Beam Epitaxy," *J. Electron. Mater.* **39**, 473 (2010).

D. Pritchett, W. Henderson, D. Billingsley, and W. A. Doolittle, "InGaN Compositional Patterning by Ultraviolet Photoexcitation during NH_3-based MOMBE – A Pathway to 3D Epitaxy," *Phys. Stat. Sol. (c)* **5**, 1726 (2007).

D. Pritchett, W. Henderson, D. Billingsley, and W. A. Doolittle, "Mixed Alkyl Exchange and Exploitable Surface Interactions in InGaN by NH_3-based MOMBE," *J. Cryst. Growth* **310**, 5297 (2008).

D. Pritchett, W. Henderson, D. Billingsley, and W. A. Doolittle, "Influence of Ultraviolet Photoexcitation on the Growth of InGaN by NH_3-based Metal Organic Molecular Beam Epitaxy," *to be submitted* (2009).

D. Pritchett, W. Henderson, D. Billingsley, and W. A. Doolittle, "Influence of Intense Photoexcitation on Mg-doped GaN by NH_3-based Metal Organic Molecular Beam Epitaxy," *to be submitted* (2009).

D. Pritchett, D. Billingsley, W. Henderson, and W. A. Doolittle, "Growth Regimes of GaN during NH_3-based Metal Organic Molecular Beam Epitaxy," *to be submitted* (2009).

M. Moseley, D. Billingsley, W. Henderson, and W. A. Doolittle, "Transient Atomic Behavior and Surface Kinetics of GaN," *J. Appl. Phys.* **106**, 014905 (2009).

E. Trybus, W. A. Doolittle, M. Moseley, W. Henderson, D. Billingsley, G. Namkoong, and D. C. Look, "Extremely High Hole Concentrations in c-Plane GaN," *Phys. Stat. Sol. (c)* **6**, 5788 (2009).

D. Billingsley, D. Pritchett, W. Henderson, E. Trybus, K. K. Lee, and W. A. Doolittle, "Influence of Surface Nitridation on GaN Grown via NH_3-based Metal-Organic Molecular Beam Epitaxy," 24th *North American Molecular Beam Epitaxy Conference,* October 8-11, 2006.

D. Billingsley, D. Pritchett, W. Henderson, A. G. Carver, S. D. Burnham, and W. A. Doolittle, "Investigation into the use of Molecular Hydrogen on the Growth of Gallium Nitride via Metal-Organic Molecular Beam Epitaxy," *7th International Conference on Nitride Semiconductors*, September 16-21, 2007.

D. Billingsley, W. Henderson, and W. A. Doolittle, "Study of Growth Kinetics and Characterization of $Al_xGa_{1-x}N$ Grown by Ammonia-Based Metal-Organic Molecular Beam Epitaxy," *51st Electronic Materials Conference*, June 24-26, 2009.

D. Pritchett, W. Henderson, D. Billingsley, and W. A. Doolittle, "InGaN Compositional Control by Ultraviolet Photoexcitation during NH_3-Based MOMBE – A Pathway to 3D Epitaxy," *7th International Conference on Nitride Semiconductors*, September 16-21, 2007.

D. Pritchett, D. Billingsley, W. Henderson, and W. A. Doolittle, "Influence of Ultraviolet Photoexcitation on the Growth of InGaN via NH_3-based MOMBE," *Workshop on Compound Semiconductor Materials and Devices*, February 18-21, 2007.

D. Pritchett, D. Billingsley, W. Henderson, and W. A. Doolittle, "Toward Engineered 3-Dimensional Epitaxy Using Micro-Mirror Patterned Photo-Assisted Epitaxy," *50th Electronic Materials Conference*, June 25-27, 2008.

M. Moseley, E. Trybus, D. Billingsley, W. Henderson, G. Namkoong, J. Freitas, and W. A. Doolittle, "Deeply Degenerate p-GaN Grown by Metal-Modulated Epitaxy," *26th North American Molecular Beam Epitaxy Conference*, August 9-12, 2009.

E. Trybus, S. Burnham, G. Namkoong, D. C. Look, D. Billingsley, M. Moseley, W. Henderson, and W. A. Doolittle, "Systematic Study of High Hole Concentration, Low Temperature Grown GaN Approaching the Compensated Region," *50th Electronic Materials Conference*, June 25-27, 2008.

E. Trybus, W. A. Doolittle, M. Moseley, W. Henderson, D. Billingsley, G. Namkoong, and D. C. Look, "Extremely High Hole Concentrations in c-Plane GaN," *International Workshop on Nitride Semiconductors*, October 6-10, 2008.